GaN-Based Multi-Active-Bridge Converter with Hot-Swapping Capability

by

Shumeng Wang

A Master's Thesis submitted to
Faculty of Electrical Engineering, Mathematics and Computer Science
At Delft University of Technology
In Fulfillment of the Requirements
For a Master of Science Degree in Electrical Engineering
To be defended publicly on Thursday, August 25th, 2022 at 09:00 AM

Student Number:	5297087	
Project Duration:	December 13, 2021 – August 25, 2022	
Thesis Committee:	Prof. dr. P. Bauer,	TU Delft, DC Systems, Energy Conversion & Storage
	Dr. Z. Qin,	TU Delft, DC Systems, Energy Conversion & Storage
	Dr. P. Manganiello,	TU Delft, Photovoltaic Materials and Devices
Thesis Supervisor:	Prof. dr. P. Bauer,	TU Delft, Thesis Advisor
	Dr. Z. Qin,	TU Delft, Supervisor
	Ir. S. Yadav,	TU Delft, Co-Supervisor

An electronic version of this thesis is available at `http://repository.tudelft.nl/`.

TU Delft

Preface

I would like to first express my gratitude to the Delft University of Technology and group of DC Systems, Energy Conversion & Storage, for giving me this wonderful opportunity to conduct researches in power converter design. This thesis is a very precious experience during my master study, and the topic of DC/DC converter help me realize the power of power electronics and its potential breakthrough and application of the future.

I would also like to express my gratitude to Prof. Pavol Bauer, Dr. Zian Qin, and Ir. Sachin Yadav for their firm support of my thesis work in the past months. I have been interested in wide-bandgap (WBG) based semiconductors for a long time and Dr. Qin gave me the opportunity to focus on the WBG-based converter, and with his help I gained many insights of this novel device and a firm interest. I was so poor in academic research and especially in hardware design, but Sachin was being so patient to guide me step by step, so I could finally accomplish the task and finish the thesis.

I want to thank my parents for being supportive for my master study and life overseas, both emotionally and financially, and they are always the firm support of the family. I would also like to express thanks to myself. Pursuing an academic degree abroad in never an easy issue, especially during the pandemic era, I thank my persistence in this major and in research.

I want to save my biggest gratitude and biggest love to my partner Yixuan Liu, a strong, wonderful and adorable girl who accompanies me during the past months, even with a distance of almost ten thousands kilometers away in China, and with six or seven hours time difference. All these difficulties could not weaken our relation and our mutual support. We worked together and solved plenty of difficulties on study, life and future career. We offered our maximum efforts to create our better future, we cried when facing endless preparation and interviews, we cried when some application didn't work out, we laughed into tears when we received offers from the same institution. If I didn't have her I may have broken down within this year. I am the luckiest boy for having her, for having a one that I genuinely trust in this world of complication and mess, who makes me still believe in love, and in a bright future.

The past two years has been a wonderful journey of my life, and this is an ending and also a new beginning for my next journey.

What's past is prologue.
— William Shakespeare

Shumeng Wang
August, 2022

Abstract

This thesis addresses a novel configuration of hot-swappable Multi-Active-Bridge (MAB) DC/DC converter in renewable-energy-based systems. As an extension of the Dual-Active-Bridge (DAB) converter, the MAB converter provides a multiport DC/DC converter solution with bidirectional power flow, simple phase shift control and galvanic isolation, but leaves problems in coupling operation, low availability and control complexity. In this thesis, the MAB converter with hot-swapping capability is proposed and studied. With a dedicated transformer design and circuit re-configuration, the converter allows a single port rigidly determines the voltage on the magnetizing inductance of the transformer, while the power flow of all other ports are naturally decoupled. The decoupled ports of this proposed MAB converter shows high independence in control and operation, thus can be hot-swappable and decentralized controlled. The hot-swapping interface circuit consisting of Negative-Temperature-Coefficient (NTC) and Metal-Oxide-Varistor (MOV) is proposed, and the benchmark of components selection is elaborated. The control of hot-swappable ports is implemented with a decentralized voltage loop and a SYNC module for phase shift control synchronization. A 2.2kW, 200kHz, two 350V, two 48V, four-port GaN-based MAB converter is simulated and tested for evaluation of decoupled operation, hot-swapping and decentralized control. Finally the hardware is designed and to be implemented for further and extended evaluation of hot-swappable MAB converter.

Index Terms — Dual-Active-Bridge Converter, Multi-Port Converter, Hot-Swapping Converter, Decentralized Control, GaN HEMT, Planar Transformer

Contents

1 Introduction 17

2 DAB, MAB, and Master-Slave Configuration 23
- 2.1 Typical DC/DC Topologies . . . 23
- 2.2 DAB Converter . . . 24
- 2.3 MAB Converter . . . 25
  - 2.3.1 MAB Topology and Waveform Derivation . . . 25
  - 2.3.2 Power Flow Mechanism of the MAB Converter . . . 27
- 2.4 Master-Slave Configuration . . . 30
  - 2.4.1 Qualitative Reasoning . . . 30
  - 2.4.2 Numerical Reasoning . . . 30
  - 2.4.3 Practical Implementation . . . 32

3 Hot-Swapping Implementation 37
- 3.1 Overview and Potential Problems . . . 37
  - 3.1.1 Case I: Voltage Source Load . . . 37
  - 3.1.2 Case II: Passive Load . . . 40
- 3.2 Surge Current Limiting . . . 43
  - 3.2.1 Description of NTC . . . 43
  - 3.2.2 Implementation of NTC in Hot-Swapping . . . 45
- 3.3 Surge Voltage Limiting . . . 47
  - 3.3.1 Description of MOV . . . 47
  - 3.3.2 Implementation of MOV in Hot-Swapping . . . 48

4 Decentralized Control Strategy 57
- 4.1 Overview . . . 57
  - 4.1.1 Traditional Control Scheme . . . 57
  - 4.1.2 Decoupled Control Scheme . . . 58
  - 4.1.3 Decentralized Control Scheme . . . 58
- 4.2 Practical Implementation . . . 59
  - 4.2.1 Control Implementation on Master Side . . . 59
  - 4.2.2 Control Implementation on Slave Sides . . . 59

5 Simulation 65
- 5.1 Overview . . . 65
- 5.2 Design Considerations . . . 66
  - 5.2.1 Sources and Loads . . . 66
  - 5.2.2 Rated Parameters . . . 66
  - 5.2.3 Control Systems Design . . . 66

5.3 Simulation in PLECS . . . 68
5.3.1 Simulation Case 1: Plugging In/ Plugging Out . . . 68
5.3.2 Simulation Case 2: Synchronization and Control . . . 69
5.3.3 Simulation Case 3: Decoupling Operation . . . 71

6 Hardware Design 77
6.1 Overview . . . 77
6.2 Master Board . . . 77
6.2.1 Auxiliary Power Supply . . . 77
6.2.2 GaN-Based Switch and Gate Driving . . . 78
6.2.3 Planar Transformer . . . 80
6.3 Slave Boards . . . 83
6.3.1 NTC and MOV Selection . . . 83
6.3.2 Auxiliary Power Supply . . . 84
6.3.3 Sync Sampling and Output Sampling . . . 84
6.3.4 GaN-Based Switch and Gate Driving . . . 86

7 Conclusion and Future Work 91
7.1 Conclusion . . . 91
7.2 Future Work . . . 91

A PCB Schematics and BOM List 95

List of Figures

1.1 The typical scenario of DC based renewable energy source systems [7]. 19
1.2 Topology of the half-bridge LLC DC/DC converter [8]. 20
1.3 Topology of the typical Buck-Boost DC/DC converter [9]. 20
1.4 Topology and control loop of the typical Flyback DC/DC converter [10]. . . . 20
1.5 Topology of the dual-active-bridge (DAB) DC/DC converter. 20
1.6 Topology of a traditional multi-active-bridge (MAB) converter. 21
1.7 The typical structure of lateral GaN-on-Si HEMT [11]. 21
1.8 The comparison of on resistance and gate capacitance of typical semiconductor transistors [6]. 22

2.1 Simplified model of DAB converter 26
2.2 Idealized transformer voltage and current waveform of DAB converter 27
2.3 Power of DAB converter versus the phase shift. The power flow is bi-directional and exclusively depends on the leading/lagging relation of two active bridges. 28
2.4 MAB converter in star-equivalent model [16]. 28
2.5 Idealized transformer voltage, star-point voltage and inductor current waveform of the four-port MAB converter, or the QAB converter. 33
2.6 Port #i and port #j of the MAB converter in delta model [16]. 34
2.7 Port #i and port #j of the MAB converter in the Thevenin equivalent model. Only port #i and port #j are considered while all the other sources are grounded due to the superposition theorem, and their leakage inductances as well as magnetizing inductance are modeled as $L'_{TH,X}$. 34
2.8 Master-slave configuration of the MAB converter. Port #1 is the master port with minimized leakage inductance, while all the other ports are slave ports and have significantly larger leakage inductances compared with port #1. . . 34
2.9 Normalized gain matrix of the MAB converter with different value of normalized master port leakage inductance. 35
2.10 A practical implementation of master-slave configuration of the MAB converter. The inherent leakage inductance of all ports of the transformer is almost identical and close to zero, and external inductors are added to slave ports only. 36

3.1 The hot-swapping configuration of the MAB converter. The sockets and plugs are applied to the transformer windings and slave modules. The parts colored in red are all modular and hot-swappable while the rest of the converter are stationary. 38
3.2 The hot-swapping configuration of the MAB converter with voltage source load. To simplify the circuit only one slave port is shown and discussed. . . . 40

3.3 The equivalent model of hot-swapping configuration of the MAB converter with voltage source load, both the source and load are represented with a square wave voltage source. To simplify the circuit only one slave port is shown and discussed. 40
3.4 The waveform of the first period of operation of the MAB converter with voltage source load after the plug is inserted into the socket. The initial current of the inductor and transformer is assumed to be zero. 41
3.5 The RMS current after plug insertion of the hot-swappable MAB converter with voltage source load. Time t_0 is the time of insertion and t_{SS} is the time that the converter reaches a steady state and thus a zero RMS current. 42
3.6 The hot-swapping configuration of the MAB converter with a passive component load, which is represented by a constant resistor. To simplify the circuit only one slave port is shown and discussed. 44
3.7 The configuration of auxiliary power supply (short for "AP" in the block diagram) of the slave module from the plug. To simplify the circuit only one slave port is shown and discussed. 44
3.8 The configuration of auxiliary power supply (short for AP in the block diagram) of the slave module from the DC bus. To simplify the circuit only one slave port is shown and discussed. 45
3.9 The conduction I-V curve for GaN enhancement-mode HEMT. The third-quadrant operation is similar to reverse diode [17]. 45
3.10 The equivalent circuit of the MAB converter with inactivated slave module. The active bridge on the slave side is replaced by a diode bridge rectifier. To simplify the circuit only one slave port is shown and discussed. 46
3.11 The equivalent circuit of hot-swapping configuration of the MAB converter with a passive load within the first cycle, the load voltage is zero and can be approximated as a short circuit. To simplify the circuit only one slave port is shown and discussed. 46
3.12 The waveform of the first period of operation of the MAB converter with passive load after the plug is inserted into the socket. The initial current is zero, and the insertion action has a phase delay of ϕ. 47
3.13 The equivalent circuit of the MAB converter with inactivated slave bridge. Unlike previous equivalent circuit, the master side parameters is referred to the slave side and the voltage source is a square wave source with a voltage V_1'. 48
3.14 The waveform of voltages and current for the MAB converter with diode bridge rectifier on the slave side. Any operation period should contains state (a), (b), (c) and (d) consecutively. The square voltage appeared before the diode bridge, which is denoted as V_{T2}, should have the same direction with the leakage current. 49
3.15 The four operation states of the MAB converter with diode rectifier bridge on the slave side. The four states are caused by the two directions of source voltage V_1' and two directions of leakage current i_σ. Due to different current direction, corresponding diodes that form circuit power flow loop are marked in red. For simplicity only one slave port is shown and discussed in this sketch. 50

3.16 The RMS current behavior after plug insertion of the hot-swappable MAB converter with passive load. Time t_0 is the time of insertion and t_{SS} is the time that the converter reaches a steady state with non-zero RMS current. . . 50
3.17 The typical R-T curve for NTC resistor. 51
3.18 The intuitive demonstration of computation of NTC resistance at steady state operation, given that the resistance of the NTC is comparatively much smaller than the equivalent resistance of the circuit, thus the effective current I_{rms} is the current rating of the original circuit. 51
3.19 The application of NTC resistor in hot-swappable slave ports. 52
3.20 The equivalent model of the MAB converter with an NTC resistor. To simplify the circuit only one slave port is demonstrated. 52
3.21 The waveform of the voltages and current of hot-swappable converter of the first period. The NTC resistor is in a quasi-static state and can be approximated as a constant-value resistor. The current is suppressed compared with the converter without current limiting components. 53
3.22 Under steady state, the NTC resistor shows small resistance and therefore can be ignored in the circuit. The MAB converter with NTC under steady state operation will be approximated as normal MAB converter. 53
3.23 The NTC selection standard for slave side with resistive load. 54
3.24 The typical V-I curve for Metal-Oxide-Varistor. 54
3.25 The MAB converter circuit with both NTC resistor and MOV resistor. 54
3.26 The equivalent model of the MAB converter with both NTC and MOV. 55
3.27 The power flow in the MAB converter with MOVs. 55
3.28 The waveform of plug voltage, external leakage inductor current, MOV current and equivalent MOV resistance is sketched during normal steady-state operation and plugging-out transient. 56
3.29 The demonstration of requirements for MOV selection. The appropriate MOV should satisfies that the operating maximum instantaneous current and operating voltage should fall in the red region. 56

4.1 The typical current loop control block diagram for MIMO MAB system. 57
4.2 The decoupled current loops for the MAB converter. The original MIMO system is devided into multiple SISO systems and can be controlled independently. 59
4.3 The ideal of decentralized control strategy of the MAB converter. 60
4.4 The block diagram and signal visualization of the control system of the master port. 60
4.5 The waveforms in control systems of PWM generation with fixed duty ratio and phase. This is applicable in master sides. 61
4.6 The voltage waveform of transformer windings of the MAB converter. This is under the assumption that the leakage inductance of the transformer is negligible. 62
4.7 The configuration of the decentralized control system with a SYNC module of the slave ports. 62
4.8 The block diagram and signal visualization of the control system of the slave ports. 63

4.9 The waveforms in control systems of PWM generation. The solid line is a signal with fixed duty ratio and phase, which represents the signals from the master side. The dashed signal is the modulated signal with a fixed duty ratio but with a phase-shoft compared to the solid line, which can represent the waveform from the slave sides. 63

5.1 The block diagram of full control loop of any slave port of decoupled MAB converter. 67
5.2 The open loop gain for port #1 (high voltage port) and port #2, #3 (low voltage ports). The PI values selected ensured similar response speed for evaluation. 68
5.3 The R-T curve for *TDK* NTC series. The type B57127P709M301 selected corresponds to the second curve from the top (red arrow). 69
5.4 The trendline for R-T curve for NTC type B57127P709M301.The value obtained in this plot is only for simulation purposes, and may cause large error in theoretical computation. 70
5.5 The simulation configuration of the MAB converter for NTC verification. . . . 70
5.6 The current waveform comparison and resistance of NTC at transient plugging-in action. The green curve (port with NTC) shows smaller inrush current than the red curve (port without NTC). 71
5.7 The current waveform comparison and resistance of NTC at steady state operation. With a resistance value lower than 1Ω, the port with NTC shows almost no difference with the port without NTC. 72
5.8 The simulation configuration of the MAB converter for case 2. To simplify the verification of control systems only one slave port is examined. 72
5.9 The SYNC module implementation. The transport delay simulates the delay in signal processing in practical implementations. 72
5.10 The load step response upon connection of extra load. The voltage maintained at 350V with a small fluctuation. The delay is set by default of 100ns (2%T). 73
5.11 The comparison between carrier wave from SYNC module and the constant carrier wave from the master side. Only a small phase shift of t_{delay} is assumed in sampling, and can be observed in generated carrier waves. 73
5.12 The load step response with different values of SYNC delay time. With up to 10% of time delay, the load voltage shows stability and fast response of maintaining at rated voltage during load step transient. 74
5.13 The simulation configuration of the MAB converter for case 3. The load step is applied to the high voltage port. 74
5.14 The voltage of high voltage ports and low voltage ports upon load step change at high voltage port are plotted to evaluate the decoupling operation of the MAB converter. The series of values of leakage inductances is selected for this decoupling evaluation. 75

6.1 The overview demonstration of the hot-swapping prototype. 78
6.2 The overview of 3D model of the master board prototype. 79
6.3 The configuration of master side auxiliary power supply. 80
6.4 The PCB implementation of auxiliary power circuit on the master side. 80
6.5 The LTspice simulation of LT8315 based buck circuit. 81

6.6 The LTspice simulation results of LT8315 based buck circuit, converting 350V DC to 12.5V DC, with an output power of 1.6W. 81
6.7 The figure of GS66508B 650V GaN enhancement-mode HEMT from *GaN Systems*. 82
6.8 The switching off energy losses with different turn-off gate voltages [20]. The testing device is GS66516B with a bus voltage $V_{DC} = 400V$ and gate resistor $R_G = 1\Omega$. 83
6.9 The gate driving interface circuit for GS66508B. 83
6.10 The gate driving interface circuit implemented on PCB. 83
6.11 The level shifted voltage from 0V/12V to -6V/6V with the help of gate driving interface designed. 84
6.12 The planar E core E64/10/50 selected for four-PCB-winding planar transformer. 85
6.13 The cross sectional view of planar transformer configuration for this four-port MAB converter. 86
6.14 The PCB windings and sizes for master side, high voltage slave side and low voltage slave side respectively. 86
6.15 The finite element modelling for four-PCB-winding planar transformer. . . . 87
6.16 The coupling coefficient matrix of the four-winding planar transformer. . . . 87
6.17 The R-T curve for *TDK* NTC series. The type B57236S0229M000 selected corresponds to the first curve from the bottom (red arrow). 88
6.18 The V-I curve for *YAGEO* NTC series. The type 391KD14 and 181KD14 selected correspond to the curves pointed by green arrows. 88
6.19 The PCB implementation of auxiliary power circuit on the slave side. 89
6.20 The LTspice simulation results of auxiliary power circuit on the low voltage slave side. 89
6.21 The theoretical schematic of AC sampling circuit of the plug voltage for slave ports. 89
6.22 The LTspice simulation results of waveform of AC sampling circuit. 90
6.23 The theoretical schematic of DC sampling circuit of the bus voltage for slave ports. 90
6.24 The figure of GS61008P 100V GaN enhancement-mode HEMT from *GaN Systems*. 90

List of Tables

2.1 Comparison between different popular topologies of DC/DC converter 24

5.1 MAB converter specifications 65
5.2 K_P and K_I values selected for controllers of slave ports different voltage power ratings. 67
5.3 MAB converter specifications 68

6.1 GaN HEMT GS66508B important ratings, compared with C3M0065100K. . . . 82
6.2 Important specifications of the planar transformer for the MAB converter. . . 84
6.3 Inductance values of the planar transformer designed for the MAB converter, unit:μH. 85
6.4 Coupling coefficients of the four windings of the planar transformer designed for the MAB converter. 85
6.5 The NTC and MOV type selected and their corresponding characteristics curves. 87
6.6 GaN HEMT GS61008P important ratings, compared with C3M0065100K. . . . 87
6.7 GaN HEMT GS61008P and GS66508B gate resistance values selection. 88

1 Introduction

In the recent development of renewable-energy-resources-based systems, DC sources, DC loads and DC storages are common components in this application scenario (Figure 1.1). Therefore, there is an growing demand for converters that converts power from Direct Current (DC) to DC for the essential infrastructure of the power system. General requirements for DC/DC converters in the novel system are isolation and bidirectional power flow. Compared with the LLC converter, Buck-Boost converter and Flyback converter as shown in Figure 1.2, Figure 1.3 and Figure 1.4 respectively which are commonly-used in DC/DC converters, the Dual-Active-Bridge (DAB) converter fulfills the fundamental needs, and also shows advantages in design and control simplicity, and thus is selected as an basic topology for this thesis design.

To integrated multiple sources and loads within the system, the multiport converter (MPC) provides an integrated solution that all DC sources, storage, and loads are interconnected with a single converter, by which the power flow is multi-directional [1], [2]. Derived from the DAB converter (Figure 1.5), [3] proposed a three-port isolated bidirectional DC/DC converter. In a more general case, the multi-active-bridge (MAB) converter shown in Figure 1.6 can achieve theoretically any number of ports, and has the following features that help it become one promising MPC implementation topology in recent multiport DC/DC applications. Primarily, the multiple ports within the MAB converter composed of multiple inverter bridges (either half-bridge or full-bridge) are highly symmetrical, and the AC sides are interconnected via a single multi-winding transformer. Consequently, ports with different voltage and power levels are guaranteed with galvanic isolation. Additionally, the MAB converter inherits the control scheme of the DAB converter that bi-directional power flow can be realized by simple control schemes.

However, the traditional topology of the MAB converter shows shortcomings that limits the mass-application of this multi-port converter. The ports are natually coupled through the multi-winding transformer and consequently brings interference among all the ports. The methodologies of decoupling the ports can be categorized into two directions, which are a) active control methods and b) dedicated configuration of hardware circuits. For the first type, researchers applied software implementation methods to reject the disturbances from any ports in control systems, and with the well-tuned controller the prototype showed satisfying results of decoupling and decentralized control [3], [4], [5]. S. Bandyopadhaya et al. also modified the circuit topology and configured a “master-slave” topology in [1], by

which one port dominates the converter operation and the slave ports share minimum linking inductance to be inherently decoupled. The hardware direction shows high implementation feasibility and reliability and thus adopted for the decoupling method of the MAB converter proposed. The benchmark for master-slave configuration and a practical method of implementation is given in Chapter 2 of this thesis.
Moreover, the MAB converter with stationary ports and fixed quantity of terminals shows low availability and low scalability issues that limits the versatility of the converter in practical applications. The low availability means the the converter lacks resilience to unexpected downtime of the converter, as a result when one port breaks down the whole converter needs to be shut down and replace the specific port. This shortage problem is unacceptable for high-availability systems such as data centers. The scalability means the converter ports is limited and fixed once the converter is implemented and applied. To solve the problem mentioned above, this thesis provides a novel configuration that the ports are hot-swappable, and by adding a buffer circuit for safe hot-swapping. The buffer circuit should contain an inrush current limiter and an voltage clamping component, and the benchmarks for the component selection are studied and will be discussed in Chapter 3. With the new solution the system downtime is eliminated and the scalability increases.
Additionally, the control scheme for this converter needs to be re-designed for smooth hot-swapping and guaranteed high scalability. In this thesis the decentralized control is derived and implemented, and will be discussed in Chapter 4. Unlike centralized control that pertains to traditional converters, controllers responsible for their corresponding ports solely are introduced to facilitate hot-swapping ports with reliable control. Moreover, decentralized control scheme provides an independent controller for the additional ports while connected to the converter, and thus scalability of the converter is ensured.
To simulate the proposed theory from Chapter 2 - Chapter 4, the simulation of four-port MAB converter is carried in Chapter 5. Among the four ports, port #1 plays an role of master port while port #2 - #4 are slave ports which are supposed to work in a decoupled and decentralized way. The voltage control loop provides a stable operation upon load changes and disturbance from other ports. The performance of NTC resistor and MOV resistor are also evaluated in this Chapter to validate the design consideration for a hot-swapping configuration.
Finally, to evaluate the theoretical design proposed from Chapter 2 - Chapter 4, a hardware design is carried to implement the prototype for future testings in Chapter 6. To facilitate a high power density and concise design of the hardware, the Wide-Bnadgap (WBG) based switches, 650V and 100V rated voltage GaN enhancement-mode High-Electron-Mobility-Transistor (HEMT) from *GaN Systems* are adopted for active bridges. The GaN-based HEMT, as the structure shown in Figure 1.7, shows advantages in gate capacitance and conduction resistance, which suggests a outstanding characteristics in faster switching transition, switching losses and conduction losses compared with SiC and Si MOSFET, as intuitively demonstrated in Figure 1.8 [6].
Another key part of hardware design is the tightly coupled transformer. Unlike traditional E core, ER core and Litz wires used for transformer design, the planar transformer core with PCB windings is designed for minimized leakage inductance, and thus a highly decoupled operation is achieved for the MAB converter. The design details will be further discussed in Chapter 6.
To conclude, the research objectives of this thesis are listed as following:

1. Overview of the DC/DC topologies and overview of the decoupled multiport converter method “master-slave configuration” adopted in this thesis is reviewed.

2. To increase the system availability and scalability, the hot-swapping capability will be configured with the help of passive components, and the benchmark for component selection is proposed.

3. To resolve the shortages of low flexibility and complexity of traditional centralized control methods, the decentralized control methods by which ports can be independently controlled is going to be implemented with the decoupled power flow.

4. The GaN HEMT based concise hardware for the converter is designed, and the dedicated transformer design is implemented to achieve the decoupling method mentioned in item 1.

In this thesis, the content is presented in seven chapters. The overview of DAB, MAB and the Master-Slave Configuration is reviewed in Chapter 2. Chapter 3 elaborates the theoretical problems of hot-swapping configuration and provides an cost-effective solution for the novel design. Chapter 4 demonstrates the control theory and practical implementation of decentralized control scheme. The simulation of specific operation cases of a four-port MAB converter, which is renamed as Quad-Active-Bridge (QAB) converter is presented in Chapter 5. Finally, an overview of hardware design will be given in Chapter 6, followed by a general conclusion of this thesis in Chapter 7.

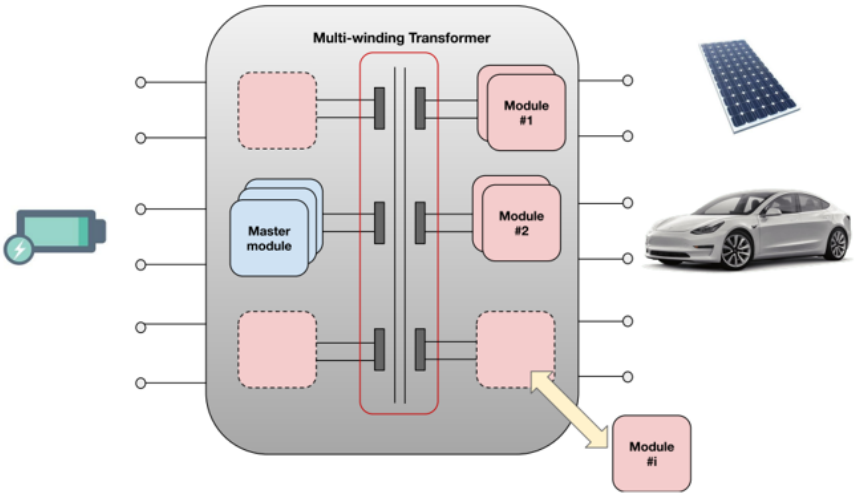

Figure 1.1: The typical scenario of DC based renewable energy source systems [7].

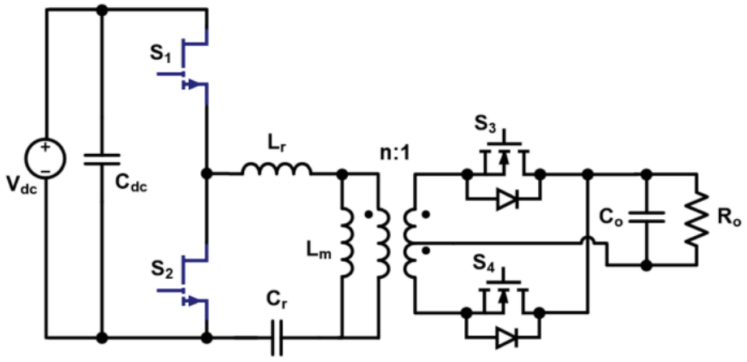

Figure 1.2: Topology of the half-bridge LLC DC/DC converter [8].

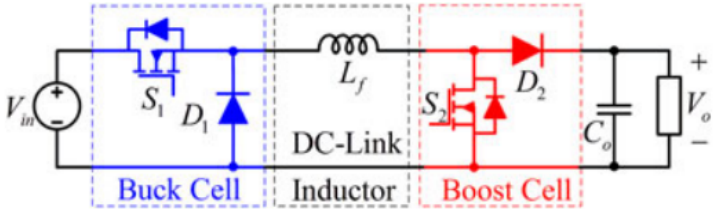

Figure 1.3: Topology of the typical Buck-Boost DC/DC converter [9].

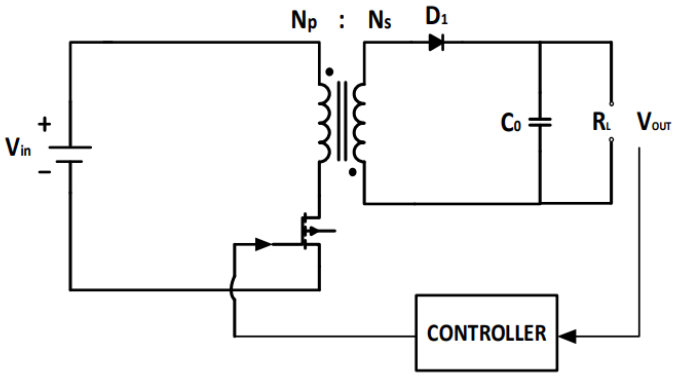

Figure 1.4: Topology and control loop of the typical Flyback DC/DC converter [10].

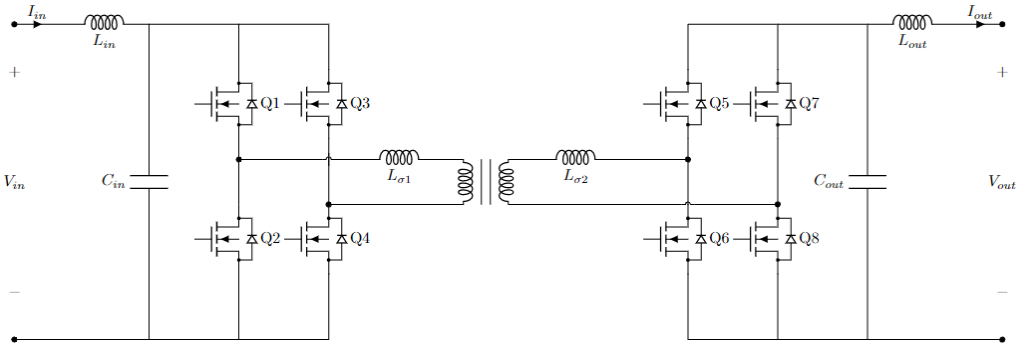

Figure 1.5: Topology of the dual-active-bridge (DAB) DC/DC converter.

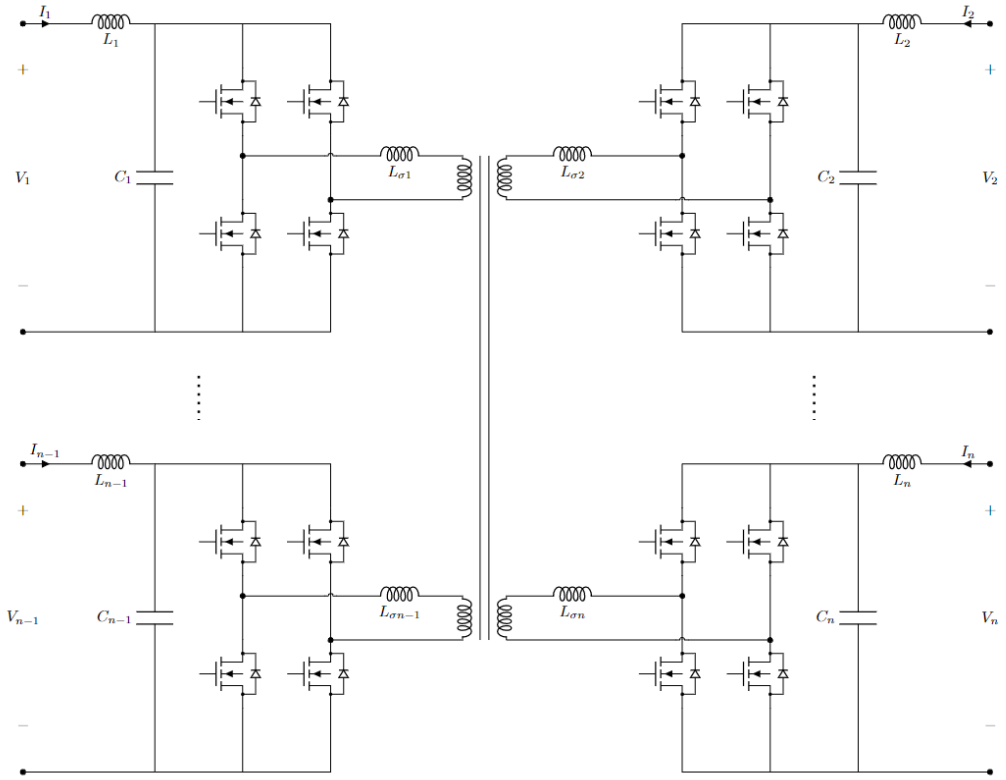

Figure 1.6: Topology of a traditional multi-active-bridge (MAB) converter.

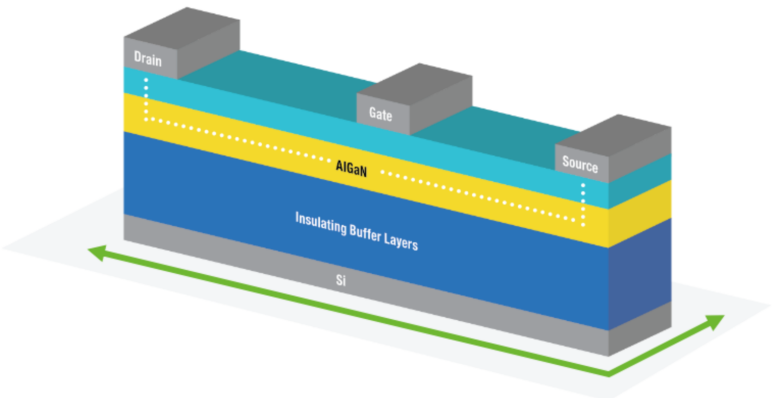

Figure 1.7: The typical structure of lateral GaN-on-Si HEMT [11].

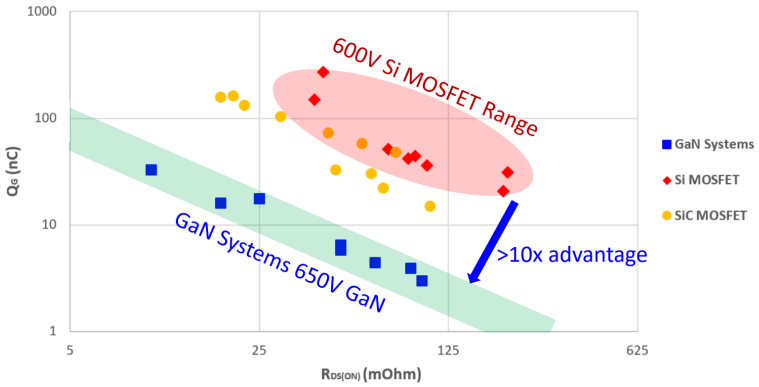

Figure 1.8: The comparison of on resistance and gate capacitance of typical semiconductor transistors [6].

2

DAB, MAB, and Master-Slave Configuration

2.1. Typical DC/DC Topologies

The research on DC/DC converter has been a popular top in the area of power converters in recent decades. Typical single-input-single-output DC/DC converter includes the LLC resonant converter, the Buck, Boost or Buck-Boost converter and the DAB converter. Each type of the converter topology have its own advantages and shortages, and their suitable application scenarios. In this section, four types of typical DC/DC topologies are discussed and compared, which are LLC resonant, Buck-Boost, Flyback and DAB converter, and the summary of characteristics of these four topologies are listed in Table 2.1.

The LLC resonant converter is demonstrated in Figure 1.2 and is a popular topologies in industrial DC/DC converter implementation for its high performance. The output-input relation of LLC converter depends on the gain situation of resonance network, and thus a frequency-dependent converter. The design flexibility of LLC converter is high, it can be either full-bridge or half-bridge, and the secondary side can be either active bridge or passive diode rectifier. Therefore, the LLC converter is a typical uni-directional DC/DC converter that is not applicable in renewable-energy based multi-directinal systems. Also due to frequency control essence, to achieve large output range of the LLC converter, a wide range of generated frequency is required thus brings complexity in both practical hardware design and software design[12].

The Buck converter, Boost converter and Buck-Boost converter (Figure 1.3) are the most basic implementation of DC/DC converters and due to its simplicity of the circuit and control scheme, and they show advantages in number of semiconductor components and therefore the losses are comparatively smaller. The typical Buck-Boost converter family only consists of active semiconductors (switches), passive semiconductor (diodes) and inductors, and therefore cannot provide galvanic isolation and thus not applicable in systems that requires reliable operation. Moreover, the efficiency drastically drops with high output-input voltage difference, and result in a low output range, which also limits the application of Buck-Boost converter [13].

The Flyback converter can be regarded as an extension of Buck-Boost converter in isolated configuration, as topology demonstrated in Figure 1.4. However unlike the typical hard switching operation of Buck-Boost converter, The soft switching can be achievable by adding an active auxiliary cell in parallel with the active switch[14]. Also the transformer provides a galvanic isolation which is more reliable compared with the Buck-Boost con-

verter. Also similar to the Buck-Boost converter, they are both pulse width controlled and the operation voltage range is limited.
The DAB converter however, possesses a series of advantages that is more applicable compared with the other three topologies. The transformer provides an isolation from input to output, and the symmetrical structure suggests a design simplicity and a naturally bidirectional power flow. The most typical control methods is Single Phase-Shift (SPS) modulation strategy, and therefore the operation voltage range and power range is higher than the converters mentioned above.

Table 2.1: Comparison between different popular topologies of DC/DC converter

	LLC	**Buck-Boost**	**Flyback**	**DAB**
Galvanic Isolation	✓	×	✓	✓
Bidirectional Power Flow	×	×	×	✓
Symmetric Structure	×	×	×	✓
Components Cost	High	Lowest	Low	High
Operating Voltage Range	Low	Low	Low	High
Soft/Hard Switching	Soft	Hard	Soft	Soft
Typical Control Method	PFM	PWM	PWM	SPS

2.2. DAB Converter

Thus, the DAB topology has been one form of prevailing implementation of isolated DC/DC converter [15]. Compared with other counterpart topologies, the DAB provides the galvanic isolation as well as a simple control scheme. Considering the ideal transformer and ideal switching behavior, the DC source and loads after the switching bridge shows a square waveform, with the amplitude of DC bus voltage. Under this simplification premise, the DAB topology can be simply modeled as Figure 2.1.
The parameters in the secondary side are referred to the primary side, and the two active bridges with voltage sources are replaced with two rectangular voltage sources, with the amplitude of V_1 and V_2' respectively. The value of the parameters in the DAB converter should have the following relations:

$$V_2' = \frac{N_1}{N_2} V_2 \tag{2.1}$$

$$i_{T2}' = \frac{N_2}{N_1} i_{T2} \tag{2.2}$$

$$L_{\sigma 2}' = \left(\frac{N_1}{N_2}\right)^2 L_{\sigma 2} \tag{2.3}$$

Therefore, to derive the current waveform in this simplified converter model, the slope of the current through the equivalent inductor can be written as:

$$\frac{di_{T1}}{dt} = \frac{di_{T2}'}{dt} = \frac{V_1 - V_2'}{L_{\sigma 1} + L_{\sigma 2}'} = \frac{V_1 - V_2'}{L_{\sigma eq}} \tag{2.4}$$

Where the $L_{\sigma eq}$ is the total equivalent linking inductance between two ports, and is calculated by the sum of leakage inductances on both sides, which is $L_{\sigma 1}$ and $L_{\sigma 2}'$.

For a typical DAB converter, the most traditional implementation of the DAB converter should have the following basic restrictions to facilitate a normal operation of the converter:

1. The switching bridges work in bipolar switching mode.

2. The duty ratio is 50% constantly.

3. The switching frequencies of two active bridges are constant and consistent.

The real transformer current waveform can be obtained once the voltage sources waveform are determined, and the Figure 2.2 demonstrates a case where the phase shift between two active bridges is ϕ. The turns ratio of transformer is configured as 1:1 for simplicity in this example case. The power flow of DAB converter, from terminal 1 to terminal 2 will be referred as positive power flow, and denoted as P_{12} can be obtained from integrating the voltage and current through one switching period, and the result can be expressed as the following:

$$P_{12} = \frac{V_1 V_2'}{2\pi L_{\sigma eq}} \phi \left(1 - \frac{|\phi|}{\pi}\right) T_s = \frac{V_1 V_2'}{2\pi \left(L_{\sigma 1} + L_{\sigma 2}'\right)} \phi \left(1 - \frac{|\phi|}{\pi}\right) T_s \tag{2.5}$$

Notably, the phase shift ϕ can be any value from $-\pi$ to π, resulting in either positive or negative P_{12} and thus a bi-directional power flow of the converter is achieved, as shown in Figure 2.3.
From equation 2.5, when the leakage inductance, source voltages and switching frequency remain constant, the power transferred from the primary side to the secondary side is exclusively determined by the phase shift ϕ. And the maximum power the DAB can achieve can be calculated by taking the first derivative of power, and obtain that when the phase shift $\phi = \frac{\pi}{2}$ or $\phi = -\frac{\pi}{2}$, the converter have the maximum power:

$$|P_{12}|_{max} = \frac{V_1 V_2'}{8 \left(L_{\sigma 1} + L_{\sigma 2}'\right)} T_s \tag{2.6}$$

Furthermore, from equation 2.5 and Figure 2.3, the power versus phase shift sketch between $\phi = \frac{\pi}{2}$ and $\phi = -\frac{\pi}{2}$ shows high linearity and montonicity, suggesting the most suitable phase shift range in control strategy.
From equation 2.6, when the source voltage, the leakage inductance is determined, the maximum power will have the positive correlation with the cycle time, thus the negative correlation with switching frequency. In general design of switch-based power converters, the trade-offs between power density and switch losses are key factors that determine the operation frequency selection, while in DAB converter, the power rating is also taken into consideration, which will be discussed in Chapter 5.

2.3. MAB Converter

2.3.1. MAB Topology and Waveform Derivation

As a heritage of DAB converter, the Multi-Active-Bridge (MAB) converter is an extension that can be regarded as a multi-port DAB converter, and shares multiple operation features with the DAB. However, the coil coupling between multi-winding transformer implied a

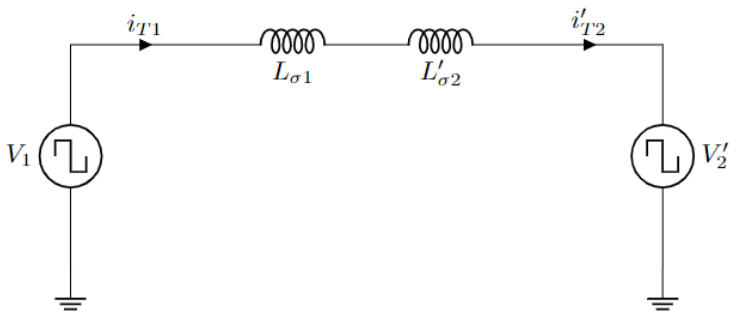

Figure 2.1: Simplified model of DAB converter

more complicated operation of MAB converter. For simplicity, Figure 2.4 provides a simplified star-equivalent model for n-port MAB topology, where the port #2 to port #n are referred to the port #1, and also the magnetizing inductance L_m. Therefore, the parameter values should have the following relations:

$$V'_i = \frac{N_1}{N_i} V_i \tag{2.7}$$

$$i'_{Ti} = \frac{N_i}{N_1} i_{Ti} \tag{2.8}$$

$$L'_{\sigma i} = \left(\frac{N_1}{N_i}\right)^2 L_{\sigma i} \tag{2.9}$$

The star-point voltage V_X, which is defined as the voltage appeared on L'_m, can be computed by the superposition theorem that is the sum of contributions of all sources:

$$V_X = \sum_{i=1}^{n} \frac{\left(\sum_{j=1, j\neq i}^{n} \frac{1}{L'_{\sigma j}} + \frac{1}{L'_m}\right)^{-1}}{L'_{\sigma i} + \left(\sum_{j=1, j\neq i}^{n} \frac{1}{L'_{\sigma j}} + \frac{1}{L'_m}\right)^{-1}} V'_i \tag{2.10}$$

For a real transformer, the magnetizing inductance is considerably larger than the leakage inductance and thus can be neglected in equation 2.10, and the equation for V_X can be further simplified as:

$$V_X = \sum_{i=1}^{n} \frac{\left(\sum_{j=1, j\neq i}^{n} \frac{1}{L'_{\sigma j}}\right)^{-1}}{L'_{\sigma i} + \left(\sum_{j=1, j\neq i}^{n} \frac{1}{L'_{\sigma j}}\right)^{-1}} V'_i \tag{2.11}$$

To simplify the equation expression, in equation 2.10 and equation 2.11, when $i = 1$, $L'_{\sigma 1}$ stands for the primary side leakage inductance “referred" to the primary side, and thus the transformer gain is assumed to be unity gain by nature. Therefore the value of $L'_{\sigma 1}$ is the same with $L_{\sigma 1}$.
With the help of voltage expression on the star point, the slope of the current through the

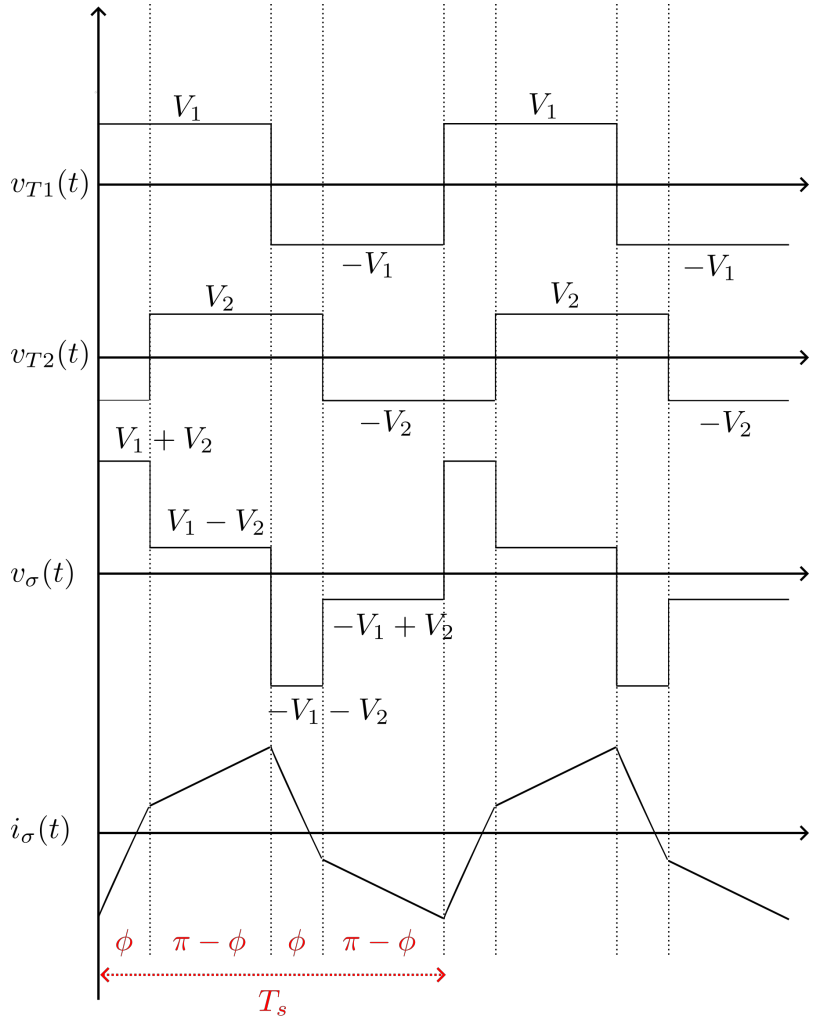

Figure 2.2: Idealized transformer voltage and current waveform of DAB converter

leakage inductance can be derived the same methods as in the DAB case:

$$\frac{di'_{Ti}}{dt} = \frac{V_X - V'_i}{L'_{\sigma i}} \tag{2.12}$$

Eventually, the idealized inductor current waveform of each port can be derived from comparing the port voltages (V_1, V'_2, ..., V'_n) and the star-point voltage. Figure 2.5 shows source voltage and the current waveform a case of four-port MAB converter, which is also known as Quad-Active-Bridge or QAB converter. In this idealized case, the turns of all windings within the transformer are identical and the leakage inductances are identical for all ports for simplicity. And the phase shift are randomly configured, while assuming the phase shift of port #1 is zero as reference.

2.3.2. Power Flow Mechanism of the MAB Converter

The star-equivalent model in the previous section demonstrates a brief topology for MAB converter in general, but to figure out the power flow between any pair of two ports in case of the MAB converter, another model named delta model in introduced as Figure 2.6. The delta equivalent model concentrates on any pair of two active ports and ignores the

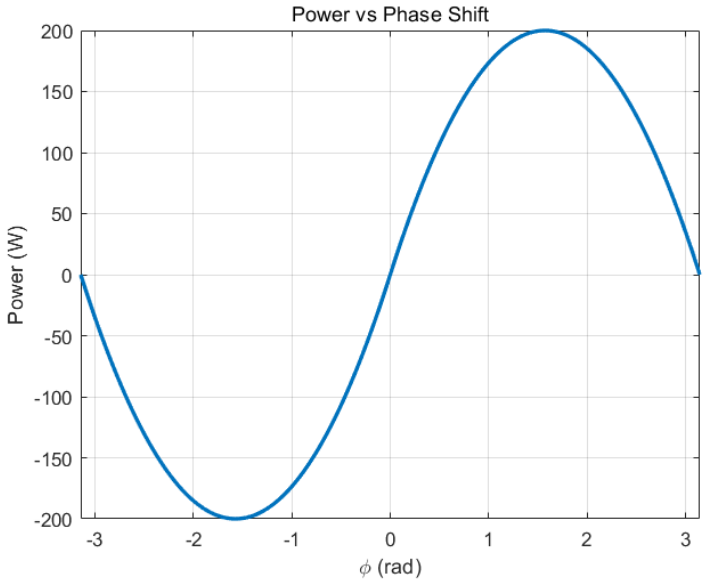

Figure 2.3: Power of DAB converter versus the phase shift. The power flow is bi-directional and exclusively depends on the leading/lagging relation of two active bridges.

other sources, and the power flow mechanism between these two ports are similar to the DAB case. From the Delta model, the MAB converter can be considered as an extension of the DAB converter, and on the contrary, the DAB converter can be regarded as a two-port MAB converter. Therefore, the power flow between any two active ports can be derived by analogy that:

$$P_{ij} = \frac{V_i' V_j'}{2\pi L_{ij}} \phi_{ij} \left(1 - \frac{|\phi_{ij}|}{\pi}\right) T_s \tag{2.13}$$

Where ϕ_{ij} is the phase shift between two switching signals of port #i and port #j, and the L_{ij} is the effective linking inductance between these two ports.
It is apparently observed from equation 2.5 of the DAB case and 2.13 of the MAB case that the equivalent inductance is essential in computing the power flow between two ports. However Figure 2.4 suggests a more complicated situation of inductance distribution of

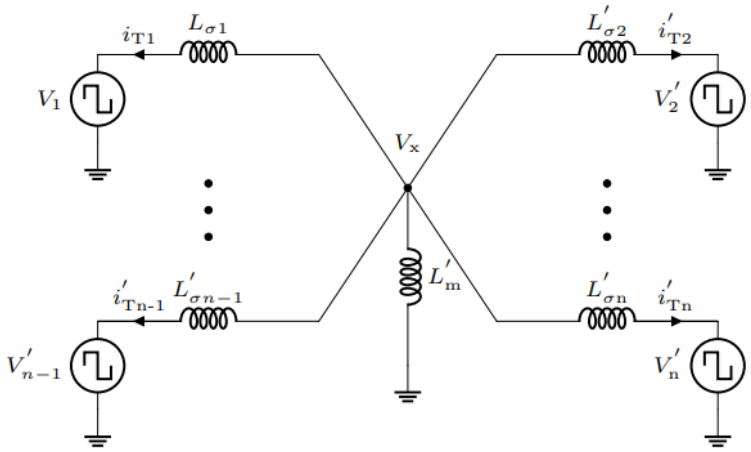

Figure 2.4: MAB converter in star-equivalent model [16].

the multi-port version of the converter. To figure out the power flow between any pair of two ports in case of the MAB converter, the linking inductance should be studied first.
The values of L_{ij} can be derived the same superposition methodology as the derivation of the star-point voltage in the star-point model. Figure 2.7 shows the Thevenin equivalent circuit that all the other sources are shorted and thus the impedance of other inductances are connected in parallel and grounded. Compared with Figure 2.1 of the DAB converter, another branch of Thevenin equivalent impedance is added between the leakage inductances of two ports, bringing a current path that influences the total equivalent inductance and power flow computation.
Assuming a comparatively large magnetizing inductance as in equation 2.10, the Thevenin equivalent inductance for all the other ports are computed by:

$$\begin{aligned} L'_{TH,X} &= \left(\frac{1}{L'_m} + \sum_{k=1,k\neq i,j}^{n} \frac{1}{L'_{\sigma k}} \right)^{-1} \\ &= \left(\sum_{k=1,k\neq i,j}^{n} \frac{1}{L'_{\sigma k}} \right)^{-1} \end{aligned} \tag{2.14}$$

And the star-point voltage of the Thevenin equivalent model can be computed from the contributions of only port #i and port#j:

$$V'_{TH,X} = \left(\frac{L'_{\sigma j} || L'_{TH,X}}{L_{\sigma i} + L'_{\sigma j} || L'_{TH,X}} \right) V'_i + \left(\frac{L'_{\sigma i} || L'_{TH,X}}{L_{\sigma j} + L'_{\sigma i} || L'_{TH,X}} \right) V'_j \tag{2.15}$$

In Figure 2.7, the excessive branch only contains the inductance thus no active power is consumed in this branch, therefore, the power transferred from port #i port #j, should be equal to the power from port #i to star-point, as well as the star-point to port #j, and the power can be written by analogy as follows:

$$\begin{aligned} P_{ij} &= \frac{V'_i V'_{TH,X}}{2\pi L'_{\sigma i}} \phi_{ij} \left(1 - \frac{|\phi_{ij}|}{\pi} \right) T_s \\ &= \frac{V'_j V'_{TH,X}}{2\pi L'_{\sigma j}} \phi_{ij} \left(1 - \frac{|\phi_{ij}|}{\pi} \right) T_s \end{aligned} \tag{2.16}$$

Combine equation 2.15 and equation 2.16, the power transferred from port #i and port #j can be derived:

$$P_{ij} = \frac{V'_i V'_j}{2\pi \left(L'_{\sigma i} + L'_{\sigma j} + \frac{L'_{\sigma i} L'_{\sigma j}}{L'_{TH,X}} \right)} \phi_{ij} \left(1 - \frac{|\phi_{ij}|}{\pi} \right) T_s \tag{2.17}$$

And the linking inductance in the Delta model in Figure 2.6 can be determined as:

$$L_{ij} = L'_{\sigma i} + L'_{\sigma j} + \frac{L'_{\sigma i} L'_{\sigma j}}{L'_{TH,X}} \tag{2.18}$$

Based on the equation 2.17 and 2.18, due to the presence of the term $L'_{TH,X}$, the ports and thus the power flow is inherently coupled, meaning that the circuit parameters of each port will affect the operation of all the other ports, which brings complexity in control scheme and implementation in real application scenarios. In the next section, the methods and solutions of resolving the coupling issues will be discussed.

2.4. Master-Slave Configuration

2.4.1. Qualitative Reasoning

Section 2.2 gives a brief insight into the MAB converter and the complexity in its power flow mechanism. In real implementations, the coupling feature of the typical MAB converter becomes a large obstacle in reliable operation in field application area. The operation of any pair of two ports will have influence on the other ports, and the linking inductance is dependent on the equivalent inductance of all the other ports.

However, a new hardware configuration that inherently decouples the ports and inter-port power flow was proposed in [16]. In this configuration, the leakage inductance of one port is minimized by a dedicated design of the multi-winding transformer, as demonstrated in Figure 2.8a. This asymmetrical configuration of leakage inductances makes one port a "master" port, and all the other ports are named "slave" ports.

With the help of the negligible inductance on the master port, the star-point in the star-equivalent model should follow the master port, and therefore the voltage waveform of V_1 should regulate the star-point voltage V_X. In this case, the power flow of all the slave ports will have a stable and identical "input" voltage source and the converter reaches a naturally decoupled power follow, as demonstrated in Figure 2.8b.

However, in real implementations, the leakage inductance cannot reach definite zero and designing the transformer with the asymmetrical leakage inductances is one key problem in this converter. The design details and the outcomes will be further discussed in the Chapter 6.

2.4.2. Numerical Reasoning

The equations derived previously also proves that the master-slave configuration naturally decouples the power flow of each slave ports. From equation 2.18, the term $L'_{TH,X}$ shows that the linking inductance between the master port (port #1) and any slave port (port #i, $i = 2, \cdots, n$) is dependent with the inductance distribution of other ports. Therefore, the manipulation of this term in equation is the most essential step in decoupling process.

The ideal outcome is that the linking inductance between a pair of master-slave ports independent of term $L'_{TH,X}$, while having an positive infinite inductances between any pair of slave-slave ports. This is naturally achieved by giving a master-port leakage inductance close to zero. With $L_{\sigma 1} \simeq 0$, the linking inductance will be approximated as:

$$L_{ij} = \begin{cases} L_{\sigma i} & i \neq 1, j = 1 \\ L_{\sigma j} & i = 1, j \neq 1 \\ \infty & i, j \neq 1 \end{cases} \tag{2.19}$$

This modified linking inductance will result in a more simplified power flow between ports that:

$$P_{ij} = \begin{cases} 0 & i, j \neq 1 \\ \frac{V'_i V'_j}{2\pi L'_{\sigma i}} \phi_{ij} \left(1 - \frac{|\phi_{ij}|}{\pi}\right) T_s & i \neq 1, j = 1 \\ \frac{V'_i V'_j}{2\pi L'_{\sigma j}} \phi_{ij} \left(1 - \frac{|\phi_{ij}|}{\pi}\right) T_s & i = 1, j \neq 1 \end{cases} \tag{2.20}$$

Equation 2.19 and equation 2.20 shows an ideal case that the power flow fulfills the requirements of decoupled MAB converter. However, in practical situations, the leakage inductance is non-zero and will affect the real value of linking inductance and therefore the

power flow of the converter. To evaluate the sensitivity of non-ideality in leakage inductance minimization, a series of non-zero master port leakage inductance values $L_{\sigma i}$ are assumed and applied in control system. According to the power flow equation of equation 2.17 and equation 2.18, the total current on the slave port output can be expressed as:

$$I'_j = \sum_{i=1, i\neq j}^{n} \frac{V'_i}{2\pi L_{ij}} \phi_{ij} \left(1 - \frac{|\phi_{ij}|}{\pi}\right) T_s \tag{2.21}$$

Where the linking inductance term L_{ij}, based on equation 2.18, should be:

$$\begin{aligned} L_{ij} &= L'_{\sigma i} + L'_{\sigma j} + \frac{L'_{\sigma i} L'_{\sigma j}}{L'_{TH,X}} \\ &= L'_{\sigma i} + L'_{\sigma j} + L'_{\sigma i} L'_{\sigma j} \left(\sum_{k=1, k\neq i,j}^{n} \frac{1}{L'_{\sigma k}} \right) \end{aligned} \tag{2.22}$$

In control systems design, equation 2.21 implied the MAB converter system in control system design that can be expressed by state variables that:

$$\mathbf{I'} = \begin{bmatrix} I'_1 \\ I'_2 \\ \vdots \\ I'_i \\ \vdots \\ I'_n \end{bmatrix} = \begin{bmatrix} G_{11} & G_{12} & \cdots & G_{1i} & \cdots & G_{1n} \\ G_{21} & G_{22} & \cdots & G_{2i} & \cdots & G_{2n} \\ \vdots & \vdots & \cdots & \vdots & \cdots & \vdots \\ G_{i1} & G_{i2} & \cdots & G_{ii} & \cdots & G_{in} \\ \vdots & \vdots & \cdots & \vdots & \cdots & \vdots \\ G_{n1} & G_{n2} & \cdots & G_{ni} & \cdots & G_{nn} \end{bmatrix} \begin{bmatrix} \phi_1 \\ \phi_2 \\ \vdots \\ \phi_i \\ \vdots \\ \phi_n \end{bmatrix} = \mathbf{G}\phi \tag{2.23}$$

However, the presence of ϕ_{ij} related terms suggests a non-linear system and a non-linear gain matrix **G**, therefore the system needs to be linearized in control systems design. This can be achieved by introducing Taylor expansion theorem that at a certain operation point SS, that:

$$I_i = I_{i,SS} + \Delta I_i \tag{2.24}$$

$$G_{ij,SS} = \frac{\partial I_{i,SS}}{\partial \phi_{ij}} \tag{2.25}$$

Therefore, the modified gain at operating point SS will be computed as:

$$G_{ij,SS} = \begin{cases} \sum_{k=1, k\neq i}^{n} \frac{V'_{k,SS}}{2\pi L_{ik}} \left(1 - \frac{2|\phi_{ik,SS}|}{\pi}\right) T_s & i = j \\ \frac{V'_{j,SS}}{2\pi L_{ij}} \left(1 - \frac{2|\phi_{ij,SS}|}{\pi}\right) T_s & i \neq j \end{cases} \tag{2.26}$$

And the small signal equation with modified small signal matrix gain at operation point **G'** will be:

$$\Delta\mathbf{I'} = \begin{bmatrix} \Delta I'_1 \\ \Delta I'_2 \\ \vdots \\ \Delta I'_i \\ \vdots \\ \Delta I'_n \end{bmatrix} = \begin{bmatrix} G_{11,SS} & G_{12,SS} & \cdots & G_{1i,SS} & \cdots & G_{1n,SS} \\ G_{21,SS} & G_{22,SS} & \cdots & G_{2i,SS} & \cdots & G_{2n,SS} \\ \vdots & \vdots & \cdots & \vdots & \cdots & \vdots \\ G_{i1,SS} & G_{i2,SS} & \cdots & G_{ii,SS} & \cdots & G_{in,SS} \\ \vdots & \vdots & \cdots & \vdots & \cdots & \vdots \\ G_{n1,SS} & G_{n2,SS} & \cdots & G_{ni,SS} & \cdots & G_{nn,SS} \end{bmatrix} \begin{bmatrix} \Delta\phi_1 \\ \Delta\phi_2 \\ \vdots \\ \Delta\phi_i \\ \vdots \\ \Delta\phi_n \end{bmatrix} = \mathbf{G'}\Delta\phi \tag{2.27}$$

In ideal cases from Figure 2.8a, the gain matrix **G'** should be diagonal and the control is fully decoupled. From equation 2.26, in non-ideal cases all the elements in the gain matrix **G'** is non-zero and thus implying that the control of each port is coupled.
To intuitively observe the extent of coupling, the ratio of non-diagonal elements with diagonal elements are quantified as the coupling index, and plotted with a gain matrix plot, as shown in Figure 2.9a to Figure 2.9f. In quantification process, normalized gain matrix is introduced that the diagonal elements are one unity. The value of leakage inductance of master port $L_{\sigma 1}$ is in normalized unit pu and the other leakages are all 1 pu. To simplify the calculation, the turns ratio, the source voltage rating are all identical, and the operation point is set at zero phase shift between any of the two ports.
It is observed that to achieve a converter with highly decoupled ports, the leakage inductance of port #1 should be at least two order of magnitudes lower than the base leakage inductance. This can be a benchmark in the hardware design, which will be further discussed in Chapter 6.

2.4.3. Practical Implementation

In practical design considerations, having a transformer with one minimized leakage inductance on one side, while keeping the leakage on all the other side significantly larger than this side is complicated. [16] proposed a novel configuration that with the help of adding external inductors on slave sides, which are modeled as "leakage" inductances, the normalized leakage inductance on master port can be reduced. The detailed configuration topology can be expressed in Figure 2.10.
To have a better decoupling performance, the external leakage inductor with high inductance should be selected. However due to the essence of power flow shown in equation 2.17, the high value of equivalent inductance is negatively correlated to the power rating and will limit the maximum power flow, thus it can be a bottleneck for operations of the converter. Therefore, this trade-off in practical design should be considered. The value choice and performance of decoupling will be further discussed in Chapter 6.

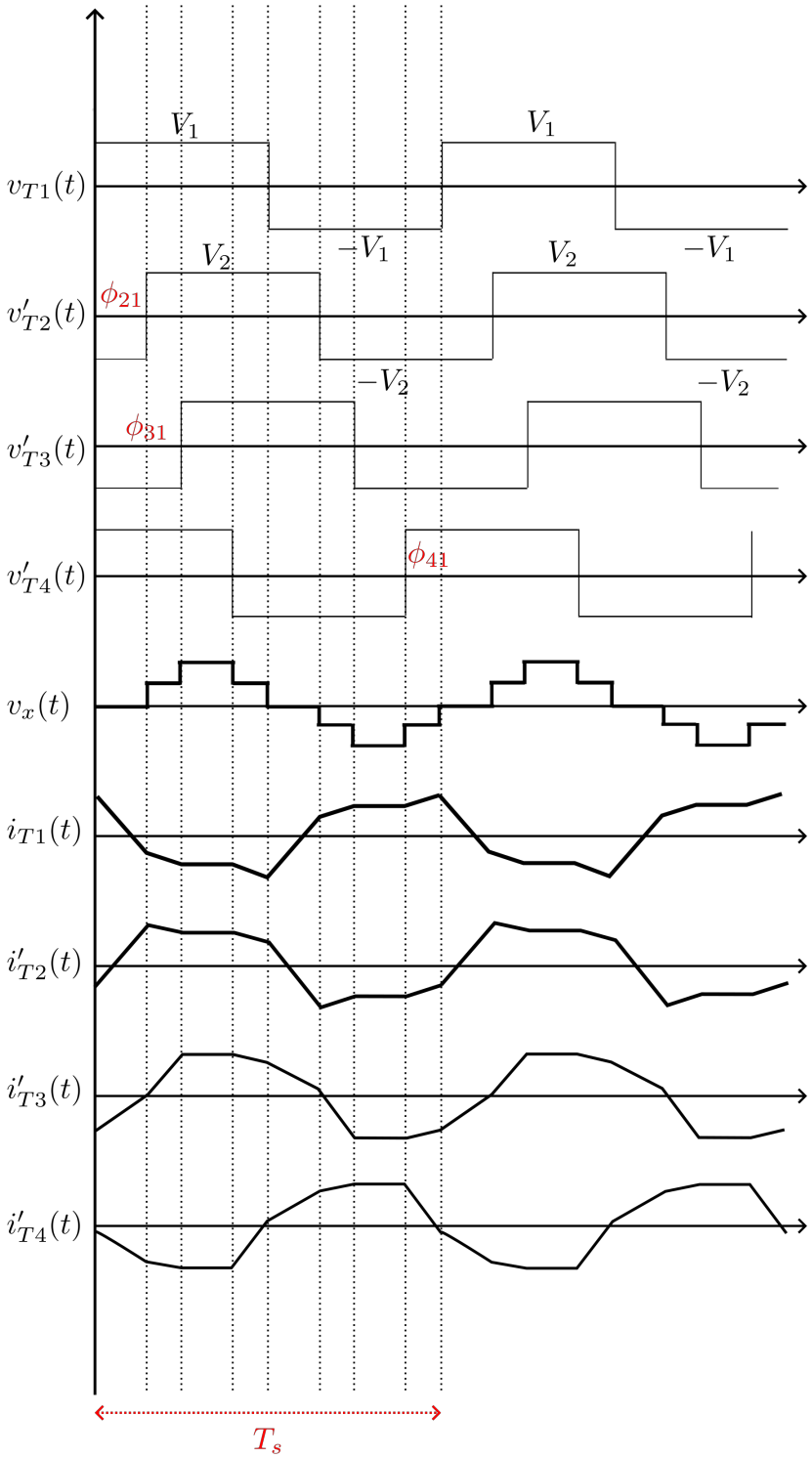

Figure 2.5: Idealized transformer voltage, star-point voltage and inductor current waveform of the four-port MAB converter, or the QAB converter.

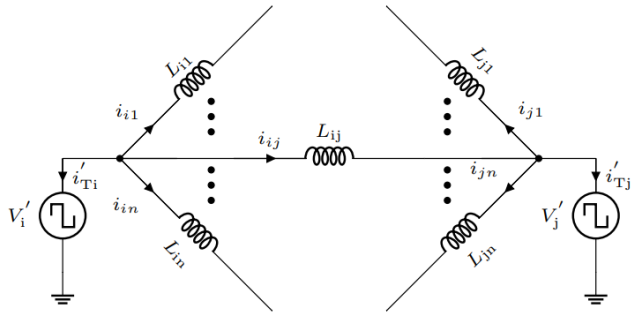

Figure 2.6: Port #i and port #j of the MAB converter in delta model [16].

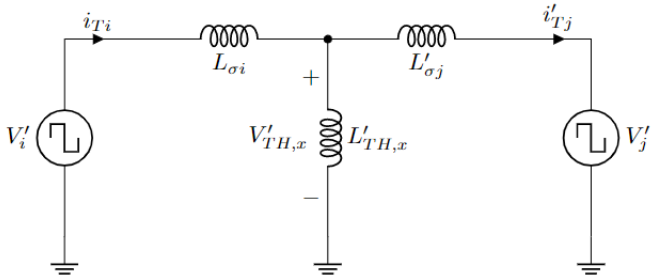

Figure 2.7: Port #i and port #j of the MAB converter in the Thevenin equivalent model. Only port #i and port #j are considered while all the other sources are grounded due to the superposition theorem, and their leakage inductances as well as magnetizing inductance are modeled as $L'_{TH,X}$.

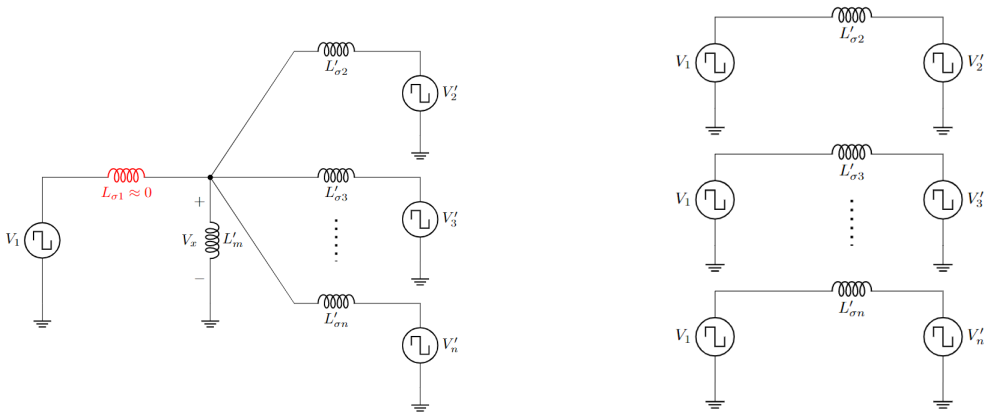

(a) Master-slave configuration

(b) Decoupled equivalent circuit

Figure 2.8: Master-slave configuration of the MAB converter. Port #1 is the master port with minimized leakage inductance, while all the other ports are slave ports and have significantly larger leakage inductances compared with port #1.

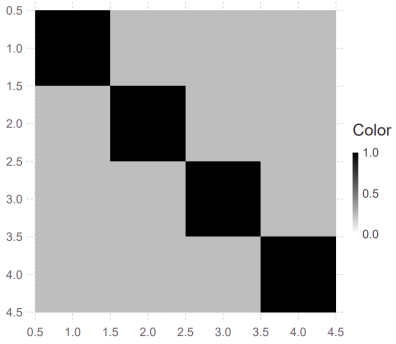

(a) $L_{\sigma 1} = 0.75pu$

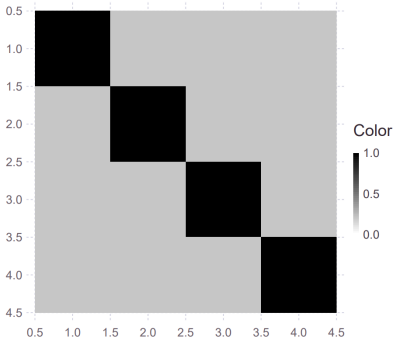

(b) $L_{\sigma 1} = 0.5pu$

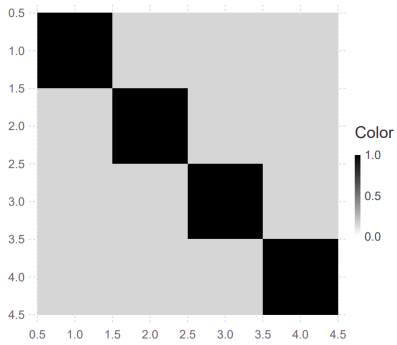

(c) $L_{\sigma 1} = 0.25pu$

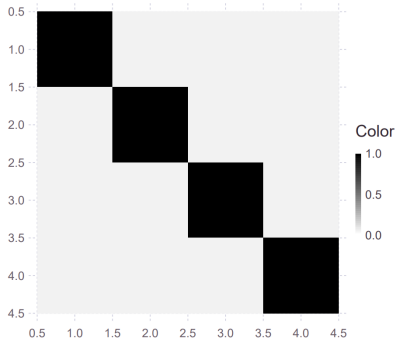

(d) $L_{\sigma 1} = 0.05pu$

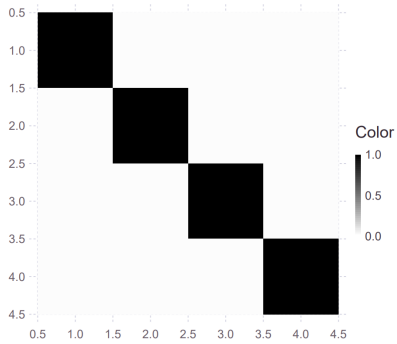

(e) $L_{\sigma 1} = 0.01pu$

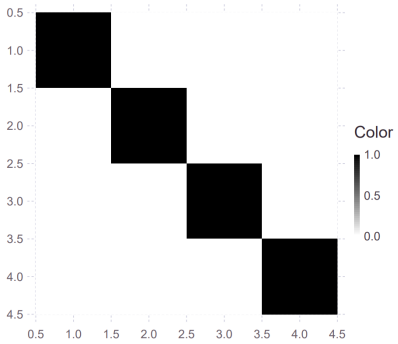

(f) $L_{\sigma 1} = 0.001pu$

Figure 2.9: Normalized gain matrix of the MAB converter with different value of normalized master port leakage inductance.

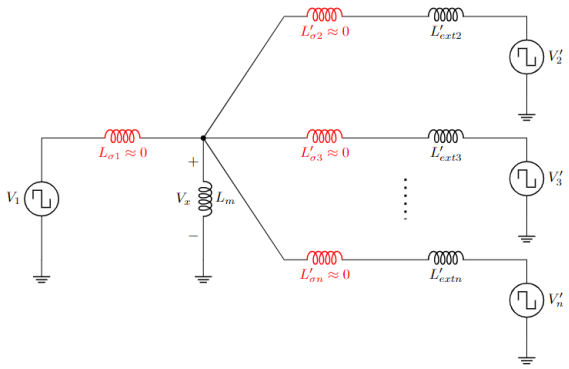

Figure 2.10: A practical implementation of master-slave configuration of the MAB converter. The inherent leakage inductance of all ports of the transformer is almost identical and close to zero, and external inductors are added to slave ports only.

3

Hot-Swapping Implementation

3.1. Overview and Potential Problems

In the application scenario of the MAB converter, availability issues are one potential bottleneck in mass application. The concept of availability means resilience to unexpected downtime is system operation. Therefore in this converter, if one port needs to be changed, the whole converter will have to be shut down, and this is not acceptable for some high-availability systems. Moreover the scalability is limited once the converter prototype is implemented, that the specifications of the ports are determined and unchangeable, which lowers the versatility of the converter in real applications.
Novel configuration of the converter introduced in this paper allows a hot-swapping capability of the converter. In this modified MAB converter, it allows the port swapping while keeping all the rest of the converter alive. Figure 3.1 demonstrates a generic concept of this new configuration. In practical applications of the MAB converter, the load that connects the output of slave sides can be either voltage source or passive load. The difference of load profile will have influences on the operation details of the MAB converter hot-swapping. In the next subsections, two types of loads will be discussed, and the affect they will have on plugging-in and plugging-out operation of slave boards are thoroughly studied.

3.1.1. Case I: Voltage Source Load

To simplify the circuit demonstration, only one slave port, which equals to the DAB converter is sketched and discussed in this and following case analyses. Therefore, the MAB converter, with only one slave sides that is loaded with a voltage source, is sketched in Figure 3.2. According to the circuit simplification process in Chapter 2, this hot-swapping configuration can also be modeled as Figure 3.3
The essence of the MAB converter and the DAB converter suggests that the master active bridge and slave active bridge works independently. This will brings two major reasons that contributing to the potential problems of hot-swapping:

1. The voltage ratings of master side and slave sides can be different.

2. The auxiliary power of slave side can be provided from slave voltage source, and thus the active bridge can be constantly activated without connecting to the master side. However the active bridge is not synchronized before plugged in.

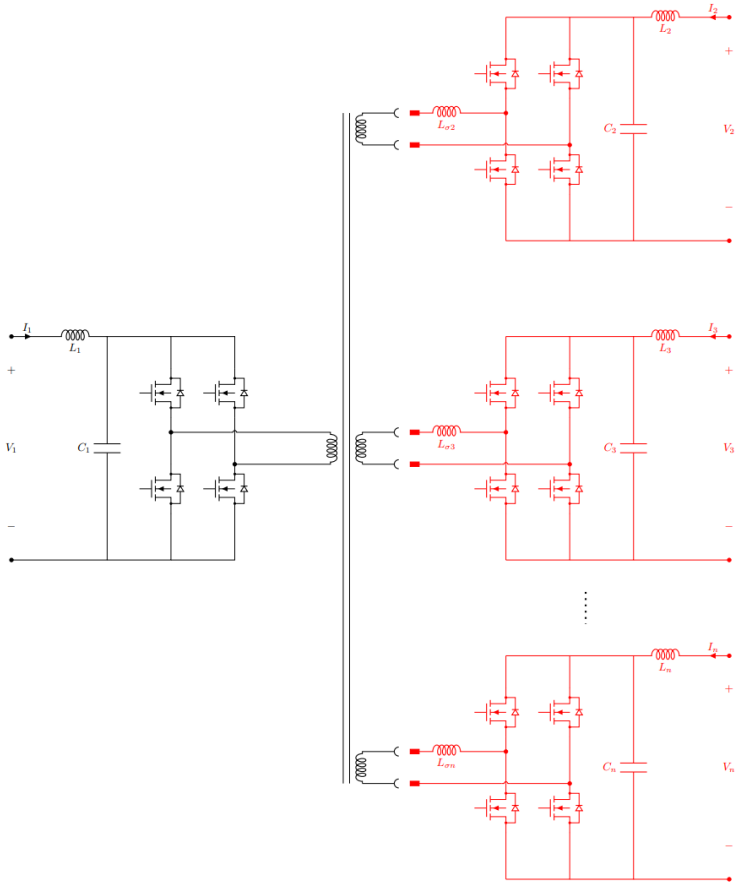

Figure 3.1: The hot-swapping configuration of the MAB converter. The sockets and plugs are applied to the transformer windings and slave modules. The parts colored in red are all modular and hot-swappable while the rest of the converter are stationary.

Moreover, the original states of the converter before plugged-in or plugged-out should be defined, to evaluate the transient performance of hot-swapping.

Plugging-in

For plugged-in process, the original current that flows through the leakage inductance and the secondary transformer winding is zero. However the cases will vary with the different load profile and phase of active bridge. To discuss the worst case scenario, the voltage rating on the master side and slave side is set non-identical, and the phase shift between master side and slave side is defined non-zero in this case study. Considering a original state that the current is zero, therefore, the voltage and current waveform upon insertion will be shown in Figure 3.4.

However, Figure 3.4 is not able to demonstrate the whole transient process since the current will not reach a steady state. The first period of operation after insertion of the plug, it can be approximated as a quasi-equilibrium state and the peak value and the root-mean-square (RMS) value of the first-period current waveform can be approximated as:

$$I_{peak0} = \frac{V_1 + V_2}{L'_{\sigma 2}} \cdot \frac{\phi}{2\pi} \cdot T_s + \frac{V_1 - V_2}{L'_{\sigma 2}} \cdot \frac{\pi - \phi}{2\pi} \cdot T_s \tag{3.1}$$

$$
\begin{aligned}
I_{rms0}^2 &= \frac{1}{T_s}\int_0^{T_s} i_\sigma(t)^2\,dt \\
&= \left(\frac{V_1+V_2}{L'_{\sigma 2}}\cdot\frac{\phi}{2\pi}\cdot T_s\right)^2\cdot\frac{\phi}{6\pi} \\
&+ \left(3I_{peak0}^2 - 3I_{peak0}\cdot\frac{V_1-V_2}{L'_{\sigma 2}}\cdot\frac{\pi-\phi}{2\pi}\cdot T_s + \left(\frac{V_1-V_2}{L'_{\sigma 2}}\cdot\frac{\pi-\phi}{2\pi}\cdot T_s\right)^2\right)\cdot\frac{\pi-\phi}{6\pi} \\
&+ \left(3I_{peak0}^2 - 3I_{peak0}\cdot\frac{V_1+V_2}{L'_{\sigma 2}}\cdot\frac{\phi}{2\pi}\cdot T_s + \left(\frac{V_1+V_2}{L'_{\sigma 2}}\cdot\frac{\phi}{2\pi}\cdot T_s\right)^2\right)\cdot\frac{\phi}{6\pi} \\
&+ \left(\frac{V_1-V_2}{L'_{\sigma 2}}\cdot\frac{\pi-\phi}{2\pi}\cdot T_s\right)^2\cdot\frac{\pi-\phi}{6\pi}
\end{aligned}
\tag{3.2}
$$

From equation 3.1 and equation 3.2, the current that delivers to the slave sides will be non-zero once the plug is inserted to the socket, and when the voltage rating is constant, the worst case scenario will happen with a phase shift of $\phi = \pi$ that:

$$I_{rms0,max} = \frac{1}{2\sqrt{3}}\cdot\frac{V_1+V_2}{L'_{\sigma 2}}\cdot T_s \tag{3.3}$$

$$I_{peak0,max} = \frac{1}{2}\cdot\frac{V_1+V_2}{L'_{\sigma 2}}\cdot T_s \tag{3.4}$$

After the insertion, the controller and synchronization process activates and the phase shift will gradually reach zero, and thus a zero RMS current goes through the leakage inductor at steady state. The current behavior whole process of plugged in can be sketched in Figure 3.5.

Moreover, this surge current will cause a surge power flow into the slave side. The average power in one period can also be computed according to the power derivation in Chapter 2, and the average power in the first period is:

$$P_0 = \frac{V_1 V_2}{L'_{\sigma 2}}\cdot\phi\left(1-\frac{|\phi|}{\pi}\right)\cdot T_s \tag{3.5}$$

Considering the equation 3.3 and equation 3.5 , this overshoot current and overshoot power at the beginning can be larger than the rated parameters of the converter and therefore, a current limiting methods shall be applied to limit this excessive power, and it will be discussed in Section 3.2.

Plugging-out

While for plugged-out step, the current flows through the inductor components in the loop can be non-zero. This can bring damaging problems due open circuit for branch that contains power stored in inductors, and the surge overshoot voltage appeared on the socket and plug will be:

$$V_{socket} = I_{sec}\cdot R_{open,socket} \tag{3.6}$$

$$V_{plug} = I_\sigma\cdot R_{open,plug} \tag{3.7}$$

Where the open circuit can be modeled as an large value resistor $R_{open,socket}$ and $R_{open,plug}$, which is modeled as the circuit that contains an air gap. The value of surge voltage when plugged out can be extremely high and hazardous to the operation of the converter and surroundings.

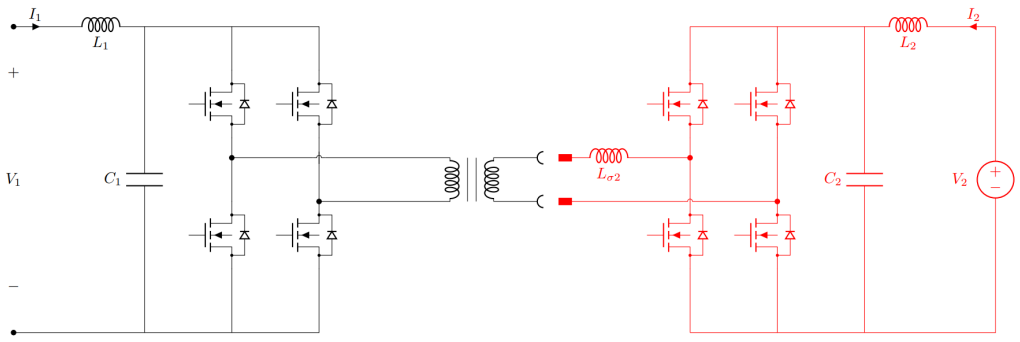

Figure 3.2: The hot-swapping configuration of the MAB converter with voltage source load. To simplify the circuit only one slave port is shown and discussed.

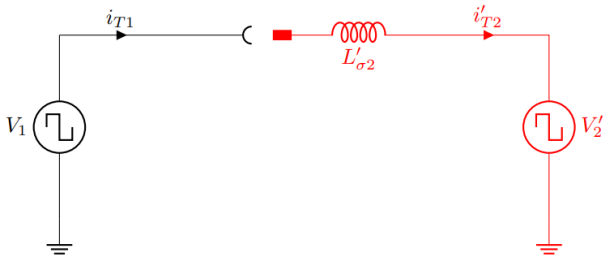

Figure 3.3: The equivalent model of hot-swapping configuration of the MAB converter with voltage source load, both the source and load are represented with a square wave voltage source. To simplify the circuit only one slave port is shown and discussed.

3.1.2. Case II: Passive Load

In other cases, the loads are passive load, and in circuit analysis of this research they can be modeled as a constant-value resistor, as shown in Figure 3.6. This case also demonstrates a MAB converter with only one slave side for simplicity. Due to the essence of passive resistor load, the output power, output voltage should follow the basic electrical circuit law that:

$$V_{load} = \sqrt{P_{load} \cdot R_{load}} \tag{3.8}$$

Plugging-in

Equation 3.8 suggests that the output voltage depends on the active power transferred from the master side to the slave side. Therefore, before the slave side is plugged into the master module, the power flow is absent and therefore the initial voltage on the slave output is zero.

The zero voltage on the slave side also lead to practical problems in semiconductor aspect. In the hot-swapping process of independent power modules in the MAB case, the power for auxiliary power supply is either from the plug, as shown in Figure 3.7, or from the slave DC bus, which is the similar to the voltage-source-load case demonstrated in Figure 3.8, thus the plugging action is always prior to activation of active bridges and other active components of the circuit board.

The lack of auxiliary power makes the switches in the active bridge not be activated and behave as passive components. For typical SiC and Si MOSFET, the body diode or exter-

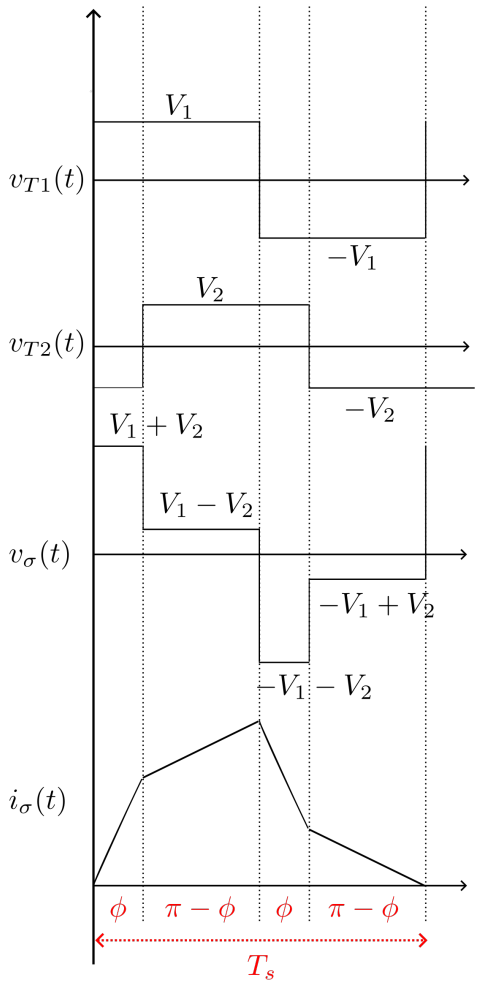

Figure 3.4: The waveform of the first period of operation of the MAB converter with voltage source load after the plug is inserted into the socket. The initial current of the inductor and transformer is assumed to be zero.

nal reversely-connected diode provides a current path for reverse conduction. While for the GaN HEMT, the 2-Dimension Electron Gas (2DEG) of HEMT structure provides a reverse conduction channel, which behaves like a natural diode, as demonstrated in Figure 3.9 [17], [18]. Therefore, the reverse conduction characteristics of most normally-on transistors suggests a diode characteristics in reserve conduction mode with inactivated gate signal.

Therefore, considering the time delay of power supply, the slave active bridge will behave as a diode bridge rectifier in the transient process of the plug insertion. Figure 3.10 depicts the concept of “active bridge to diode bridge rectifier” transient state of the MAB (DAB) converter. When the output filter is considered, the output voltage is assumed to be constant zero for the first few periods after insertion. As a result the slave side is shorted and grounded, and the equivalent circuit for this hot-swapping configuration with passive load can be redrawn as Figure 3.11.

This transient state of the converter will lead to two specific problems that requires to be dealt with for safe operation of insertion, which are:

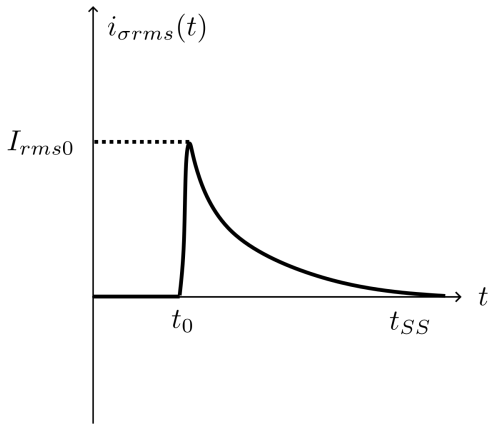

Figure 3.5: The RMS current after plug insertion of the hot-swappable MAB converter with voltage source load. Time t_0 is the time of insertion and t_{SS} is the time that the converter reaches a steady state and thus a zero RMS current.

1. The high inrush current when the slave module is plugged into the socket, due to a very high voltage difference of master and slave side DC buses.

2. The unexpected and uncontrolled power flow from master port to slave port with inactivated switch bridge on the slave side at steady state.

For the first problem, the current waveform for the first period after insertion that appeared on the leakage inductor, or the plug and socket is elaborated in Figure 3.12. Since only one square wave voltage source is considered, the peak current can be simply computed that:

$$I_{peak0} = \left| \frac{V_1}{L'_{\sigma 2}} \cdot \frac{\pi - \phi}{2\pi} \cdot T_s \right| \tag{3.9}$$

Therefore, the maximum and minimum first-period current I_{peak0} can be obtained that:

$$\begin{cases} I_{peak0,max} = \frac{V_1}{2L'_{\sigma 2}} \cdot T_s, & \phi = 0, \pi \\ I_{peak0,min} = \frac{V_1}{4L'_{\sigma 2}} \cdot T_s, & \phi = \frac{\pi}{2}, -\frac{\pi}{2} \end{cases} \tag{3.10}$$

The absence of auxiliary power and the essence of diode-bridge-rectifier does not only affect the inrush current, but also result in excessive power flow at steady state, as described in the second problem. The steady state in inactivated slave bridge means the voltage on load is uncontrollably charged to a constant non-zero value, as demonstrated in Figure 3.13. Under this situation, the current and voltage waveform, and the corresponding circuit topologies are demonstrated in Figure 3.14 and Figure 3.15. Theoretically, the whole converter should have the following features

1. Due to the presence of DC bus capacitor, under steady state situations, the load can be regarded as a voltage source in diode bridge rectifier analysis.

2. The RMS value of the absolute current on the leakage inductor is the RMS current transferred to the load.

3. The load voltage is lower than the master side DC voltage. If this is not true, the diode bridge rectifier is blocked and the power flow is zero. With a zero power flow the load voltage is zero, which contradicts the assumption that the load voltage is higher than the source voltage.

To quantitatively estimate the load voltage and power, based on the relations mentioned above, if the constant d is defined as the duty ratio that state (a) or state (c) occupies an half period, the equations can be set that:

$$I_{mean} = \frac{1}{2} \cdot \frac{V_1' - V_{load}}{L_{\sigma 2}} \cdot d \cdot \frac{T_s}{2} \tag{3.11}$$

$$I_{rms} = \sqrt{\frac{13}{12} \cdot I_{mean}^2} \tag{3.12}$$

$$\left(V_1' - V_{load}\right) \cdot d = \left(V_1' + V_{load}\right) \cdot (1 - d) \tag{3.13}$$

$$I_{rms} = \frac{V_{load}}{R_{load}} \tag{3.14}$$

With the help of this equation set, the steady state load voltage before slave bridge activation can be obtained, and is a non-zero value, which verifies that the existence of an unexpected power flow for the MAB converter with passive load in hot-swapping process. The RMS current that is delivered to the load can be sketched as in Figure 3.16. Compared with a voltage source load, there are two major differences in plugging in action:

1. The converter with passive load will have lower inrush current upon insertion, but still not negligible, and requires inrush current limiting methods for safety and reliability of components.

2. An excessive power flow exists before the auxiliary power is obtained for slave side active bridge. In applications an immediate activation process is necessary for ideal operation of the MAB converter.

Plugging-out
As for the plugged out action of the MAB converter with passive load, it is similar to the case of voltage source load as in equation 3.6 and equation 3.7. Therefore, it also leaves potential danger for plugging out, and the solution for surge voltage suppression should be similar to case I, which will be elaborated in the next sections.

3.2. Surge Current Limiting

3.2.1. Description of NTC

The NTC resistor, which is short for Negative-Temperature-Coefficient resistor, possesses a feature that the resistance of the resistor is negatively related with the component temperature. The NTC is a non-linear passive component and therefore can be a simple and cost-effective method for inrush current limiting implementation. A typical resistance-temperature is sketched in Figure 3.17.
In the circuit, the operation state will change the temperature of the NTC resistor, and can be quantitatively computed by the power dissipated on the NTC and the thermal parameters of the resistor. This temperature change will have influence on the resistance which

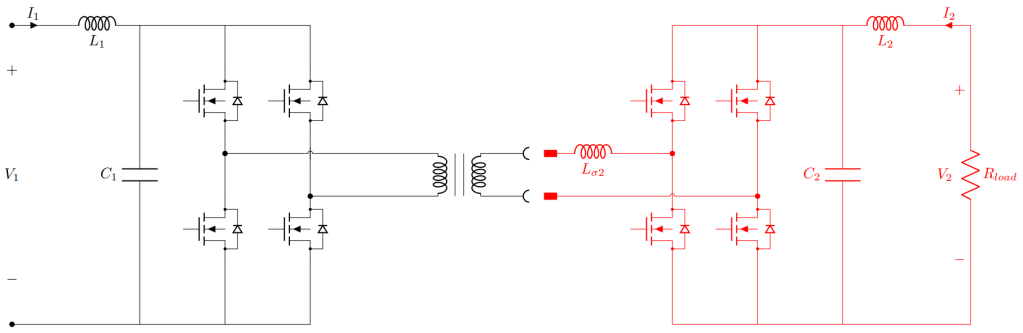

Figure 3.6: The hot-swapping configuration of the MAB converter with a passive component load, which is represented by a constant resistor. To simplify the circuit only one slave port is shown and discussed.

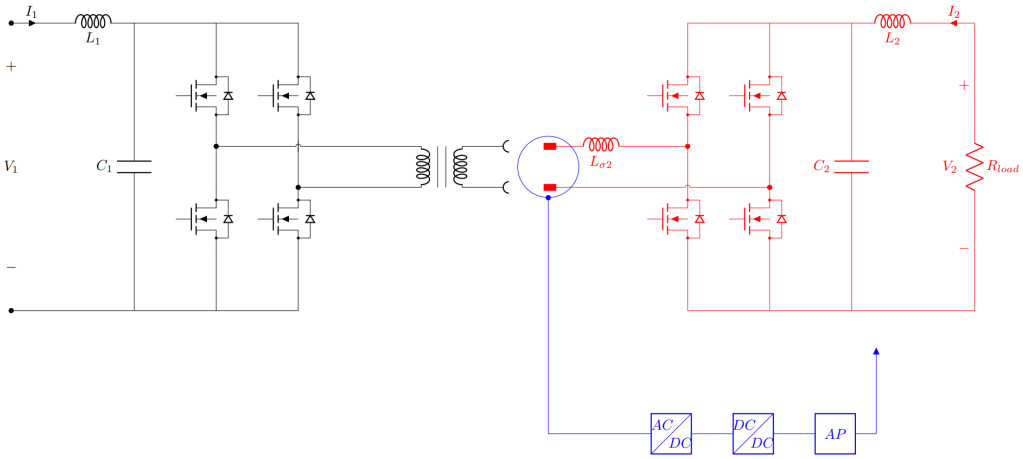

Figure 3.7: The configuration of auxiliary power supply (short for “AP” in the block diagram) of the slave module from the plug. To simplify the circuit only one slave port is shown and discussed.

eventually affect the state of the circuit. The resistance of the NTC under ambient temperature and at steady state can be obtained in the following equations:

$$R_{NTC,ambient} = R_{NTC}|_{@T=T_{ambient}} \tag{3.15}$$

$$R_{NTC,SS} = R_{NTC}|_{@T=\left(\frac{I_{rms}^2 R_{NTC,SS}}{R_{TH}} + T_{ambient}\right)} \tag{3.16}$$

Therefore, the computation of resistance at steady state can be intuitively sketched as shown in Figure 3.18. The resistance at steady state is a crossing point of the inherent R-T curve of the NTC resistor, and the temperature line of the resistor. Therefore, the characteristics of the NTC in circuits can be briefly summarized that:

1. High resistance before operation and upon activation.

2. Low resistance at steady state operation.

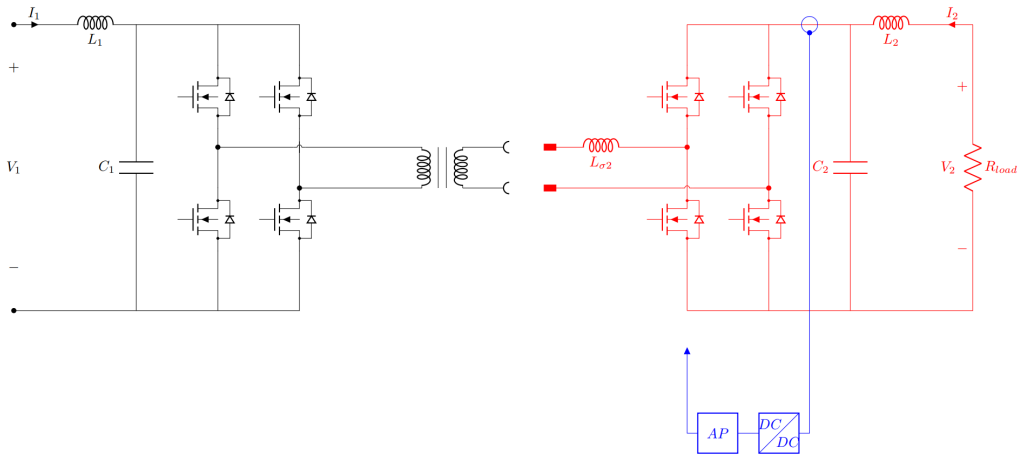

Figure 3.8: The configuration of auxiliary power supply (short for AP in the block diagram) of the slave module from the DC bus. To simplify the circuit only one slave port is shown and discussed.

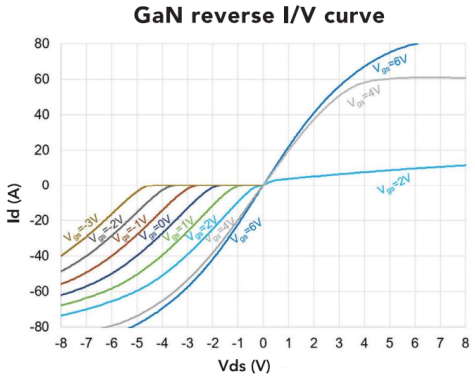

Figure 3.9: The conduction I-V curve for GaN enhancement-mode HEMT. The third-quadrant operation is similar to reverse diode [17].

3.2.2. Implementation of NTC in Hot-Swapping

In the MAB converter with hot-swapping slave modules, the NTC resistor can be inserted between the plug and the external inductor, as demonstrated in Figure 3.19. And the equivalent circuit upon insertion is re-drawn as Figure 3.20. Therefore with the applied square wave from the master side, the current on the leakage inductor can be regarded as a current response of a first-order RL system under voltage input, and can be computed by:

$$i_\sigma = \frac{V_1}{R_{NTC,ambient} + sL'_{\sigma 2}} \tag{3.17}$$

The modified current waveform and its comparison with original current can be plotted in Figure 3.21, with the time constant of curve that $\tau = \frac{L'_{\sigma 2}}{R_{NTC,ambient}}$. From the plot it is intuitively derived that the NTC at ambient temperature have larger resistance will present a better performance in inrush current limiting.

At steady state operation, the NTC is expected to heated up to a constant temperature and result in a negligible value in the circuit, and the equivalent circuit will shown in Figure 3.22. This feature of resistance change during operation of the NTC proves the ability of

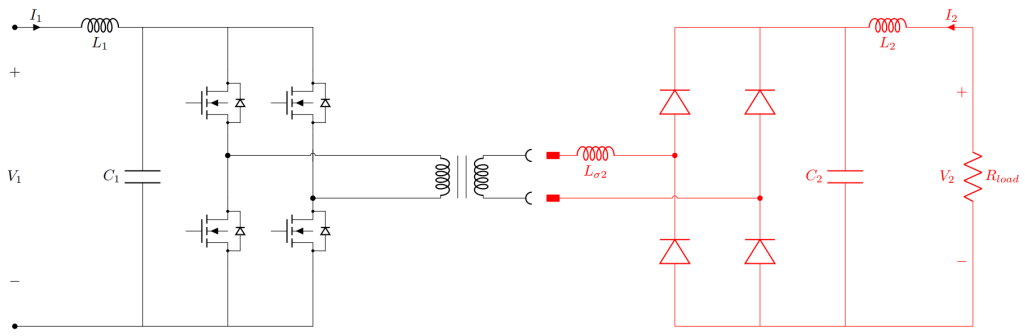

Figure 3.10: The equivalent circuit of the MAB converter with inactivated slave module. The active bridge on the slave side is replaced by a diode bridge rectifier. To simplify the circuit only one slave port is shown and discussed.

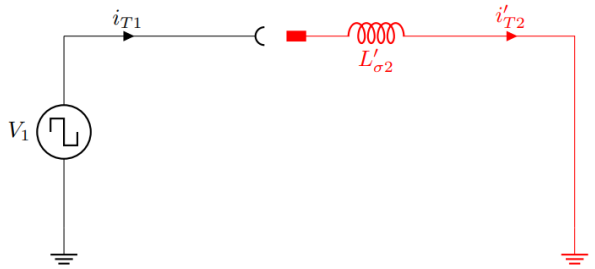

Figure 3.11: The equivalent circuit of hot-swapping configuration of the MAB converter with a passive load within the first cycle, the load voltage is zero and can be approximated as a short circuit. To simplify the circuit only one slave port is shown and discussed.

inrush current limiting at plugging-in actions of the hot-swappable MAB converter.
For the slave ports with voltage load, the NTC resistor should satisfy the following two qualitative requirements, which suggests the distance of two resistances appeared on the Figure 3.18 should be as far as possible.

1. The resistance at initial situation is as high as possible.

2. The resistance during steady-state operation is as low as possible.

For the slave ports with resistive load, the NTC resistor should fulfill the following two quantitative requirements for optimum operation, and can be intuitively demonstrated in Figure 3.23. that

1. The resistance should be much larger than load resistance at ambient temperature.

2. The resistance should be much smaller than the load resistance during steady-state operation.

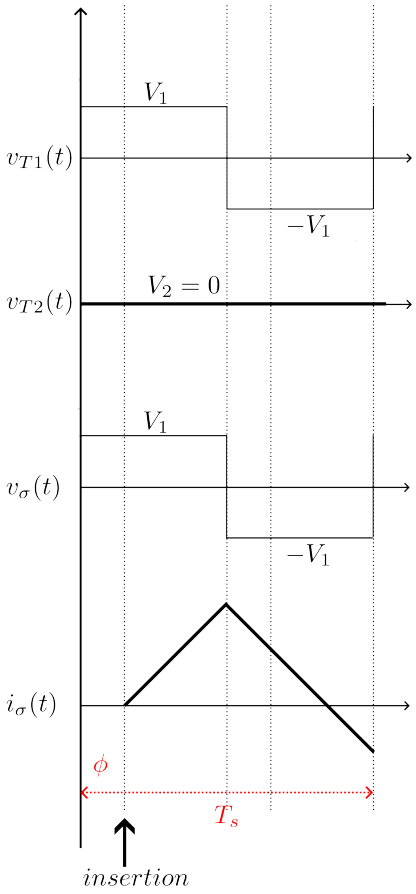

Figure 3.12: The waveform of the first period of operation of the MAB converter with passive load after the plug is inserted into the socket. The initial current is zero, and the insertion action has a phase delay of ϕ.

3.3. Surge Voltage Limiting

3.3.1. Description of MOV

The MOV is an abbreviation for Metal-Oxide-Varistor. The MOV can regulate the voltage over a wide current range, and can be modeled as a non-linear passive component that the resistance is determined by the current that flows through the resistor. From low current to high current, the operation region of MOV can be categorized into three regions, as demonstrated in Figure 3.24, which are:

1. $I < I_{leakage,max}$, high resistance region.

2. $I_{leakage,max} < I < I_{breakdown}$, low resistance region, or voltage-clamping region.

3. $I > I_{breakdown}$, breakdown region.

At current lower than the maximum leakage current $I_{leakage,max}$, the MOV behaves as a high-resistance resistor, which ensures that the MOV does not influence the normal operation of the circuit and the branch with an MOV can be regarded as an open circuit.

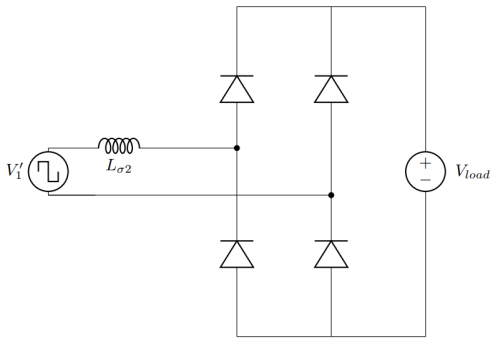

Figure 3.13: The equivalent circuit of the MAB converter with inactivated slave bridge. Unlike previous equivalent circuit, the master side parameters is referred to the slave side and the voltage source is a square wave source with a voltage V_1'.

With current higher than the maximum leakage current, the voltage will no longer rise with the increasing current but will be clamped at a certain level, and the voltage in this case is named the clamping voltage $V_{clamping}$. Under ideal situations and circuit analysis the $V_{clampmg}$ is normally assumed as a constant value for all current higher than $I_{leakage,max}$ and before the MOV reaches breakdown, but in non-ideal cases, the clamping voltage rises slowly with the increasing current. In this region, the equivalent resistance of the MOV drastically drops, and result in a low-resistance region.
Finally as the current through MOV increases above a critical value of $I_{breakdown}$, the MOV reaches a breakdown state. At this state, the MOV can no longer clamp the voltage and the equivalent resistance will increase.

3.3.2. Implementation of MOV in Hot-Swapping

In the MAB converter with hot-swapping slave modules, the MOVs are placed in parallel with the plug and the socket of the hot-swapping module, which is demonstrated in Figure 3.25. The equivalent circuit of this dedicated configuration of MAB converter with MOV connected in parallel with the plug and the socket on the hot-swapping ports can be redrawn as Figure 3.26. The MOVs on the slave side helps to dissipate the energy stored in the external inductors, while the MOV on the socket side aims to release the energy from the equivalent virtual leakage inductances in non-ideal situations, although the leakage is assumed to be minimal in this thesis.
The normal opeartion and removal transient of hot-swappable MAB converter with MOVs on plug and socket can be demonstrated in Figure 3.27a and Figure 3.27b respectively, and the waveform of MOV during operation is sketched in Figure 3.28. Under normal operations, the MOV should cause minimum interference to the original circuit, thus a sufficiently large resistance, which can be approximated as an open circuit for the MOV is required under any circumstances except for plugging-out action. In this case the MOV is expected to operate in high-resistance region to be ignored, therefore, the rated voltage on the plug should be below the clamping voltage and a small leakage current exists in the MOV branch.
During the plugging-out transient process, the original current loop on the main circuit is

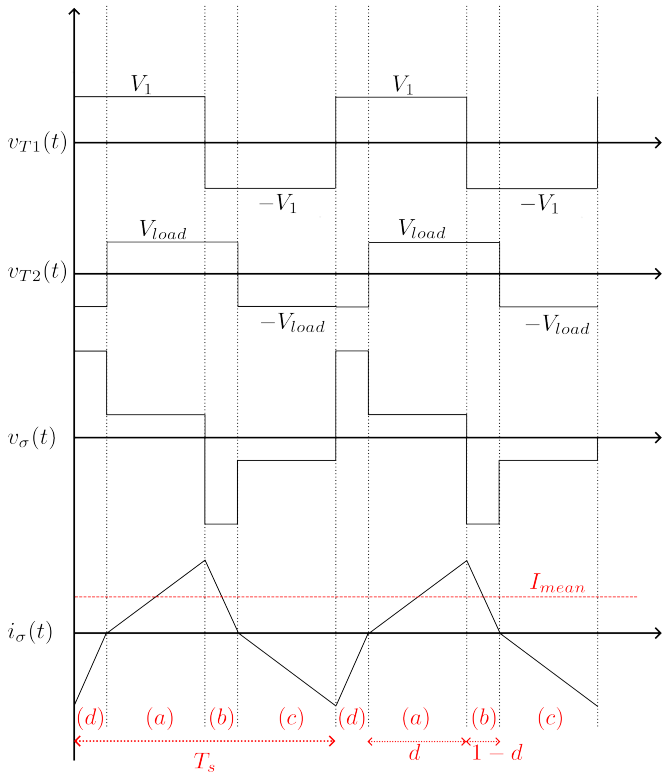

Figure 3.14: The waveform of voltages and current for the MAB converter with diode bridge rectifier on the slave side. Any operation period should contains state (a), (b), (c) and (d) consecutively. The square voltage appeared before the diode bridge, which is denoted as V_{T2}, should have the same direction with the leakage current.

disconnected from the plug, the current on this main loop is forced to flow through the MOV branch. And the value of the current on MOV equals the original current on the external inductor. The current on MOV at this transient should drive the MOV into low-resistance region for safe operation with clamped voltage on the plug. Therefore, under the worst case the current on the inductor reaches its maximum, this current should be larger than the maximum leakage current $I_{leakage,max}$ of MOV, but below the breakdown current $I_{breakdown}$ to avoid the breakdown region of MOV.
Therefore, the selection for the MOV in hot-swapping circuit should meet the following two requirements, and can also be intuitively drawn in Figure 3.29.:

1. The maximum current on AC side should fall in the range between $I_{leakage,max}$ and $I_{breakdown}$.

2. The operating voltage on the plug should be lower than the clamping voltage $V_{clamping}$.

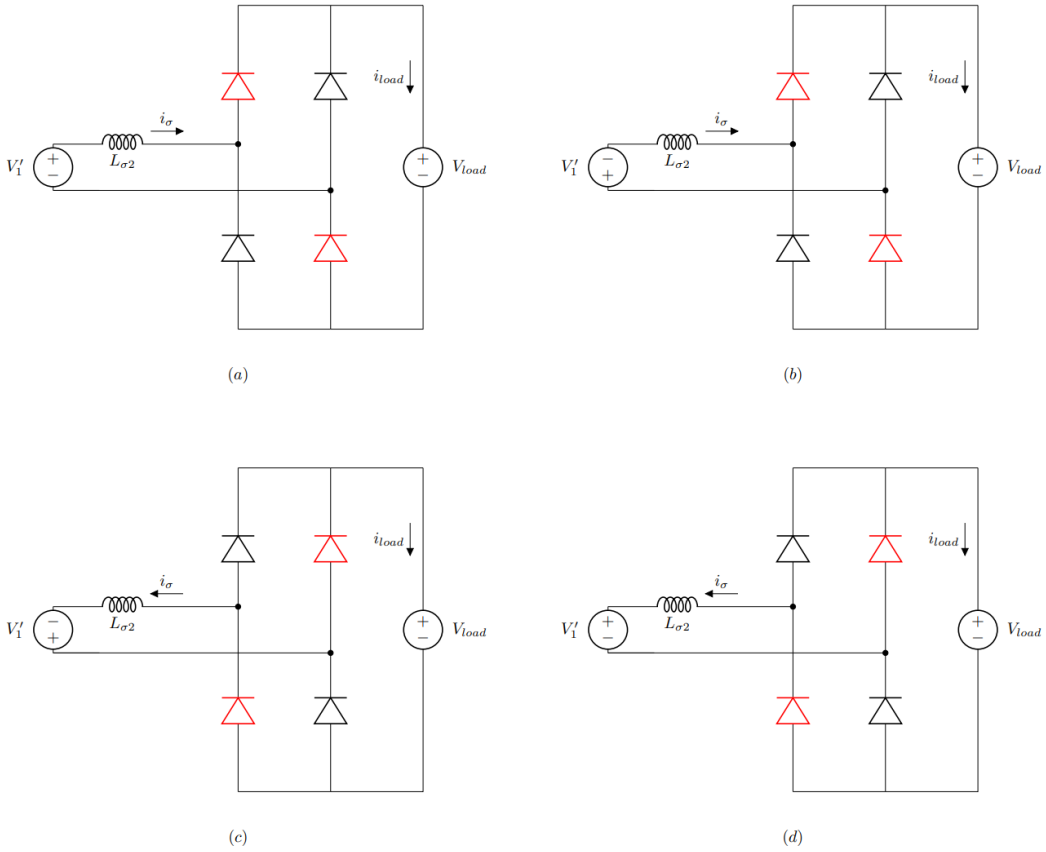

Figure 3.15: The four operation states of the MAB converter with diode rectifier bridge on the slave side. The four states are caused by the two directions of source voltage V_1' and two directions of leakage current i_σ. Due to different current direction, corresponding diodes that form circuit power flow loop are marked in red. For simplicity only one slave port is shown and discussed in this sketch.

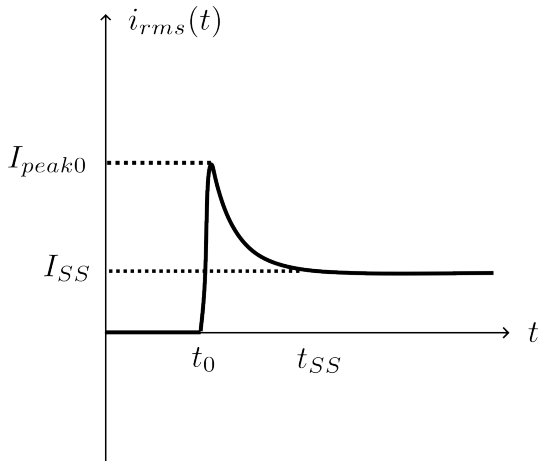

Figure 3.16: The RMS current behavior after plug insertion of the hot-swappable MAB converter with passive load. Time t_0 is the time of insertion and t_{SS} is the time that the converter reaches a steady state with non-zero RMS current.

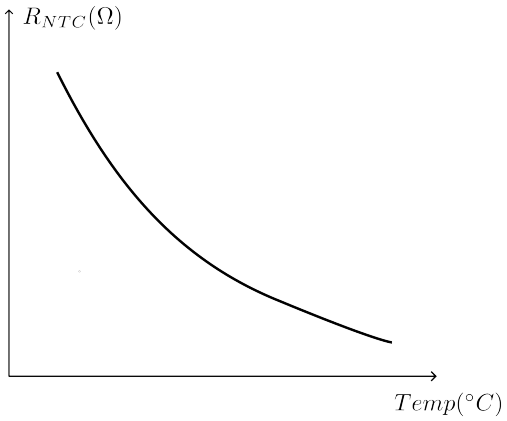

Figure 3.17: The typical R-T curve for NTC resistor.

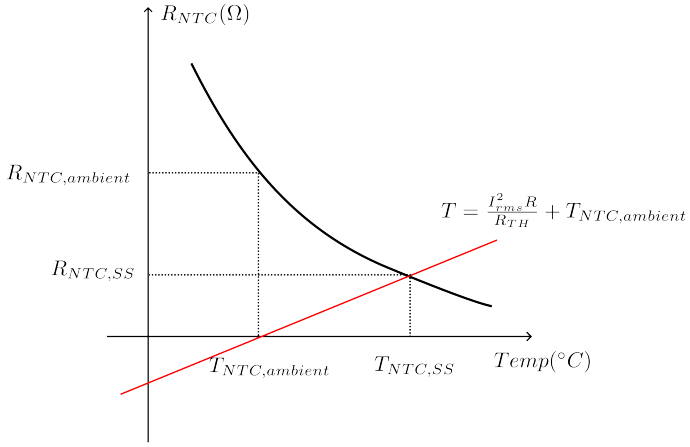

Figure 3.18: The intuitive demonstration of computation of NTC resistance at steady state operation, given that the resistance of the NTC is comparatively much smaller than the equivalent resistance of the circuit, thus the effective current I_{rms} is the current rating of the original circuit.

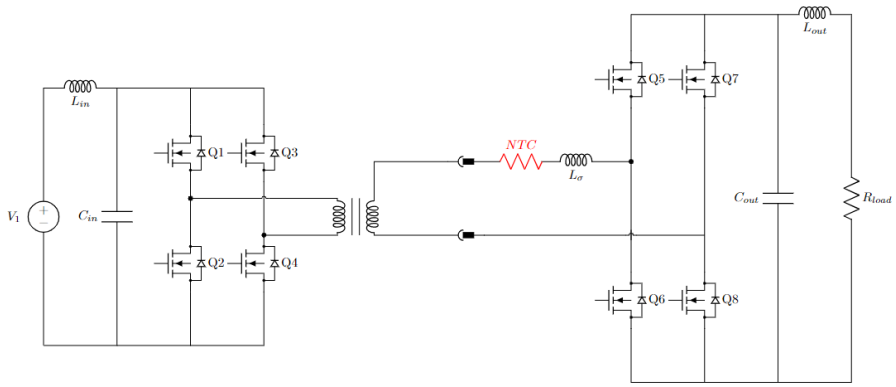

Figure 3.19: The application of NTC resistor in hot-swappable slave ports.

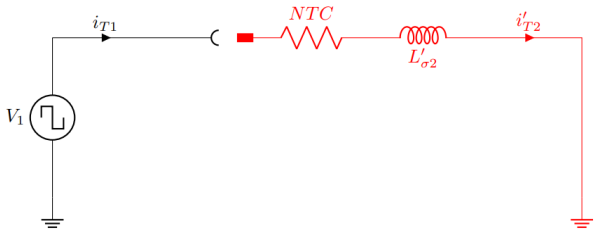

Figure 3.20: The equivalent model of the MAB converter with an NTC resistor. To simplify the circuit only one slave port is demonstrated.

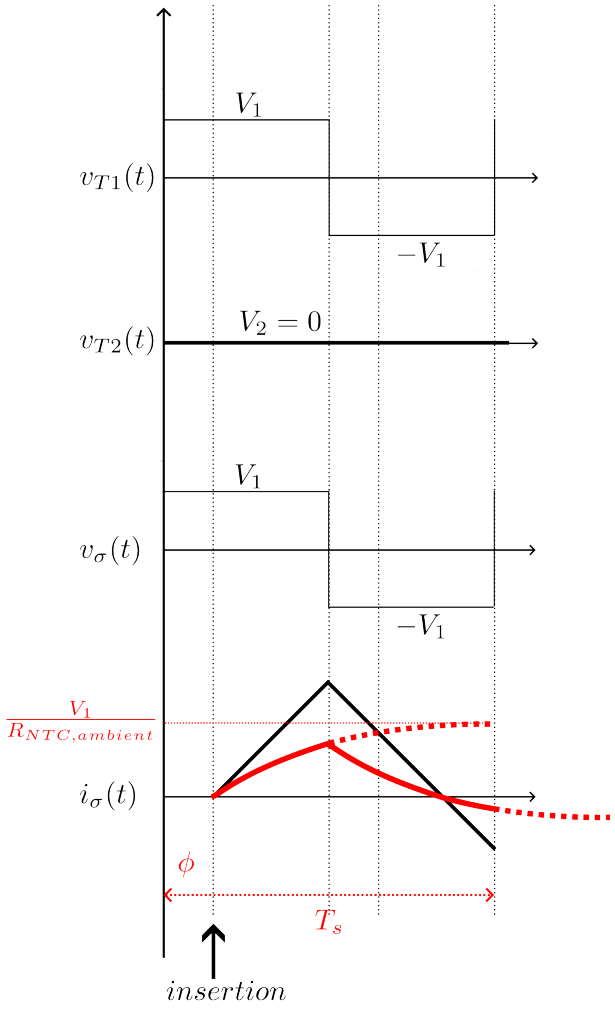

Figure 3.21: The waveform of the voltages and current of hot-swappable converter of the first period. The NTC resistor is in a quasi-static state and can be approximated as a constant-value resistor. The current is suppressed compared with the converter without current limiting components.

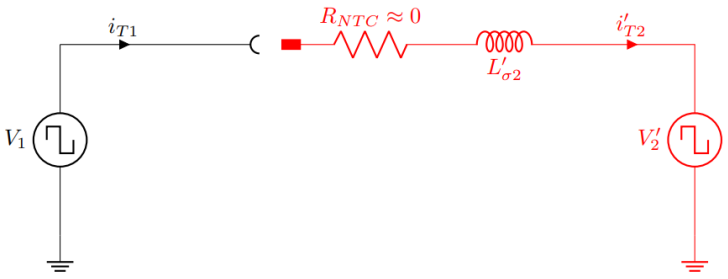

Figure 3.22: Under steady state, the NTC resistor shows small resistance and therefore can be ignored in the circuit. The MAB converter with NTC under steady state operation will be approximated as normal MAB converter.

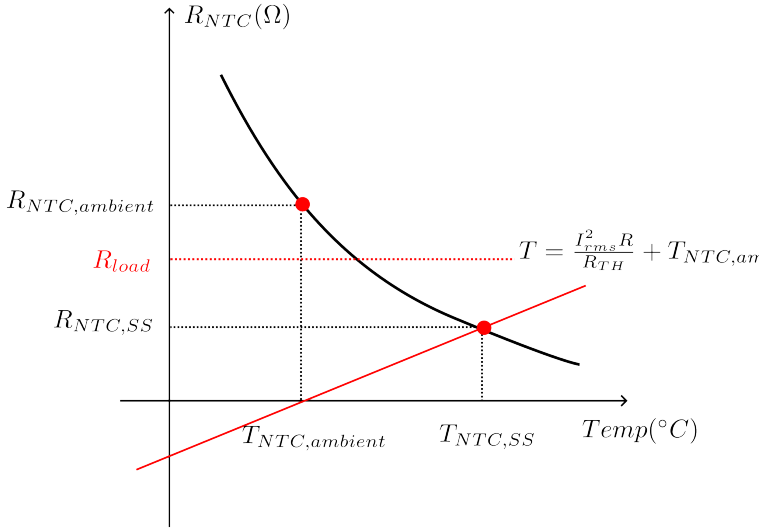

Figure 3.23: The NTC selection standard for slave side with resistive load.

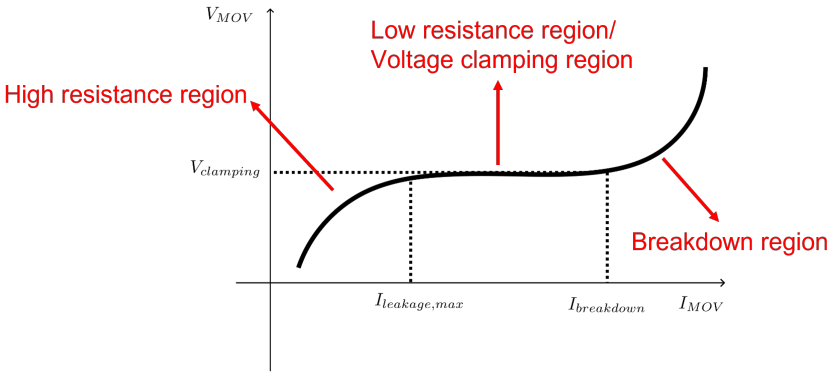

Figure 3.24: The typical V-I curve for Metal-Oxide-Varistor.

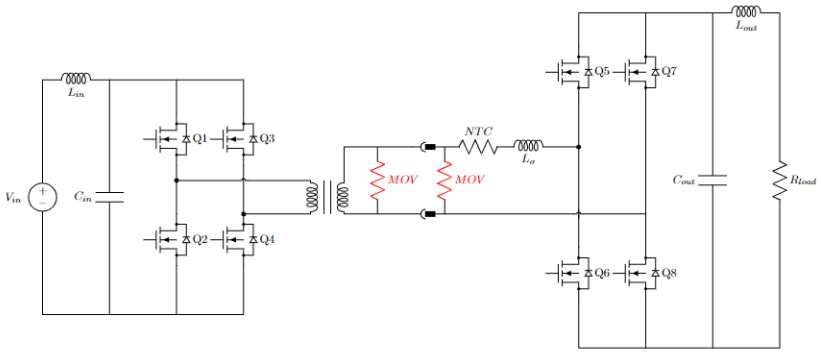

Figure 3.25: The MAB converter circuit with both NTC resistor and MOV resistor.

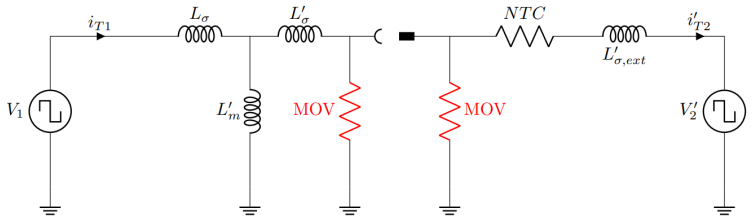

Figure 3.26: The equivalent model of the MAB converter with both NTC and MOV.

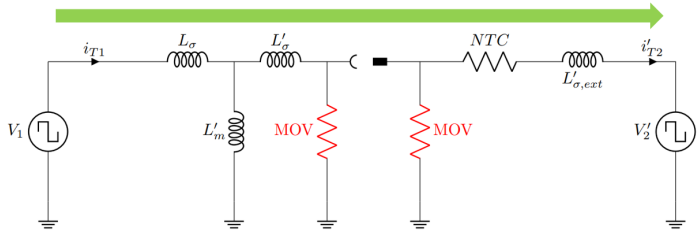

(a) The power flow during normal operation.

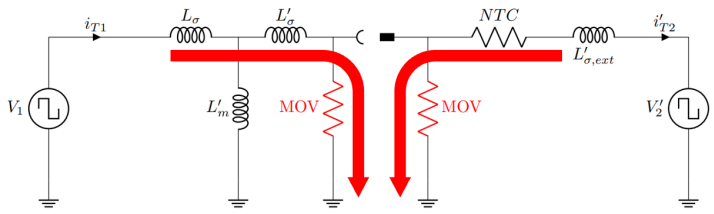

(b) The power flow during slave port plugging-out transient.

Figure 3.27: The power flow in the MAB converter with MOVs.

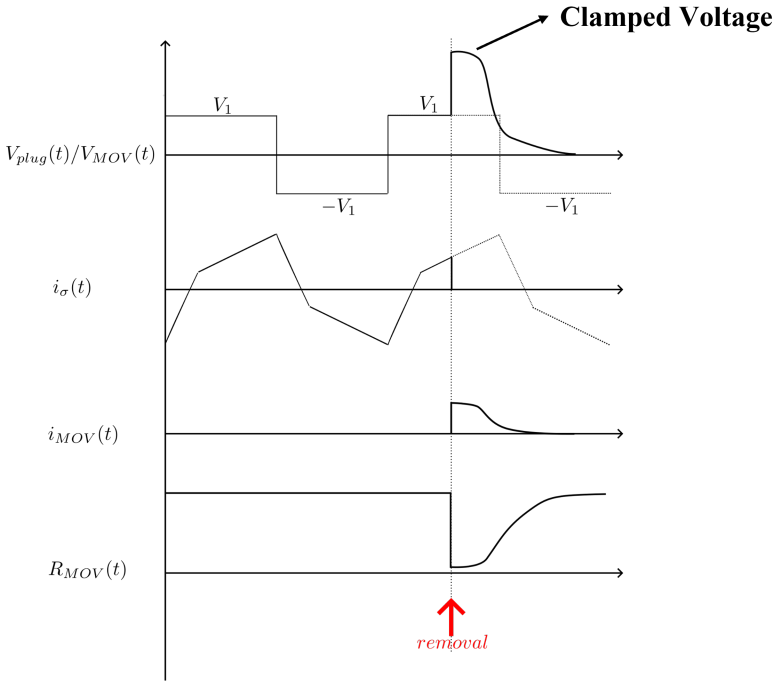

Figure 3.28: The waveform of plug voltage, external leakage inductor current, MOV current and equivalent MOV resistance is sketched during normal steady-state operation and plugging-out transient.

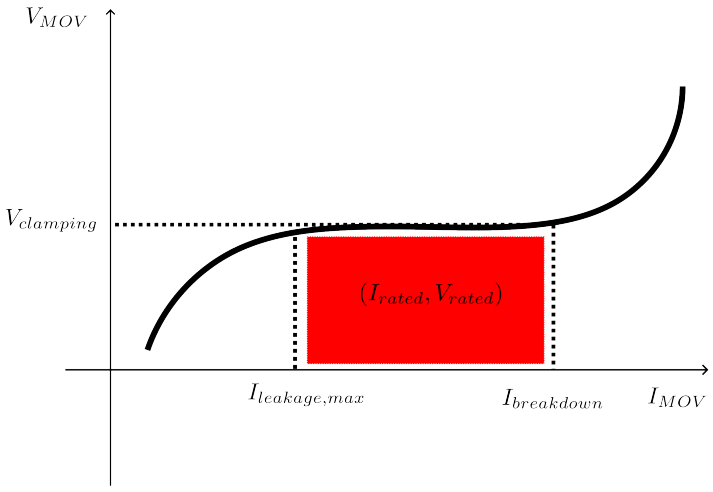

Figure 3.29: The demonstration of requirements for MOV selection. The appropriate MOV should satisfies that the operating maximum instantaneous current and operating voltage should fall in the red region.

4

Decentralized Control Strategy

4.1. Overview

4.1.1. Traditional Control Scheme

The traditional MAB converter uses a centralized control strategy, and the typical block diagram of current loop control strategy can be shown in Figure 4.1. For an N-port MAB converter, the converter system is a Multi-Input-Multi-Output (MIMO) system, and there are N control loops corresponding to each of the ports respectively. In the example of Figure 4.1, N current loops for port #1 to port #n are used.

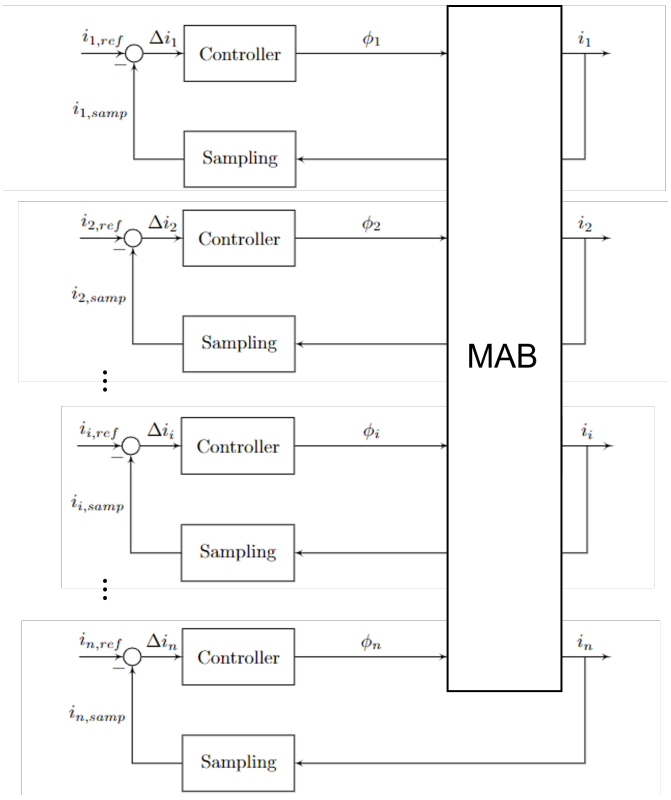

Figure 4.1: The typical current loop control block diagram for MIMO MAB system.

4.1.2. Decoupled Control Scheme

The original configuration of the MAB causes tightly coupled active ports as the MIMO system in Figure 4.1, and thus results in sophisticated control design for converter operation. In general, multiple directions of solutions are proven effective in controller decoupling, and the multiple Single-Input-Single-Output (SISO) systems can be derived to the converter as shown in Figure 4.2.

To achieve an intended SISO configuration, [4] applied Linear Active Disturbance Rejection Control (LADRC) to regulate voltage output by rejecting the disturbance of each coupling ports observed. [5] uses another methods by applying different bandwidths of each independent control loops in the multiport converter. Another method is to use a precalculated gain matrix in control system design for decoupling [3]. All of the methods mentioned applied software implementation and showed effectiveness in ports decoupling. However, these generally require large software work and microcontroller implementation complexity and thus are regarded as low cost-effective solutions.

In [16] as mentioned in Chapter 2, the hardware implementation is proposed as a simpler idea to decouple the ports. The MAB system in small signal model can be expressed as Equation 4.1, and with a highly coupled transformer and significantly large external inductor compared to the leakage inductance, the transfer function can be approximated as:

$$\Delta \mathbf{I'} = \begin{bmatrix} \Delta I_1' \\ \Delta I_2' \\ \vdots \\ \Delta I_i' \\ \vdots \\ \Delta I_n' \end{bmatrix} = \begin{bmatrix} G_{11,SS} & G_{12,SS} & \cdots & G_{1i,SS} & \cdots & G_{1n,SS} \\ G_{21,SS} & G_{22,SS} & \cdots & 0 & \cdots & 0 \\ \vdots & \vdots & \cdots & \vdots & \cdots & \vdots \\ G_{i1,SS} & 0 & \cdots & G_{ii,SS} & \cdots & 0 \\ \vdots & \vdots & \cdots & \vdots & \cdots & \vdots \\ G_{n1,SS} & 0 & \cdots & 0 & \cdots & G_{nn,SS} \end{bmatrix} \begin{bmatrix} \Delta\phi_1 \\ \Delta\phi_2 \\ \vdots \\ \Delta\phi_i \\ \vdots \\ \Delta\phi_n \end{bmatrix} = \mathbf{G'}\Delta\phi \tag{4.1}$$

Therefore, for the slave modules, the transfer function is naturally decoupled so that can be re-written as:

$$\Delta I_i' = \begin{cases} \sum_{i=1}^{n} G_{1i,SS}\Delta\phi_i & i = 1 \\ G_{ii,SS}\Delta\phi_i & i \neq 1 \end{cases} \tag{4.2}$$

The sub-index $i \neq 1$ represents any slave port, and the equation after ideal master-slave configuration shows independence in controlling that the slave port current is solely controlled by one input of phase shift of its own switching bridge. Therefore, the operation of slave port resembles the basic DAB converter and the control methods of SPS can be applied to the decoupled ports for simplicity.

4.1.3. Decentralized Control Scheme

With a hot-swapping configuration of the MAB converter elaborated in Chapter 3, the signals need to transfer between stationary master side and hot-swapping slave sides, which increases complexity in hardware design and brings potential integrity problems of signal transmission. Therefore, with ideal decoupled power flow and decoupled control scheme, each control loops can be distributed to each slave ports separately, and the ideal of decentralized control is demonstrated in Figure 4.3.

The features of implementing a decentralized control scheme come to a more flexible and scalable design. With a decentralized controller on each ports, the slave ports can be made fully modular, the controller is not required to re-designed when adding or removing the

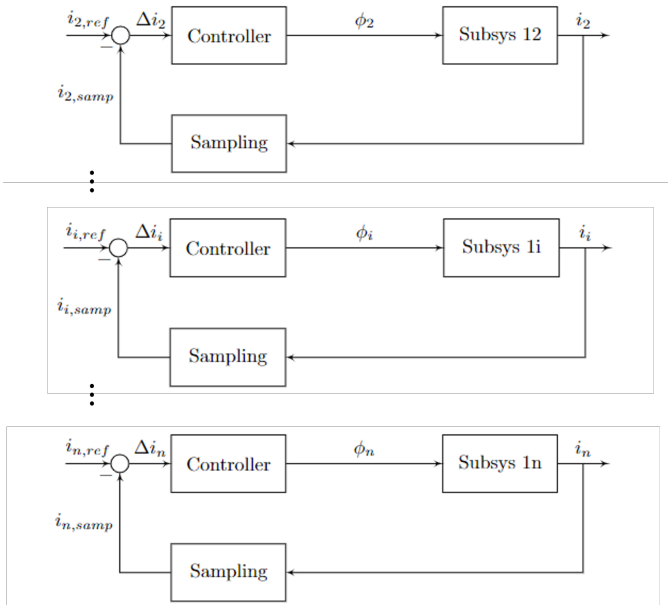

Figure 4.2: The decoupled current loops for the MAB converter. The original MIMO system is devided into multiple SISO systems and can be controlled independently.

ports. And the specifications of the slave sides are independent, meaning a design freedom that can be determined by the users. Additionally, the quantity of ports is only limited to the reserved secondary windings of the transformer, and this highly flexible design suggests an advantageous ability in renewable-energy-based application scenarios.

4.2. Practical Implementation

4.2.1. Control Implementation on Master Side

The control on the master side should provide the PWM signals for switching bridge with constant phase and constant duty ratio of 50%. Therefore, the PWM generation mechanism is demonstrated in Figure 4.4. The control consists of two carrier waves for PWM signals on and off respectively.

The carrier waves are sawtooth waves, with a constant frequency, constant rising time which equals to the period time, and zero falling time. The two carrier waves have a phase shift of 180∘, so either one can be the On carrier and the other on will become the Off carrier. The carriers will then be level-shifted with an offset value m, typically this value is set to zero for idle phase for master side.

The level-shifted carrier signals will then pass through zero-crossing detection modules, by which the up-crossing events are detected and generates pulse signals. The alternating pulses from On carrier and Off carrier will then trigger the SR flip-flop to generate the PWM signals. In this case the phase shift of 180∘ of the two carriers guaranteed a constant duty ratio of 50% with any value of offset value m. The overall signals and PWM generated are plotted in Figure 4.5.

4.2.2. Control Implementation on Slave Sides

The control of slave sides is fully independent due to the decentralized control strategy proposed above. However, the reference phase is required for SPS control of the converter,

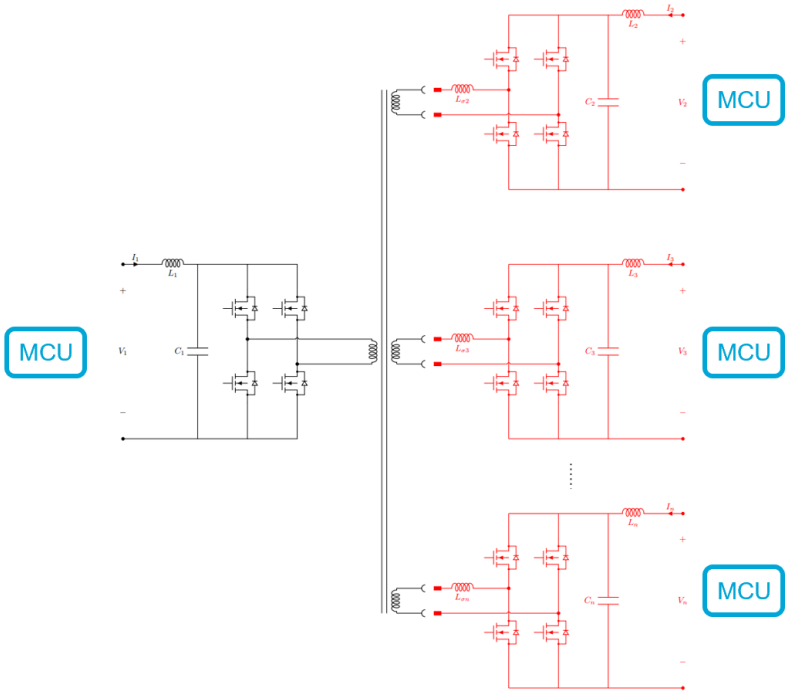

Figure 4.3: The ideal of decentralized control strategy of the MAB converter.

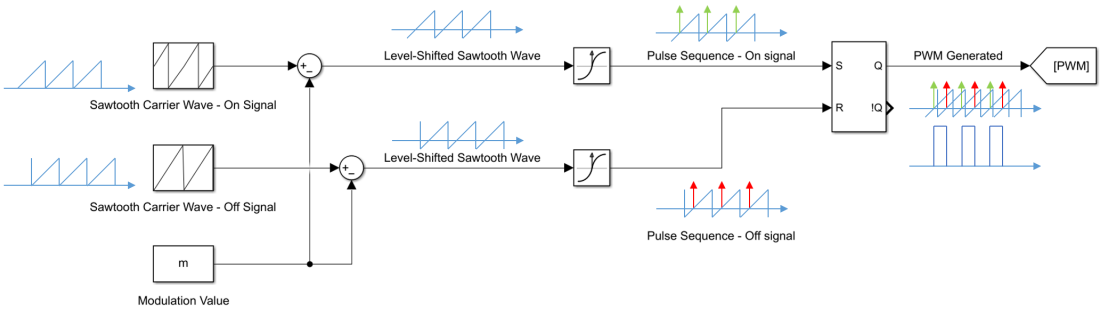

Figure 4.4: The block diagram and signal visualization of the control system of the master port.

and according to the SPS control theory, the reference phase should synchronize with the master side switching bridge for accurate control operation.
Under ideal operation and master-slave configuration of the transformer, the voltage waveform appeared on the AC side of the master bridge is similar with the voltage waveform on the secondary windings, and therefore the plug and sockets but with amplitudes determined by turns ratio of corresponding windings. The voltage waveforms are demonstrated in Figure 4.6.The waveform on the master AC side represents the switching behavior of the constant master switching bridge. Information on carrier signals can be further derived from the voltage waveform, which is taken for the slave side synchronization. Therefore, by adding a SYNC module for the slave sides the decentralized control can be achieved, as shown in Figure 4.7, and the full decentralized control implementation is demonstrated in Figure 4.8. In this case the reference phase for slave side controller is indirectly obtained from the AC plug voltage waveform.

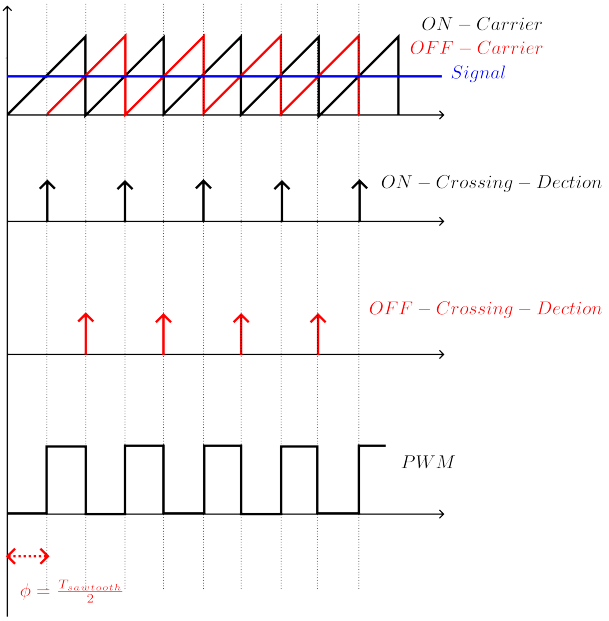

Figure 4.5: The waveforms in control systems of PWM generation with fixed duty ratio and phase. This is applicable in master sides.

In this SYNC module, the voltage waveform on the plug is sampled and passed through a filter and voltage divider for signal processing. The processed signal is examined by two zero-crossing detectors, one with up-crossing detection and the other with down-crossing detection. The generated pulses from the two zero-crossing detection blocks theoretically have a phase difference of half cycle. And the pulses helps reset the constantly integrating blocks to zero, which eventually formulate two sawtooth waves, with an ideal phase shift of half cycle named as On-carrier and Off-carrier respectively, can be adopted for further PWM processing. And the following steps resembles the control implementation on the master side.
With a synchronized carrier waves of both master side and slave side, the PWM modulation can be regarded as the normal SPS control as the typical DAB converter. The PWM generation from two modulation signals and same carrier waves are demonstrated in Figure 4.9. The solid modulation line represents the signal from master side and is assumed to be constant, while the dashed line is the modulated value from slave side with a range between $V_{carrier,min}$ and $V_{carrier,max}$. The phase shift of 180° guaranteed a duty ratio of 50%, and different modulation signals provides different offset which eventually result in an phase shift of two PWM signals.

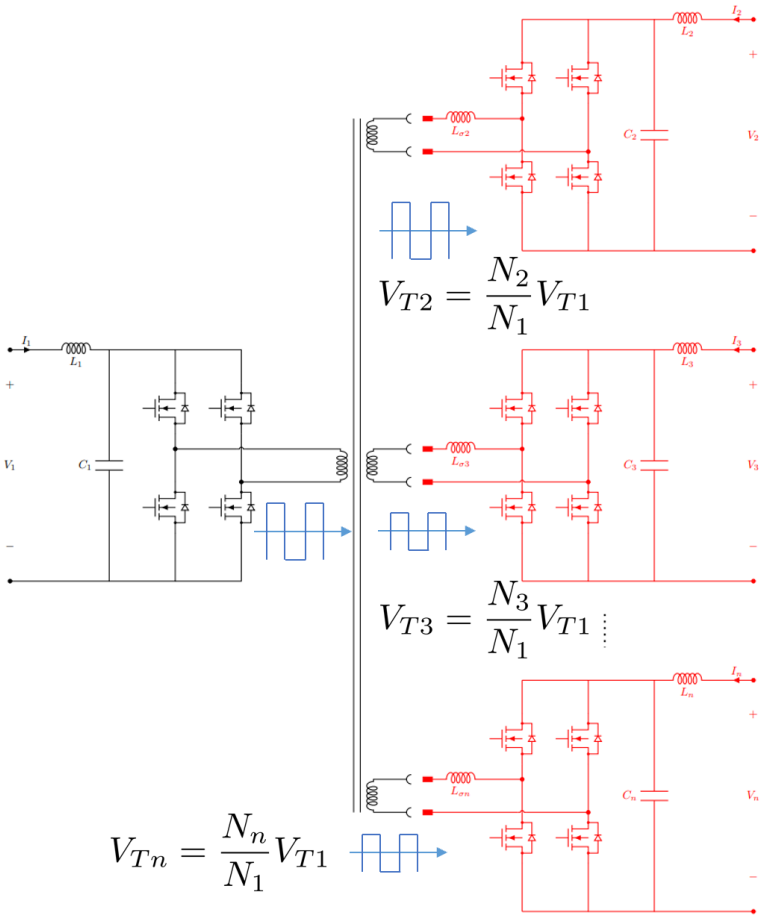

Figure 4.6: The voltage waveform of transformer windings of the MAB converter. This is under the assumption that the leakage inductance of the transformer is negligible.

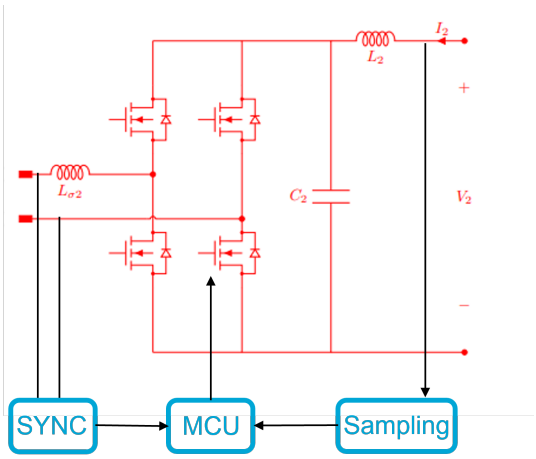

Figure 4.7: The configuration of the decentralized control system with a SYNC module of the slave ports.

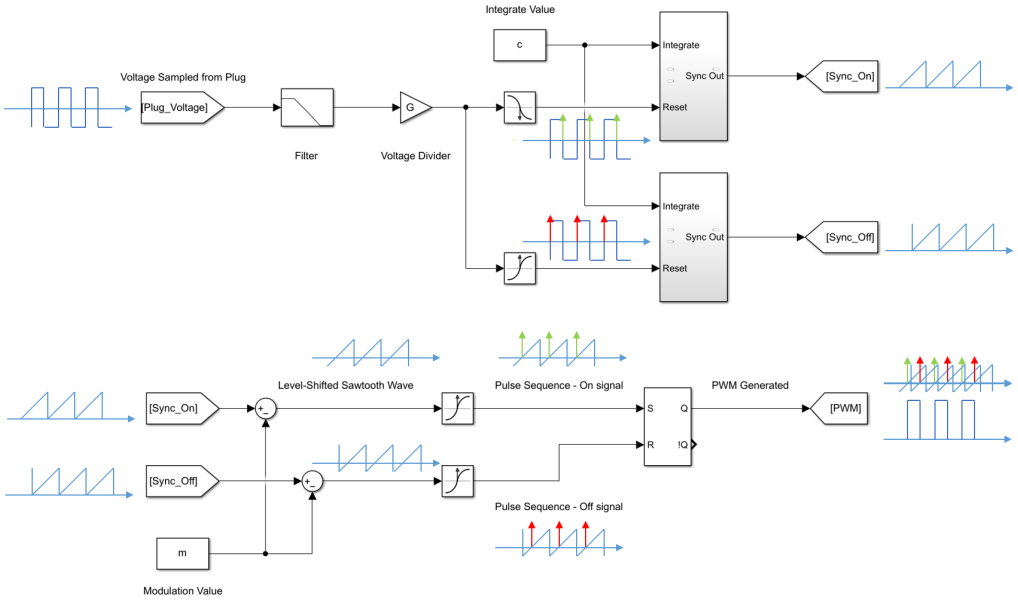

Figure 4.8: The block diagram and signal visualization of the control system of the slave ports.

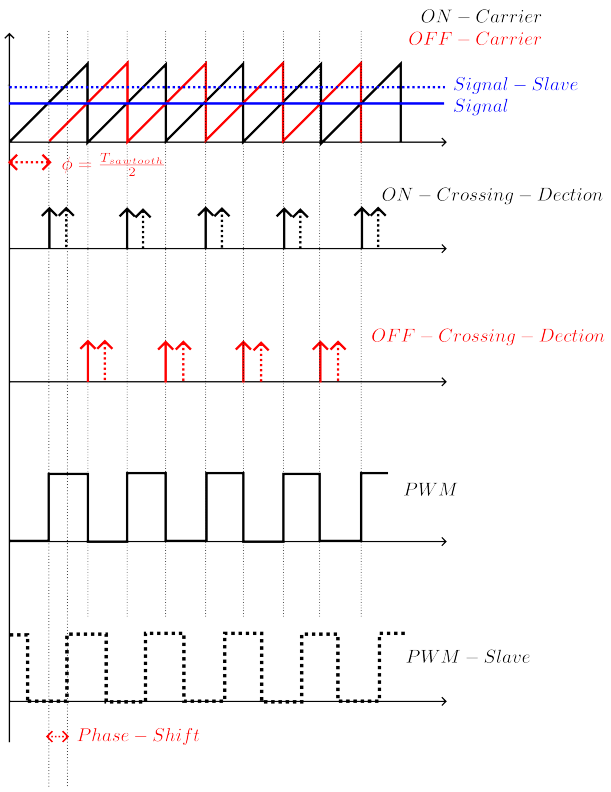

Figure 4.9: The waveforms in control systems of PWM generation. The solid line is a signal with fixed duty ratio and phase, which represents the signals from the master side. The dashed signal is the modulated signal with a fixed duty ratio but with a phase-shoft compared to the solid line, which can represent the waveform from the slave sides.

5

Simulation

5.1. Overview

The simulation and design of a prototype of four-port MAB converter, which is also named Quad-Active-Bridge or QAB converter with the aforementioned features, is carried to validate the theories discussed from Chapter 2 to Chapter 4. The specifications of the converter is shown in Table 5.1. This converter is consisted of four ports, and port #1 is configured as a master port according to the concept demonstrated in Chapter 2, while by adding external inductors with an appropriate value for the other three ports to make slave ports.
In this chapter, the specifications and considerations of the QAB converter is discussed in the next section. And in the following section, six simulation items are carried and evaluated, the software PLECS is adopted in this thesis for power converter simulation, including basic circuit analysis, control and thermal behavior.

Table 5.1: MAB converter specifications

Parameter	**Ports**			
	#1	#2	#3	#4
Port Type	DC source	Passive load	Passive load	Passive load
Master/Slave Type	Master	Slave	Slave	Slave
External Inductor	0	25μH	25μH	25μH
DC Rated Voltage V_{rated}	350V	350V	48V	48V
Transformer Winding Side	Primary	Secondary	Secondary	Secondary
Transformer Winding Turns	8	8	2	2
Phase Shift Range	0 (fixed)	0 to $\frac{\pi}{2}$	0 to $\frac{\pi}{2}$	0 to $\frac{\pi}{2}$
Transistor Voltage Rating	650V	650V	100V	100V
Rated Power P_{rated}	2200W	2000W	100W	100W
Switching Frequency f_{sw}	200kHz			

5.2. Design Considerations

5.2.1. Sources and Loads

The MAB converter is typically used in renewable-energy-based systems. In this simulation, DC home is the target application scenario.
Due to the essence of passive component on the load side, uni-directional power flow is the only possible operation status for any master-slave pair. Therefore the phase shift of all slave bridges should vary from 0 to π. However, a non-monotonic power versus phase shift as shown in Figure 2.3 brings potential trouble in control systems design. Therefore, a phase shift between 0 and $\frac{\pi}{2}$ is chosen for phase shift range of slave ports.

5.2.2. Rated Parameters

The four ports of this converter are composed of two high-voltage ports and two low-voltage ports. Since the DC home is the assumed application scenario, the parameters chosen for this converter follows generic domestic appliances and Dutch standards. The port #1 and port #2 are high-voltage ports with a voltage rating 350V, which is the Dutch standard DC voltage. The port #3 and port #4 are low-voltage ports, and the rated voltages are configured to 48V, which is a typical voltage for regular home appliances such electronic devices, illumination system and other low voltage loads. This multi-voltage-rating feature shows a versatile capability in practical applications.
With the determined rated voltage, rated operating frequency turns ratio and equivalent linking inductance, the maximum power that can be transferred to the high-voltage load and low-voltage load can be computed as following respectively:

$$P_{350V,max} = \frac{V_1' V_{350V}}{8L_\sigma} \cdot T_s = 3062.5W \tag{5.1}$$

$$P_{48V,max} = \frac{V_1' V_{48V}}{8L_\sigma} \cdot T_s = 105W \tag{5.2}$$

Where the voltage on the primary side V_1 is referred to the secondary sides for simplicity, and is denoted as V_1'. Therefore, the power rating for this converter should be lower than this value and thus 2kW and 100W is selected as the rated power for high-voltage port and low-voltage port respectively for evaluation.
With selected power ratings and voltage ratings, the required resistive load value can be computed that:

$$R_{350V} = \frac{V_{350V}^2}{P_{350V}} = 61.25\Omega \tag{5.3}$$

$$R_{48V} = \frac{V_{48V}^2}{P_{48V}} = 23.04\Omega \tag{5.4}$$

5.2.3. Control Systems Design

For the MAB converter with a passive load, the voltage control loop is applied for precise voltage control of each slave ports. A filter for current filtering and voltage stabilization is applied to the the load resistor, the transfer function of output current to output voltage in Laplace domain is:

$$\frac{u_{out}(s)}{i_{out}(s)} = \frac{sL + R}{s^2LC + sCR + 1} \tag{5.5}$$

Therefore the voltage control loop can be reconfigured as shown in Figure 5.1, and in simulation, the sampling transfer function is set as unity gain for simplicity. The subsystem transfer function is derived from the rated operation point of small signal equivalent model as linearized equation 2.26, and the PI controller is assumed to be configured in series and is designed for a crossover frequency of approximately 1kHz. The open loop transfer function can be written as:

$$\begin{aligned} G_{open}(s) &= G_{PI} \cdot G_{1i,SS} \cdot G_{RLC} \\ &= K_P \left(1 + \frac{K_I}{s}\right) \cdot G_{1i,SS} \cdot \frac{sL+R}{s^2LC + sCR + 1} \end{aligned} \tag{5.6}$$

With rated power and rated voltages of two cases of slave ports listed in Table 5.1, the phase shift compared to the master port at operating points are computed:

$$\phi_{1i,350V} = 0.2055\pi \tag{5.7}$$

$$\phi_{1i,48V} = 0.3909\pi \tag{5.8}$$

Thus the gain of subsystem is approximately computed that:

$$\begin{aligned} G_{1i,350V,SS} &= \frac{V'_{350V,SS}}{2\pi L_{1i,350V}} \left(1 - \frac{2|\phi_{1i,350V,SS}|}{\pi}\right) T_s \\ &= 6.5620 \end{aligned} \tag{5.9}$$

$$\begin{aligned} G_{1i,48V,SS} &= \frac{V'_{48V,SS}}{2\pi L_{1i,48V}} \left(1 - \frac{2|\phi_{1i,48V,SS}|}{\pi}\right) T_s \\ &= 0.3334 \end{aligned} \tag{5.10}$$

The crossover frequency of each voltage loop control systems is set to 100Hz for noise and disturbance rejection. To achieve this, the values of K_P and K_I in Table 5.2 is selected. The bode plots of the control open loop gain are demonstrated in Figure 5.2a and Figure 5.2a respectively.

Table 5.2: K_P and K_I values selected for controllers of slave ports different voltage power ratings.

	K_P	K_I
High Voltage Port	0.005	1
Low Voltage Port	0.15	1

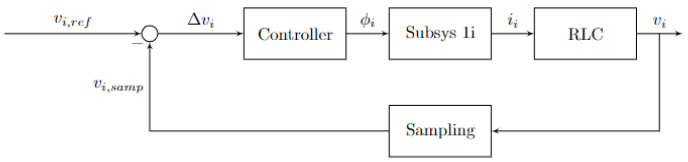

Figure 5.1: The block diagram of full control loop of any slave port of decoupled MAB converter.

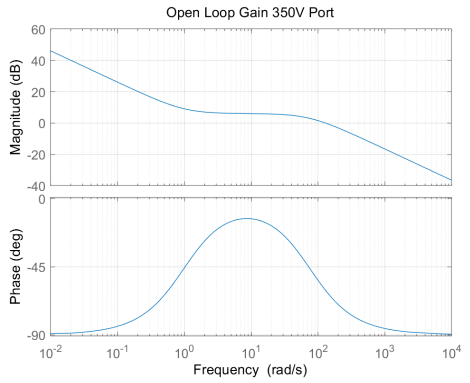

(a) Open loop gain for high voltage port, $f_{crossover} \approx 100Hz$

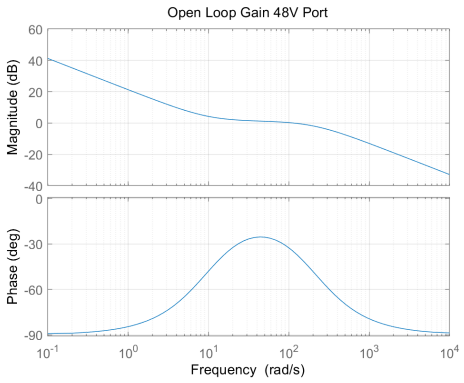

(b) Open loop gain for low voltage port, $f_{crossover} \approx 100Hz$

Figure 5.2: The open loop gain for port #1 (high voltage port) and port #2, #3 (low voltage ports). The PI values selected ensured similar response speed for evaluation.

5.3. Simulation in PLECS

5.3.1. Simulation Case 1: Plugging In/ Plugging Out

In this case study, two slave modules with passive load is inserted into the corresponding socket. The two modules port #1 and port #2 shares identical rated parameters and switch type. However, the NTC is inserted in series with the external inductor of port #2 while no other passive components is placed in port #1, to evaluate the effectiveness of NTC in inrush current limiting. In this simulation the NTC type B57127P709M301 by *TDK Electronics* is selected for 350V port inrush current limiting, the basic parameters is listed in Table 5.3. The R-T curve is plotted in Figure 5.3, and to obtain the trendline of the curve for simulation modeling purpose, EXCEL is applied and the plot is shown in Figure 5.4, the R-T curve fitting equation can be written as:

$$R_{NTC} = 17.354e^{-0.029T} \tag{5.11}$$

Where T is the Celsius temperature.

The simulation circuit is demonstrated in Figure 5.5. The switch with a signal “sw” simulates the insertion action of the hot-swapping ports. To shorten the simulation time the “Thermal Cooling Time Constant” of the NTC resistor is reduced by two order of magnitude. The simulation results and comparison of two ports of plugging-in action is demonstrated in Figure 5.6. It is intuitively observed a smaller inrush current for port with an NTC compared with port without NTC.

Table 5.3: MAB converter specifications

Parameter	Symbol	Value	Unit
Max. Power	P_{max}	10	W
Dissipation Factor	δ_{th}	approx. 50	mW/K
Thermal Cooling Time Constant	τ_{th}	approx. 200	s
Heat Capacity	C_{th}	approx. 10000	mJ/K
Resistance at 25°C	R_{25}	5	Ω
Max. Current	$I_{max}(0...25°C)$	11	A

After a certain period of time, for example 4s (and in reality approximately 400s), the NTC heated up to a steady state and the slave port of this MAB converter reaches a steady state, the inductor current comparison is shown in Figure 5.7. Since the equivalent resistance of the NTC resistor is much smaller than the load resistance, the difference of the inductor current with or without the NTC is hardly observed. Therefore, the selection of this NTC resistor is proved to be effective, that limits the inrush current upon insertion, and causes negligible influences during rated operation.
As for plugging out and MOV simulation, due to the limitations of the piecewise variable resistor modelling in PLECS, the accuracy does not meet the requirements of and thus the simulation of plugging out transient behavior of the MAB converter will not be presented in this thesis.

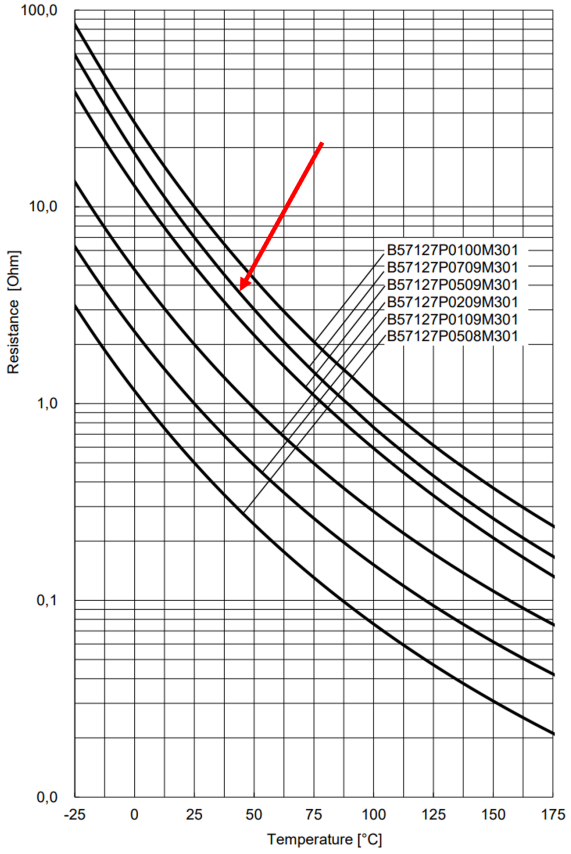

Figure 5.3: The R-T curve for *TDK* NTC series. The type B57127P709M301 selected corresponds to the second curve from the top (red arrow).

5.3.2. Simulation Case 2: Synchronization and Control

In this simulation, the performance of SYNC module and control system is examined. The whole circuit simulation configuration is demonstrated in Figure 5.8. And the SYNC module implementation in PLECS is shown in Figure 5.9, in which the “Transport Delay” block is to simulate the sum of any delay in software processing and hardware implementation in practical situations, and the “Vt sync” block is designed based on the theoretical derivation in Figure 4.8. To simplify the simulation only one slave port with 350V rated output voltage is simulated. One resistor with resistance value of $2R_{350V}$ is applied to the high voltage port,

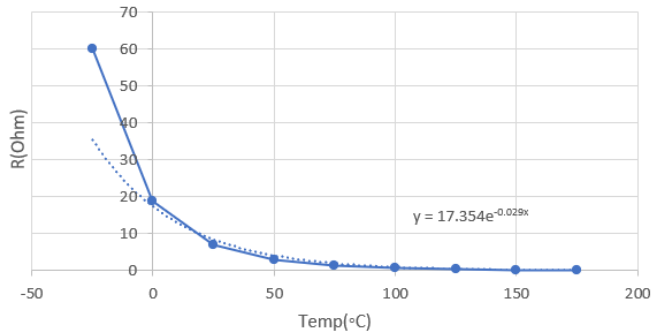

Figure 5.4: The trendline for R-T curve for NTC type B57127P709M301.The value obtained in this plot is only for simulation purposes, and may cause large error in theoretical computation.

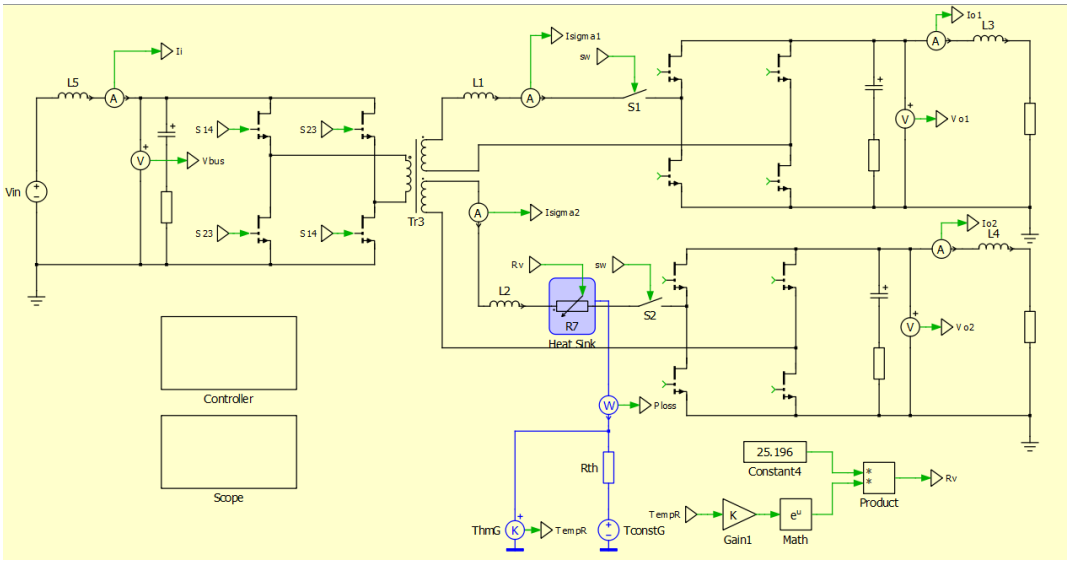

Figure 5.5: The simulation configuration of the MAB converter for NTC verification.

and this load at initial state dissipates the power at half of rated value, i.e. 1kW, and output voltage is maintained at 350V.
Load step from 1kW to 2kW rated power is applied to the port during the half power operation. This is achieved by connecting another parallel resistor with value of $2R_{350V}$ on the load side. Figure 5.10 shows the results of voltage response at the slave port. It is observed that the voltage drop is approximately 3% of rated voltage, and the fast recovery of voltage to reference value suggests an appropriate design of control loop and tuning of PI values. For the verification of synchronization step, it is observed that the carrier wave used to slave port PWM generation is synchronized with the master side carrier wave, with a preset time delay of t_{delay}, as plotted in Figure 5.11. A series value of t_{delay} ranged from 1% 2% 5% and 10% of the cycle period is adopted for simulation, and the result is demonstrated in Figure 5.12. The response to load step change shows light correlation with time delay of the SYNC module, which suggests a large margin of synchronization delay, and the PI values for this voltage-loop control are well-tuned.

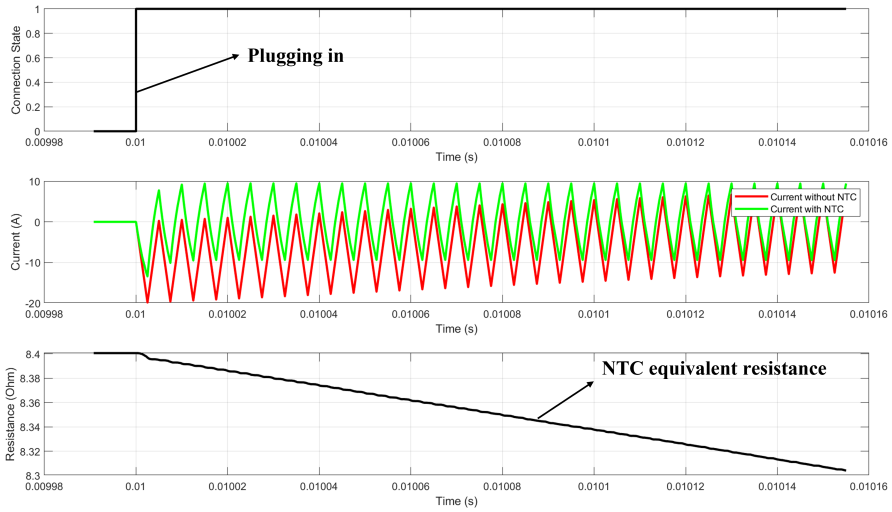

Figure 5.6: The current waveform comparison and resistance of NTC at transient plugging-in action. The green curve (port with NTC) shows smaller inrush current than the red curve (port without NTC).

5.3.3. Simulation Case 3: Decoupling Operation

In this simulation, the evaluation of decoupling of the slave ports is carried. The coupling coefficient is set to a series of different values, which is achieved by setting an ideal transformer and different values of external leakage inductors in PLECS, as demonstrated in Figure 5.13. The load step is applied to the high voltage port, and the voltages on the low voltage port is measured to observe the interference of operation.

A constant values for the external inductors and a series values of leakage inductors are selected to evaluate the decoupling strategy elaborated in Chapter 2. In this simulation a base value of $L_{base} = 25\mu H$ is selected for external inductor and the leakage inductance of the transformer is set as 1%, 2%, 5%, 10% and 20% of the base inductance. The voltage responses on the low voltage port are demonstrated in Figure 5.14.

It is apparently observed that with a leakage inductance lower than 5% of the external inductor, the operation of low voltage port shows negligible interference when load step is applied on the high voltage port. With a leakage larger than this value, the operation on one port will have significant affect on both the steady state operation and transient response of the other ports.

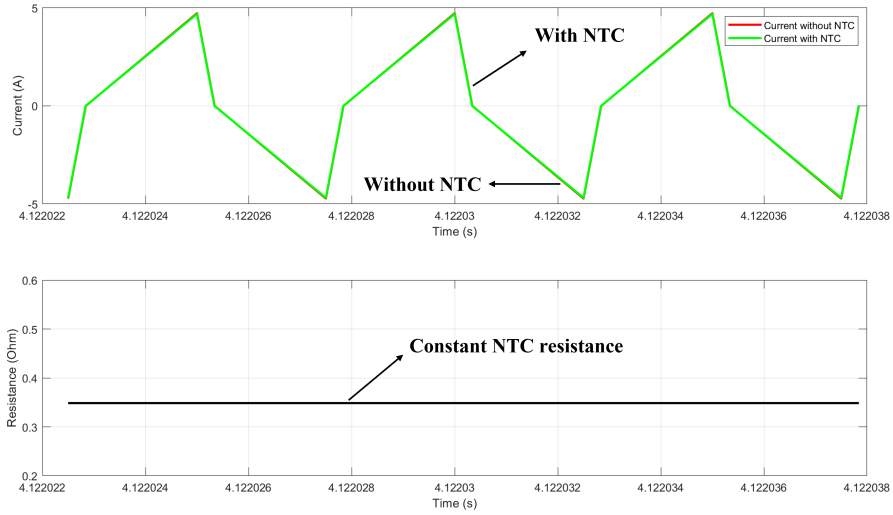

Figure 5.7: The current waveform comparison and resistance of NTC at steady state operation. With a resistance value lower than 1Ω, the port with NTC shows almost no difference with the port without NTC.

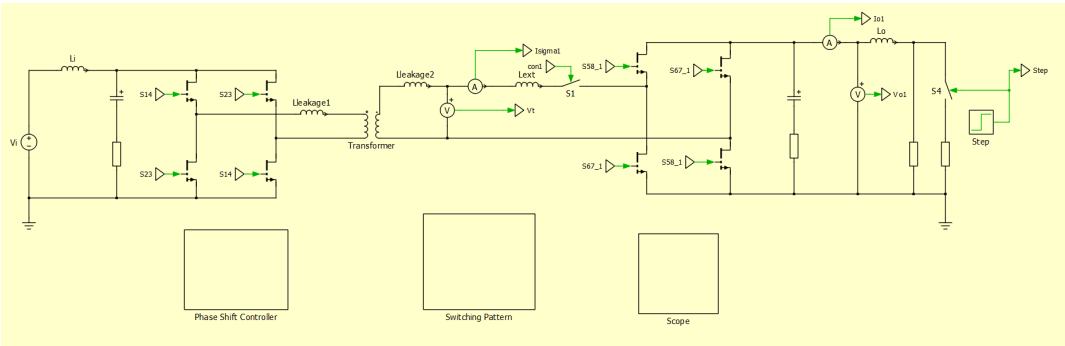

Figure 5.8: The simulation configuration of the MAB converter for case 2. To simplify the verification of control systems only one slave port is examined.

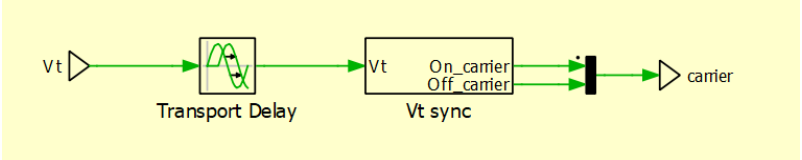

Figure 5.9: The SYNC module implementation. The transport delay simulates the delay in signal processing in practical implementations.

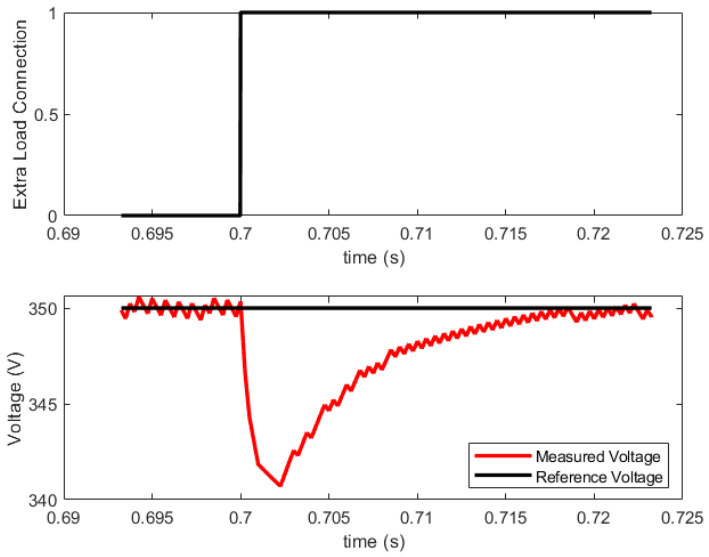

Figure 5.10: The load step response upon connection of extra load. The voltage maintained at 350V with a small fluctuation. The delay is set by default of 100ns (2%T).

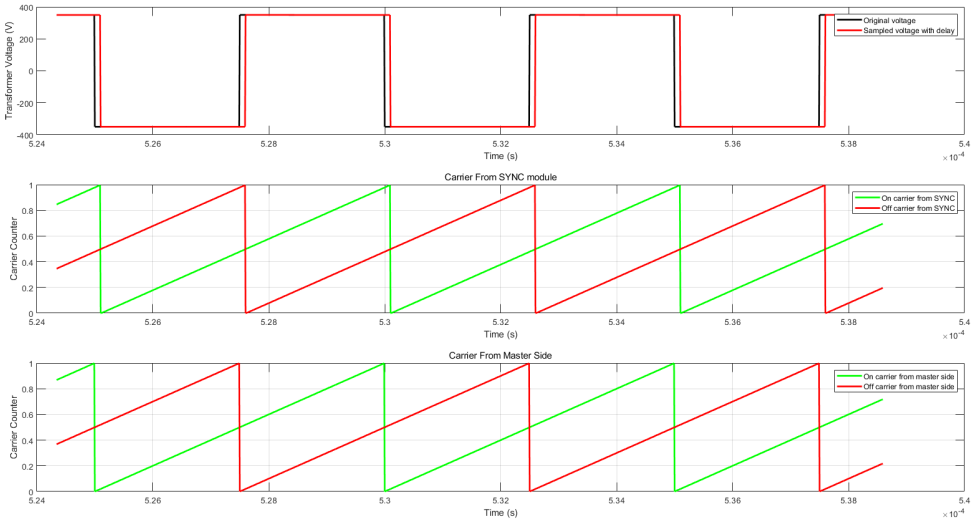

Figure 5.11: The comparison between carrier wave from SYNC module and the constant carrier wave from the master side. Only a small phase shift of t_{delay} is assumed in sampling, and can be observed in generated carrier waves.

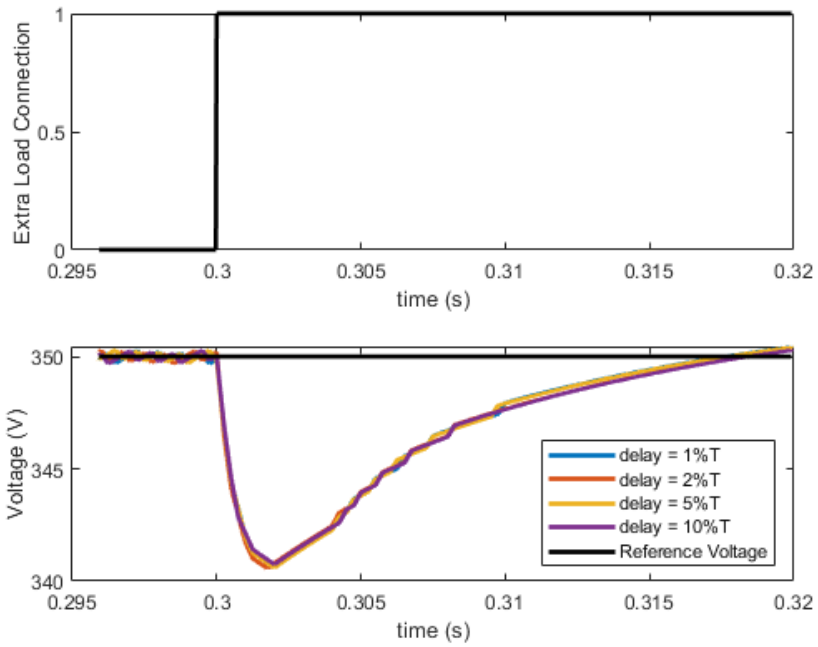

Figure 5.12: The load step response with different values of SYNC delay time. With up to 10% of time delay, the load voltage shows stability and fast response of maintaining at rated voltage during load step transient.

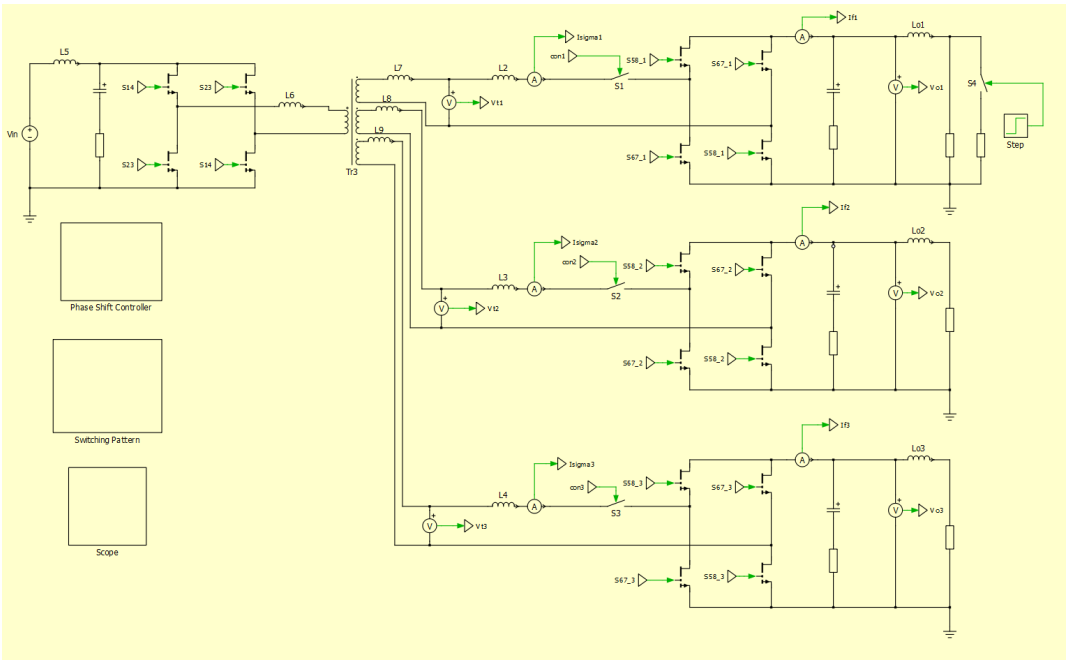

Figure 5.13: The simulation configuration of the MAB converter for case 3. The load step is applied to the high voltage port.

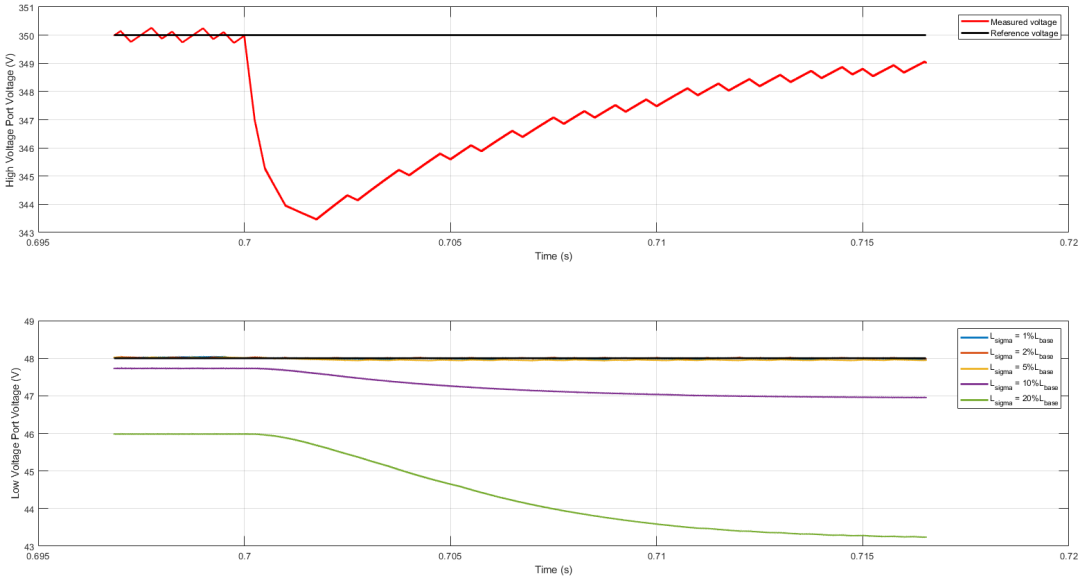

Figure 5.14: The voltage of high voltage ports and low voltage ports upon load step change at high voltage port are plotted to evaluate the decoupling operation of the MAB converter. The series of values of leakage inductances is selected for this decoupling evaluation.

6

Hardware Design

6.1. Overview

To verify the design considerations discussed from Chapter 2 - Chapter 4, the new prototype based on GaN switches will be implemented, as an advanced version compared with the SiC based hardware in [16], that the new prototype will provide a better performances in switching frequency, semiconductor losses, power density and coupling coefficient of the transformer.

The overall configuration of the hardware prototype is demonstrated in Figure 6.1. The whole prototype consists of one stationary master side (main board/ mother board) with a transformer, three hot-swapping slave sides (daughter boards) that can be connected to and disconnected from the main board. The master side is connected with a 350V voltage source and the slave sides are connected with DC passive loads.

The master board is demonstrated in Figure 6.2a. The size of the board is $120mm \times 70mm \times 96mm$, which results in a volume of $V \approx 50in^3$, as shown in Figure 6.2b. The structure of the slave boards resembles the master boards, however the transformer is not required and the hot-swapping peripheral circuit is needed.

For the master board or slave board, the board contains a full bridge switching bridge, a gate driver part for the full bridge, the auxiliary power part, the microcontroller and the transformer part for the master board only. All the components are placed on top layer while the bottom layer is left for heatsink. The microcontrollers from *Texas Instrument* TMS320F28067PNT DSP are adopted for controlling. The transformer is a planar transformer with planar E core E64/10/50, with four PCB windings on separate PCBs for four ports respectively. The solder pads for primary side winding of the transformer is left and the transformer is placed perpendicular to the master board plane. The details of important parts of board design will be further discussed in this Chapter.

6.2. Master Board

6.2.1. Auxiliary Power Supply

The power for integrated circuits (IC) and gate driving of the master board is internally generated with the help of build in auxiliary power supply. This is achieved by obtaining the low voltage from DC bus with the DC/DC buck circuit and voltage regulator, as demon-

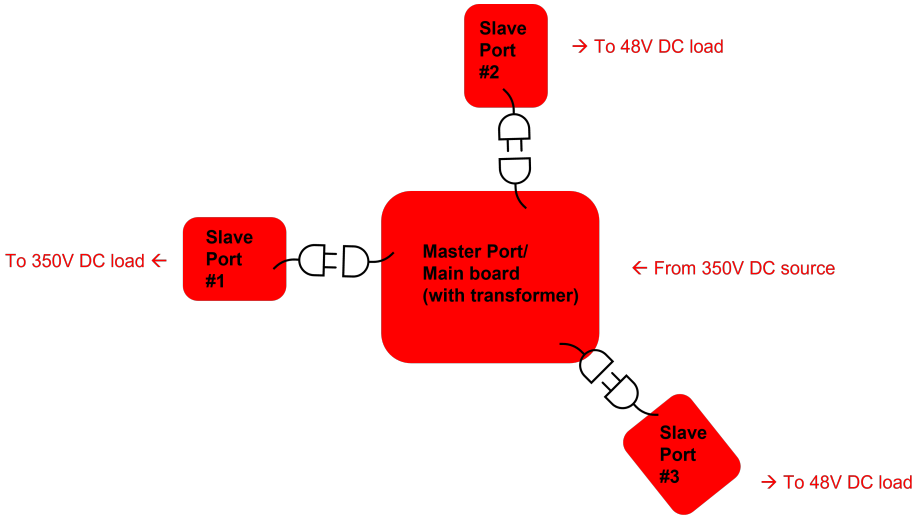

Figure 6.1: The overview demonstration of the hot-swapping prototype.

strated in Figure 6.3. The auxiliary power circuit implementation of prototype design is shown in Figure 6.4 is based on the LT8315 *Analog Devices* power management IC and a non-isolated peripheral circuit is implemented for Buck operation [19]. The feedback resistors ($R_{47} = 15K\Omega$, $R_{48} = 3.3K\Omega$, $R_{83} = 3.3K\Omega$) and the Zener diode at the output bus ensured a steady output voltage of approximately 12.5V, as the LTspice simulation and its results shown in Figure 6.5 and 6.6 respectively. The voltage slightly above 12V gives a margin for driving the ICs on the PCB board.
There are a few notice in simulation and practical application of LT8315 based buck circuit, which are:

1. For simplicity of resistance value selection, only E6 scale resistors are selected.
2. The output voltage is highly dependent on the accuracy of feedback loop.
3. With a 100Ω load, the output current and output power is approximately 120mA and 1.6W respectively, which is sufficient for auxiliary power of one module.
4. The capacitor type (Electrolytic capacitor, SMD capacitor or others) are not considered in simulation, and in practical implementations there might be deviation in output parameters.

6.2.2. GaN-Based Switch and Gate Driving

To facilitate a high switching frequency and high power density of the prototype, the GaN based active switches are adopted for active bridge on the master side. The GaN HEMT type GS66508B (Figure 6.7) from *GaN Systems* is selected, and the ratings of this GaN HEMT, and comparison of *Wolfspeed* C3M0065100K, which is the type of switch used in [16], is listed and compared in Table 6.1.
It is observed that the SiC devices is suitable for high voltage and high current rating applications, while the GaN shows much higher performances in switching speed, losses and achievability to soft-switching. Furthermore, a higher thermal conduction ability is another advantage of GaN devices compared with SiC MOSFET, and the case to ambient thermal resistance of $24°C/W$ indicates a possible implementation of the prototype without

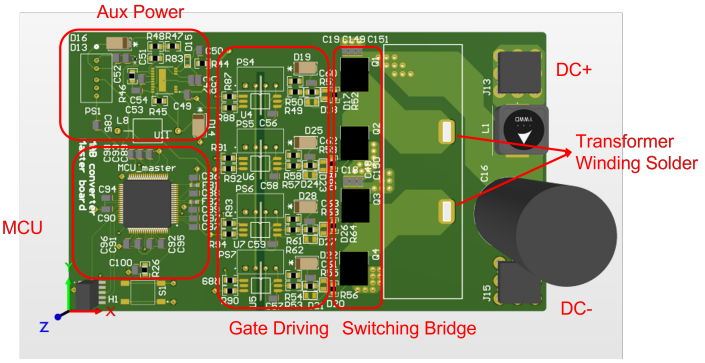

(a) The overview of function areas the master board prototype.

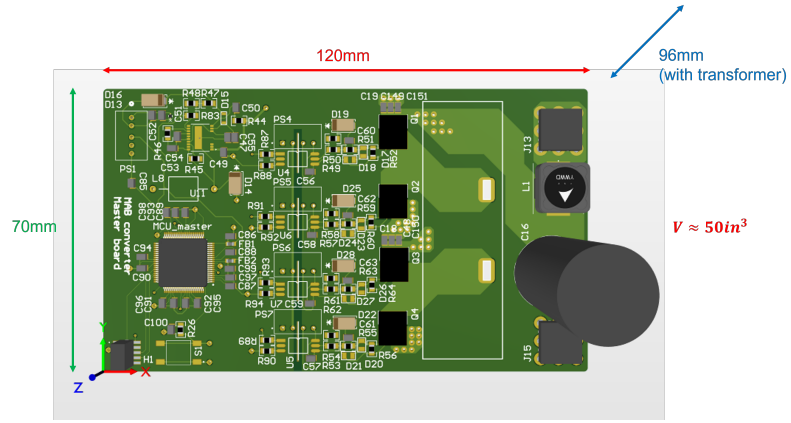

(b) The size of the master board prototype.

Figure 6.2: The overview of 3D model of the master board prototype.

heatsink. Additionally, SMD encapsulation facilitate concise implementation and bottom side cooling, which suggests an advantage in complexity of building a high power density prototype. With all the advantages mentioned, a more concise prototype can be implemented.

The gate driving requirements for GaN enhancement-mode HEMT from *GaN Systems* is similar with typical Si devices and SiC devices [20]. It is a normally-off transistor with a voltage-driven gate driving circuit, and the slew rate of switching transition is simply controlled by external gate resistance. However, there are other essential requirements for GaN HEMT gate driving for reliable operation, which are listed below.

1. Low gate driving turn-on voltage of 5-6V.
2. High current required for gate driving chips.
3. Negative turn-off voltage expected to avoid false turn-on during switching and lower switching-off energy, as shown in Figure 6.8.
4. Reduced gate driving circuit size for minimum stray inductance [20].

Therefore, the gate driving circuit is proposed as Figure 6.9 as recommended by [21], and implemented on PCB as Figure 6.10. The gate driving circuit is identical for all switches so all transistors can function independently which leaves flexibility for further use of the prototype. The gate driving interface consists of an isolated gate driving chip ACPL-P346,

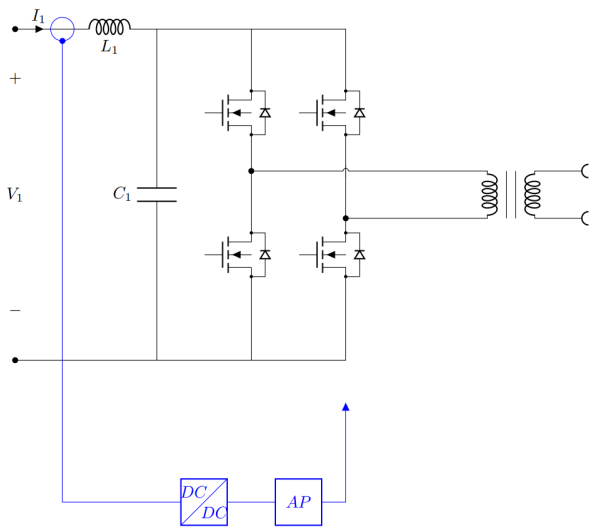

Figure 6.3: The configuration of master side auxiliary power supply.

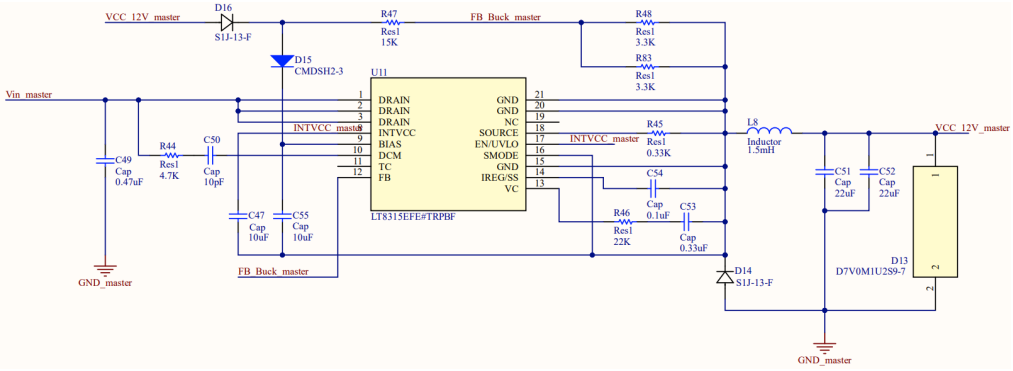

Figure 6.4: The PCB implementation of auxiliary power circuit on the master side.

a gate turn-on resistor of 10Ω and a gate turn-off resistor of 1Ω with a diode connected in parallel, the RC voltage holding circuit and two reversely series connected Zener diode for voltage regulating. The distance between the output of driver IC and the gate of transistor on PCB is approximately 16.5mm, as demonstrated in Figure 6.10.
This design fulfills the gate driving requirements with a voltage supply of 12V on PCB board. This proposed gate driving circuit can achieve negative voltage with the help of only passive components, and the flexibility of controlling the slew rate and EMI issues is also kept. With a 0V/12V input voltage for gate driving power supply, gate-source voltage can be level shifted to -6V/6V. The performance of level shifting can be simulated by LTspice and the signals observed are demonstrated in Figure 6.11.

6.2.3. Planar Transformer

The planar transformer with PCB windings are adopted for transformer design of the MAB converter to achieve low profile, high power density, ease of modularity, high coupling coefficient and minimized leakage inductance [22], [23]. The core selected is a planar E core E64/10/50, with a low to medium ferrite core material with low power losses 3C97, as shown in Figure 6.12. And the basic parameter values of the transformer core is listed in Table 6.2.

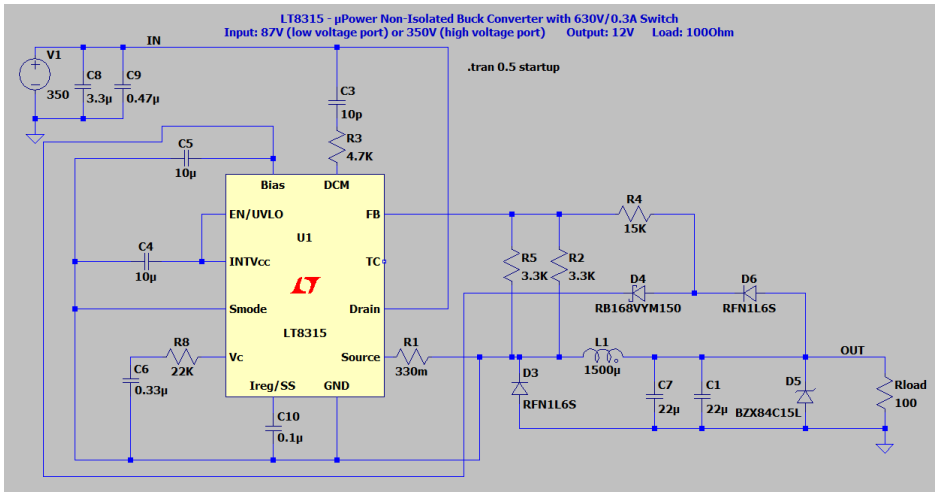

Figure 6.5: The LTspice simulation of LT8315 based buck circuit.

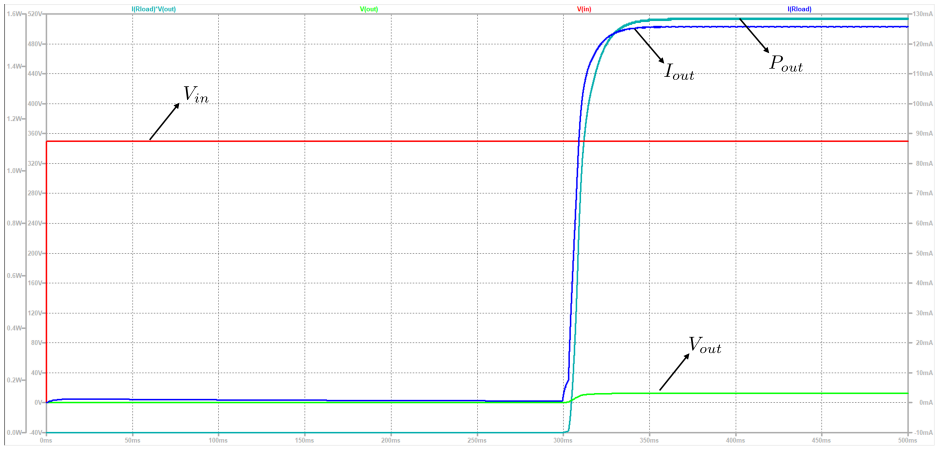

Figure 6.6: The LTspice simulation results of LT8315 based buck circuit, converting 350V DC to 12.5V DC, with an output power of 1.6W.

The PCB windings are designed based on the core size and shown in Figure 6.14. And four PCB windings corresponding to four sides respectively are implemented, thus the cross section view of the whole configuration is demonstrated in Figure 6.13. This modular winding configuration shows advantage in flexibility, that the quantities of secondary sides can be easily modified, by either adding extra PCBs or removing them, as long as the thickness of PCBs combined fits into the the window size.

The PCBs are two-layer PCBs, to avoid the potential heat dissipation problems of internal layer winding. The width of the winding are designed based on the minimum width and required temperature rise for rated current. In this case the large portion of the magnetic flux generated by the AC excitation current on primary side goes through the secondary windings due to the tightly aligned PCB boards, and the cross sectional view of finite element modelling (FEM) of the transformer is demonstrated in Figure 6.15. The linking inductance of any of the two windings are computed from FEM analysis results and listed in Table 6.3, and based on this value matrix, the coupling coefficient matrix can be obtained as shown in Table 6.4, which can further be intuitively plotted in Figure 6.16. Considering the simulation errors, the magnetizing inductance is approximately $255\mu H$ and the cou-

Table 6.1: GaN HEMT GS66508B important ratings, compared with C3M0065100K.

Parameter	Symbol	GS66508B	C3M0065100K
Drain-to-Source Voltage	V_{DS}	650V	1000V
Drain Current	I_{DS}	30A	35A
Drain-to-Source On Resistance	$R_{DS,on}$	$50m\Omega$	$65m\Omega$
Input Capacitance	C_{ISS}	$242pF$	$660pF$
Output Capacitance	C_{OSS}	$65pF$	$60pF$
Rise Time (Typical)	t_r	3.7ns	10ns
Fall Time (Typical)	t_f	5.2ns	8ns
Switching Energy during Turn-on (Typical)	E_{on}	$47.5\mu J$	$190\mu J$
Switching Energy during Turn-off (Typical)	E_{off}	$8\mu J$	$40\mu J$
Packaging	-	SMD	Through Hole
Thermal Resistance from Junction to Ambient	$R_{\theta JA}$	$24°C/W$	$40°C/W$

Figure 6.7: The figure of GS66508B 650V GaN enhancement-mode HEMT from *GaN Systems*.

pling coefficient can higher than 0.998, which suggests a 0.2% of leakage is achieved with this proposed design of the transformer. In this case the equivalent maximum leakage inductance referred to the master side is approximately:

$$L_{\sigma'} \approx 255\mu H \times 0.2\% \approx 0.5\mu H \tag{6.1}$$

The values of coupling coefficients derived is roughly 2% of the external inductor value, meaning a two order of magnitude lower than the base inductance, which verifies an appropriate design of the transformer with required leakage inductance.
However, the planar transformer have the following problems, which leaves potential research focuses for the future study.

1. Limited number of turns. The PCB windings should fulfill the minimum width required for rated current. And for large power rating applications, a redundancy is preferred and thus the turns are strictly limited by the core size.

2. High losses. The skin effect and proximity effect for such tightly placed windings are severe, which results in a much larger loss compared with normal transformer.

3. High capacitance between windings. The PCB winding can be regarded as copper plates and due to the closely aligned windings, the inter-winding capacitance are not

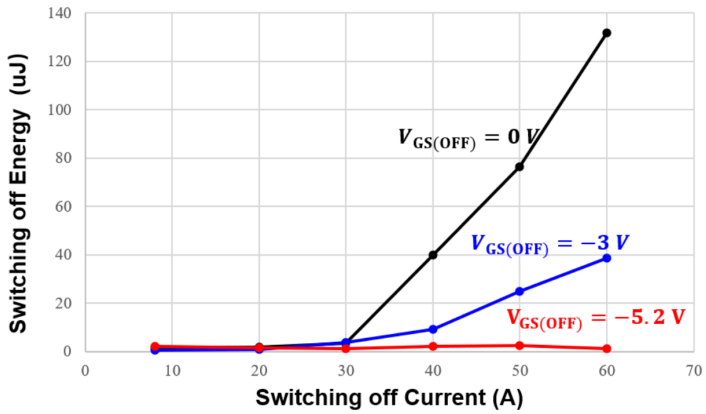

Figure 6.8: The switching off energy losses with different turn-off gate voltages [20]. The testing device is GS66516B with a bus voltage $V_{DC} = 400V$ and gate resistor $R_G = 1\Omega$.

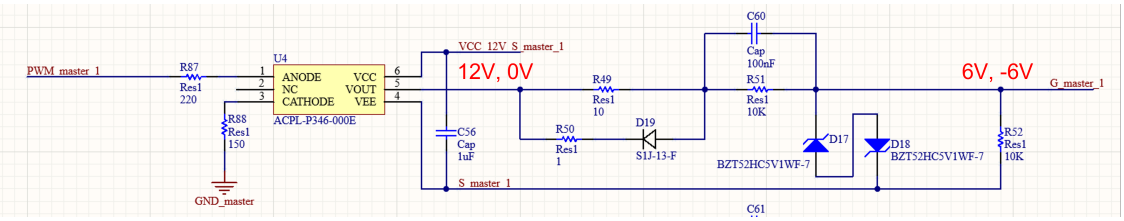

Figure 6.9: The gate driving interface circuit for GS66508B.

negligible. The stray capacitance will affect the transformer equivalent model and eventually the operation of the transformer.

6.3. Slave Boards

6.3.1. NTC and MOV Selection

The selection for hot-swapping peripherals are based on the benchmark discussed in Chapter 3, and the final selection types, and their corresponding curves are listed in Table 6.5.

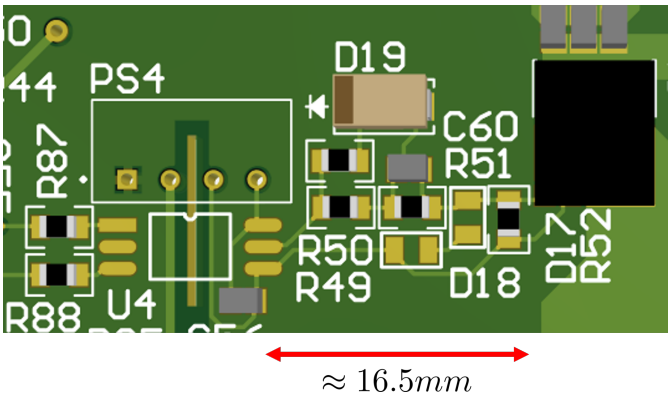

Figure 6.10: The gate driving interface circuit implemented on PCB.

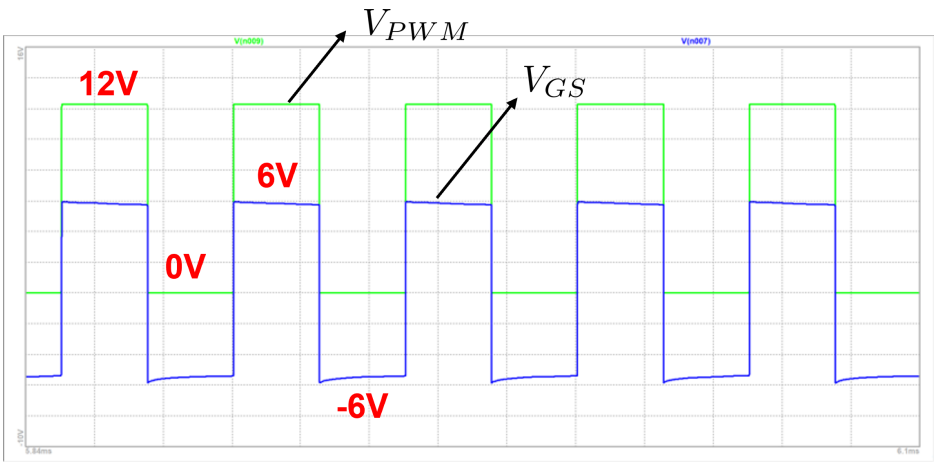

Figure 6.11: The level shifted voltage from 0V/12V to -6V/6V with the help of gate driving interface designed.

Table 6.2: Important specifications of the planar transformer for the MAB converter.

Parameter	Value
Core Width	64mm
Core Length	20.4mm
Depth	50.8mm
Effective Area	$519mm^2$
Window Width	21.8mm
Window Length	10.2mm
Window Area	$212.2mm^2$
Effective Volume	$35500mm^3$
Core Material	3C97
Inductance Factor	$\approx 18500nH/turns^2$
Air gap	$25\mu m$

6.3.2. Auxiliary Power Supply

The auxiliary power supply modules on the slave side are implemented based on the configuration demonstrated in Figure 3.7. The auxiliary power is from the AC plug (350V AC for high voltage port or 87.5V AC for low voltage port), and then goes through a AC/DC stage which is implemented with a diode bridge rectifier ABS10A, and the same buck circuit with LT8315 is followed after the rectifier stage, as shown in Figure 6.19.
The AC voltage from plug and the diode bridge rectifier is assumed to be ideal and thus the DC input of the buck circuit is assumed to be approximately 350V for high voltage port and 87.5V ($350V \times \frac{N_{2,3}}{N_1}$). Therefore the simulation of high voltage port is similar with Figure 6.6. With the same feedback resistors and identica Zener diode, the simulation of low voltage port is demonstrated in Figure 6.20. The output voltage remains at 12.5V and output power is still approximately 1.6W, which is also sufficient for slave side auxiliary power supply.

6.3.3. Sync Sampling and Output Sampling

The key part of the SYNC module is a AC sampling circuit, which converts high voltage dual-ended AC signal into low voltage single-ended AC signal for MCU processing, as demonstrated in Figure 6.21. The sampling circuit consists of a voltage divider, an offset circuit

Table 6.3: Inductance values of the planar transformer designed for the MAB converter, unit:μH.

	Primary	**Secondary 1**	**Secondary 2**	**Secondary 3**
Primary	255.32	255.16	63.75	63.73
Secondary 1	255.16	255.14	63.75	63.74
Secondary 2	63.75	63.75	15.94	15.94
Secondary 3	63.73	63.74	15.94	15.95

Table 6.4: Coupling coefficients of the four windings of the planar transformer designed for the MAB converter.

	Primary	**Secondary 1**	**Secondary 2**	**Secondary 3**
Primary	1	0.9997	0.9993	0.9987
Secondary 1	09997	1	0.9996	0.9992
Secondary 2	0.9993	0.9996	1	0.9997
Secondary 3	0.9987	0.9992	0.9997	1

and the dual-ended to single-ended conversion circuit. The resistance used in voltage divider and offset circuit are much smaller than the conversion circuit, for a relatively large input impedance of the conversion input. And the resistance R_1, R_2, R_3, R_4 have the identical value. With the configuration shown in Figure 6.21, the output is single ended and the output voltage can be computed by the following equation, where the red part is voltage divider and the green part is the offset configuration. And the LTspice simulation of AC voltage sampling is plotted in Figure 6.22.

$$V_{samp,AC} = V_{plug,AC} \times \frac{R_{vd,2}}{R_{vd,1} + R_{vd,2}} + V_{CC} \times \frac{R_{offset,2}}{R_{offset,1} + R_{offset,2}} \tag{6.2}$$

The DC bus voltage sampling is a basic DC sampling circuit which converts a high voltage DC input to low voltage DC output, as demonstrated in Figure 6.23. The sampling circuit is simply consisting of a voltage divider and a buffer based on a normal operational amplifier. And the output voltage can be simply expressed that:

$$V_{samp,DC} = V_{bus,DC} \times \frac{R_{vd,2}}{R_{vd,1} + R_{vd,2}} \tag{6.3}$$

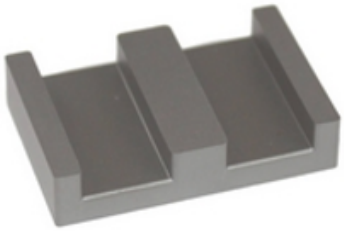

Figure 6.12: The planar E core E64/10/50 selected for four-PCB-winding planar transformer.

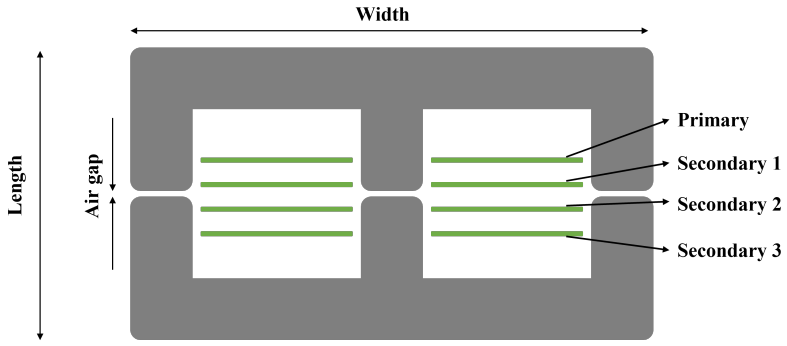

Figure 6.13: The cross sectional view of planar transformer configuration for this four-port MAB converter.

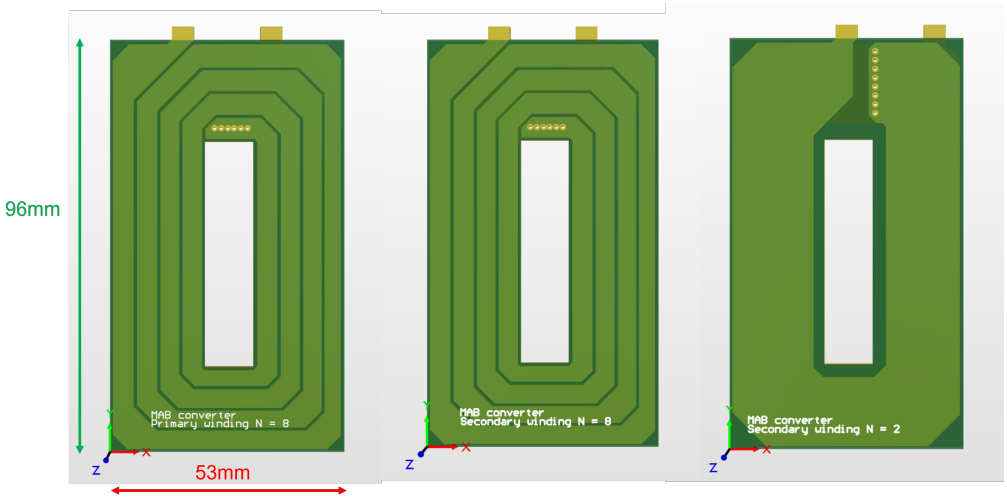

Figure 6.14: The PCB windings and sizes for master side, high voltage slave side and low voltage slave side respectively.

6.3.4. GaN-Based Switch and Gate Driving

The GaN enhancement-mode HEMT is also adopted for active switches on the slave sides. For different power ratings or voltage ratings of slave sides, different type of GaN HEMT are selected. Type GS66508B is applied to high voltage slave port (port #2) as the master side, and type GS61008P 100V GaN HEMT from *GaN Systems* is adopted for low voltage ports (port #3 and port #4), and the key parameters are listed and compared with previous SiC MOSFET C3M0065100K in Table 6.6. It is also observed that the GaN have much superior features compared to SiC devices at application of low voltage ratings.

The gate driving circuits of the slave sides resemble the master side, except the gate resistance for 100V transistor is different based on the recommended value by *GaN Systems*, and the values of gate resistors are listed in Table 6.7.

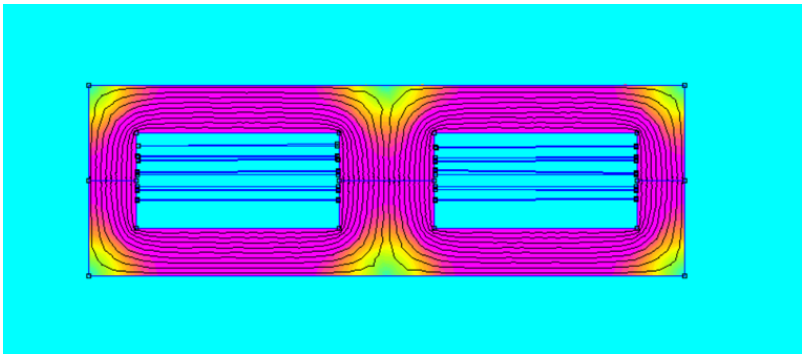

Figure 6.15: The finite element modelling for four-PCB-winding planar transformer.

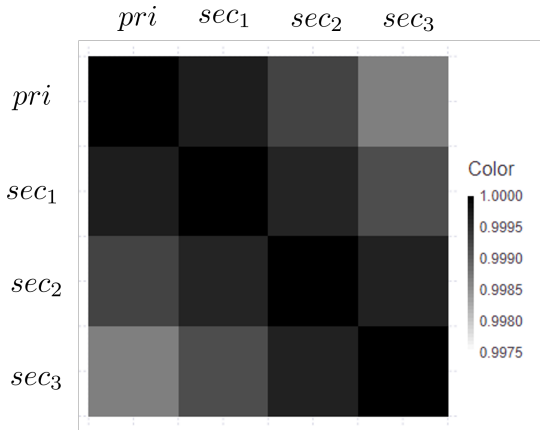

Figure 6.16: The coupling coefficient matrix of the four-winding planar transformer.

Table 6.5: The NTC and MOV type selected and their corresponding characteristics curves.

	High Voltage Port	Low Voltage Port
NTC	B57127P509M301 (Figure 5.3)	B57236S0229M000 (Figure 6.17)
MOV	391KD14 (Figure 6.18)	181KD14 (Figure 6.18)

Table 6.6: GaN HEMT GS61008P important ratings, compared with C3M0065100K.

Parameter	Symbol	GS61008P	C3M0065100K
Drain-to-Source Voltage	V_{DS}	100V	1000V
Drain Current	I_{DS}	90A	35A
Drain-to-Source On Resistance	$R_{DS,on}$	$7m\Omega$	$65m\Omega$
Input Capacitance	C_{ISS}	$600pF$	$660pF$
Output Capacitance	C_{OSS}	$250pF$	$60pF$
Switching Energy during Turn-on (Typical)	E_{on}	$47.5\mu J$	$190\mu J$
Switching Energy during Turn-off (Typical)	E_{off}	$8\mu J$	$40\mu J$
Packaging	-	SMD	Through Hole
Thermal Resistance from Junction to Ambient	$R_{\theta JA}$	$23°C/W$	$40°C/W$

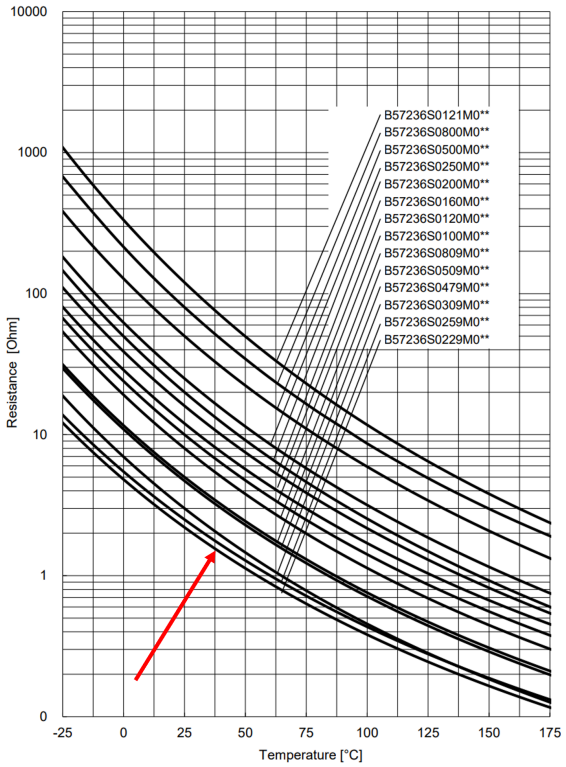

Figure 6.17: The R-T curve for *TDK* NTC series. The type B57236S0229M000 selected corresponds to the first curve from the bottom (red arrow).

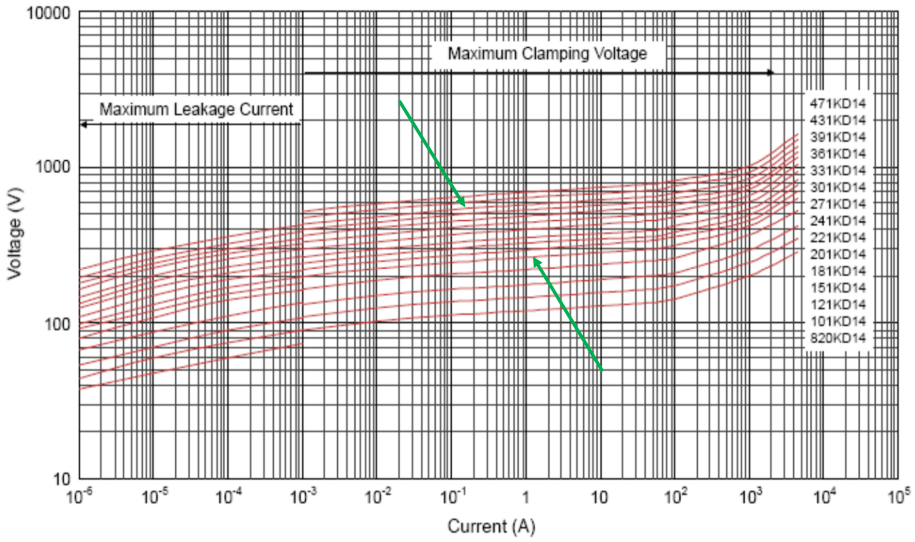

Figure 6.18: The V-I curve for *YAGEO* NTC series. The type 391KD14 and 181KD14 selected correspond to the curves pointed by green arrows.

Table 6.7: GaN HEMT GS61008P and GS66508B gate resistance values selection.

	Voltage Rating	**Turn-on**	**Turn-off**
GS61008P	100V	2Ω	1Ω
GS66508B	650V	10Ω	1Ω

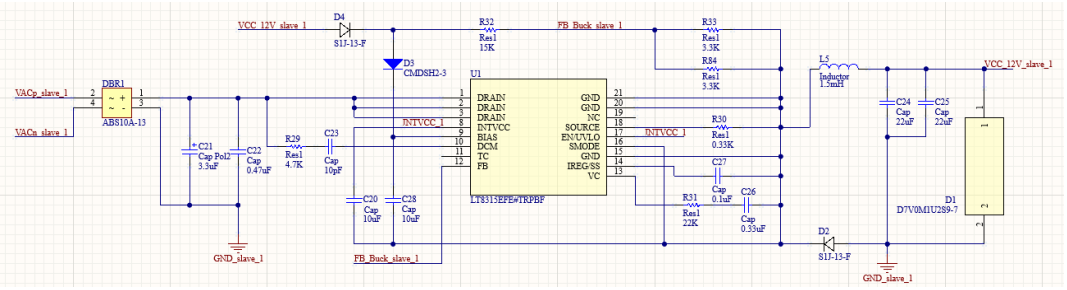

Figure 6.19: The PCB implementation of auxiliary power circuit on the slave side.

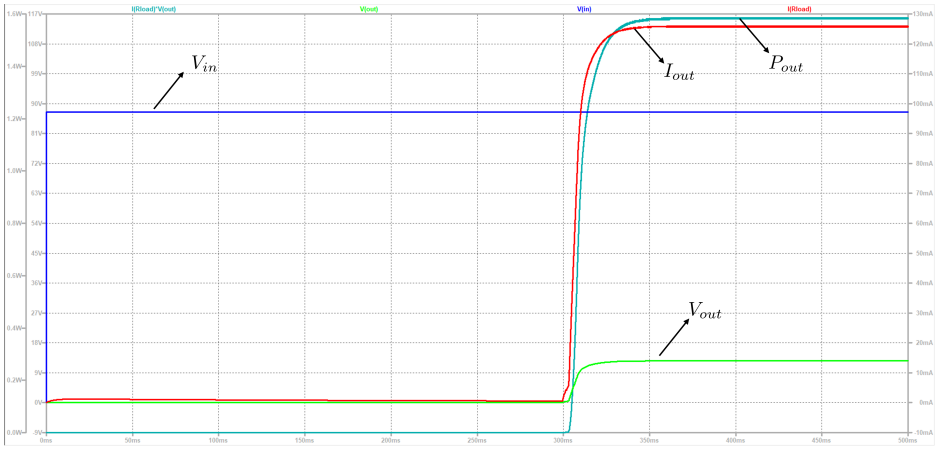

Figure 6.20: The LTspice simulation results of auxiliary power circuit on the low voltage slave side.

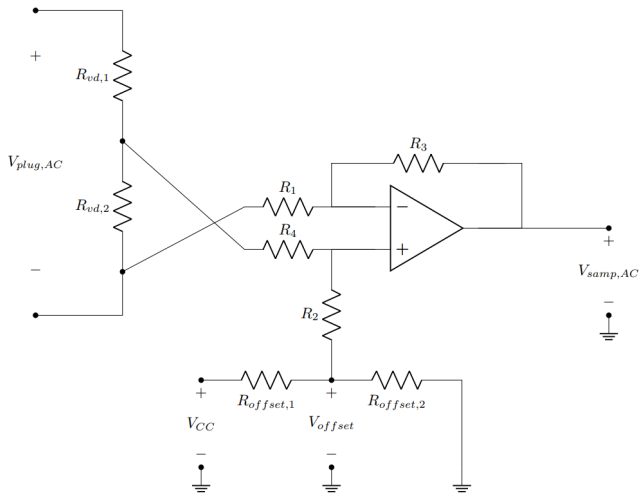

Figure 6.21: The theoretical schematic of AC sampling circuit of the plug voltage for slave ports.

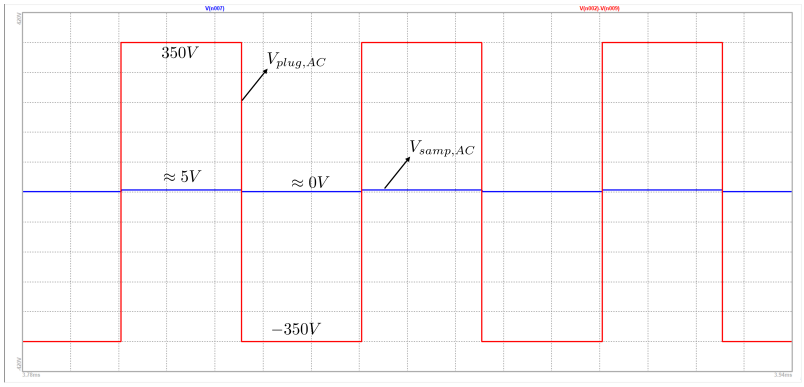

Figure 6.22: The LTspice simulation results of waveform of AC sampling circuit.

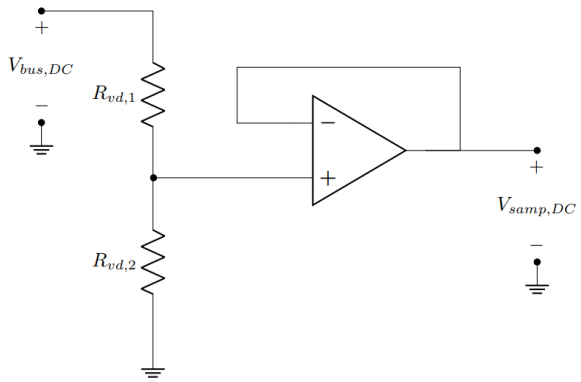

Figure 6.23: The theoretical schematic of DC sampling circuit of the bus voltage for slave ports.

Figure 6.24: The figure of GS61008P 100V GaN enhancement-mode HEMT from *GaN Systems*.

7

Conclusion and Future Work

7.1. Conclusion

This thesis proposed a hot-swapping multi-port DC/DC converter based on the Dual-Active-Bridge basic DC/DC topology. The MAB converter is redesigned as the master-slave configuration with the help of dedicated transformer design, meaning a master port solely dominates the transformer winding voltages and the slave ports are therefore capable of independent operation. The hot-swapping configuration is implemented for slave ports, that each slave ports can be plugged-in or plugged-out from the alive MAB converter without interfering the operation other ports, and the hot-swapping buffer circuit with full passive components is designed for safe insertion and removal. With the independent operation of slave ports, a decentralized control strategy with synchronization capability is designed and implemented, by which standalone MCUs are equipped with all ports for operation control. Finally the GaN HEMT based hardware of the hot-swapping MAB converter is designed, and the planar transformer with modular PCB windings are adopted for high coupling performance and minimum leakage inductance of the transformer.
The achievement of this thesis corresponding to the introduction chapter can be briefly summarized as following:

1. The decoupled power flow is achieved for the multi-port converter.
2. The hot-swapping capability is achieved.
3. The decentralized control methods for independent slave port control is implemented.
4. The GaN-based hardware is designed.

7.2. Future Work

The hardware design for hot-swapping converter should be finalized for further testings and evaluations. This includes an advanced design and application of GaN HEMT components, and the promoted design of the transformer.

1. The GaN HEMT devices have much potentials in high frequency operation of the converter (up to MHz) and thus a extremely high power density prototype can be implemented. To achieve this, a thorough study on the GaN based high frequency

switching circuit and its implementation techniques and layout considerations should be carried.

2. The transformer still have limitations discussed in Chapter 6. Therefore, the trade-offs among the various parameters of the transformer losses and the coupling coefficients should be studied. Additionally, for a more standard design of the planar transformer for this MAB converter, a standard design flow procedure should be researched.

Bibliography

[1] S. Chi, P. Liu, X. Li, M. Xu, and S. Li, "A novel dual phase shift modulation for dual-active- bridge converter," in *2019 IEEE Energy Conversion Congress and Exposition (ECCE)*, 2019, pp. 1556–1561. DOI: 10.1109/ECCE.2019.8912591.

[2] J. Ning, J. Zeng, and X. Du, "A four-port bidirectional dc-dc converter for renewable energy-battery-dc microgrid system," in *2019 IEEE Energy Conversion Congress and Exposition (ECCE)*, 2019, pp. 6722–6727. DOI: 10.1109/ECCE.2019.8912185.

[3] C. Zhao, S. D. Round, and J. W. Kolar, "An isolated three-port bidirectional dc-dc converter with decoupled power flow management," *IEEE Transactions on Power Electronics*, vol. 23, no. 5, pp. 2443–2453, 2008. DOI: 10.1109/TPEL.2008.2002056.

[4] S. Bandyopadhyay, Z. Qin, and P. Bauer, "Decoupling control of multiactive bridge converters using linear active disturbance rejection," *IEEE Transactions on Industrial Electronics*, vol. 68, no. 11, pp. 10 688–10 698, 2021. DOI: 10.1109/TIE.2020.3031531.

[5] S. Falcones, R. Ayyanar, and X. Mao, "A dc–dc multiport-converter-based solid-state transformer integrating distributed generation and storage," *IEEE Transactions on Power Electronics*, vol. 28, no. 5, pp. 2192–2203, 2013. DOI: 10.1109/TPEL.2012.2215965.

[6] "An introduction to gan enhancement-mode hemts," Tech. Rep., 2022.

[7] *Power module, multi-port power converter and energy system comprising the same*, 4A/P183582NL00, patent filed.

[8] Y. Qiu and L. J. Lu, "High-power-density 400vdc-19vdc llc solution with gan hemts," in *2018 1st Workshop on Wide Bandgap Power Devices and Applications in Asia (WiPDA Asia)*, 2018, pp. 66–72. DOI: 10.1109/WiPDAAsia.2018.8734685.

[9] Y. Lu, H. Wu, K. Sun, and Y. Xing, "A family of isolated buck-boost converters based on semiactive rectifiers for high-output voltage applications," *IEEE Transactions on Power Electronics*, vol. 31, no. 9, pp. 6327–6340, 2016. DOI: 10.1109/TPEL.2015.2501405.

[10] M. C. Taneri, N. Genc, and A. Mamizadeh, "Analyzing and comparing of variable and constant switching frequency flyback dc-dc converter," in *2019 4th International Conference on Power Electronics and their Applications (ICPEA)*, 2019, pp. 1–5. DOI: 10.1109/ICPEA1.2019.8911196.

[11] "Gallium nitride semiconductor power devices a perfect pair," Tech. Rep.

[12] Y. Wei, Q. Luo, and A. Mantooth, "A hybrid half-bridge llc resonant converter and phase shifted full-bridge converter for high step-up application," in *2020 IEEE Workshop on Wide Bandgap Power Devices and Applications in Asia (WiPDA Asia)*, 2020, pp. 1–6. DOI: 10.1109/WiPDAAsia49671.2020.9360292.

[13] G. F. Laghari, A. Umar, and S. Abdullah, "Comparative analysis of multi-input dc/dc converter topology for hybrid renewable energy systems," in *2015 Power Generation System and Renewable Energy Technologies (PGSRET)*, 2015, pp. 1–5. DOI: 10.1109/PGSRET.2015.7312254.

[14] H. Tarzamni, E. Babaei, and A. Z. Gharehkoushan, "A full soft-switching zvzcs flyback converter using an active auxiliary cell," *IEEE Transactions on Industrial Electronics*, vol. 64, no. 2, pp. 1123–1129, 2017. DOI: 10.1109/TIE.2016.2615601.

[15] A. R. Rodríguez Alonso, J. Sebastian, D. G. Lamar, M. M. Hernando, and A. Vazquez, "An overall study of a dual active bridge for bidirectional dc/dc conversion," in *2010 IEEE Energy Conversion Congress and Exposition*, 2010, pp. 1129–1135. DOI: 10.1109/ECCE.2010.5617847.

[16] S. Bandyopadhyay, P. Purgat, Z. Qin, and P. Bauer, "A multiactive bridge converter with inherently decoupled power flows," *IEEE Transactions on Power Electronics*, vol. 36, no. 2, pp. 2231–2245, 2021. DOI: 10.1109/TPEL.2020.3006266.

[17] J. Styles, "Common misconceptions about the body diode," Tech. Rep., 2019.

[18] B. Sun, "Does gan have a body diode understanding the third quadrant operation of gan," Tech. Rep., 2019.

[19] "560vin micropower no-opto isolated flyback converter with 630v/300ma switch," Tech. Rep., 2017.

[20] "Gate driver circuit design with gan e-hemts," Tech. Rep., 2022.

[21] "Ezdrive power stage solution for gan systems' gan transistor," Tech. Rep., 2022.

[22] L. Dixon, "Designing planar magnetics," Tech. Rep.

[23] Z. Ouyang, "Advances in planar and integrated magnetics," Ph.D. dissertation, Ørsteds Plads, Building 349, DK-2800 Kgs. Lyngby, Denmark, 2011.

A

PCB Schematics and BOM List

Due to the layout of the thesis, the full version of the PCB Schematics can be found at https://github.com/Garyseventeen/docs/blob/main/PCB_Project.pdf.
And the BOM list can be found at https://github.com/Garyseventeen/docs/blob/main/PCB_Project_BOM.pdf.